Development of a SQUID (Superconducting Quantum Interference Device) Detection System of Magnetic Nanoparticles for Cancer Imaging

by

Song Ge

A dissertation submitted in partial fulfillment
of the requirements for the degree of
Doctor of Philosophy
(Physics)
in The University of Michigan
2009

Doctoral Committee:

Professor Bradford G. Orr, Chair
Professor James R. Baker, Jr.
Professor Mark M. Banaszak Holl
Associate Professor Luming Duan
Associate Professor Cagliyan Kurdak

To my dear parents,

Dongxing Ge and Huandi Xu,

and my beloved wife,

Li Yi

Acknowledgements

My greatest debt is to my advisor Dr. Bradford Orr for the time and efforts that he put in my doctoral education and his personal support. It is under his guidance that I become confident and capable in research and future career. I would like to thank my dissertation committee members for their valuable suggestions and encouragement. I also owe my thanks to former and present group members in MNIMBs (Michigan Nanotechnology Institute for Medicine and Biological Sciences) and the Orr group who have offered generous help and contributed intellectual inputs to my work. They have been great teachers, colleagues, and friends.

Thank my parents who brought me up and encouraged me to be a scientist. Special thanks to my wife Li Yi who walked me throughout my Ph.D. study. And thank all my family members and friends. Without your love and support, I doubt my achievements should ever have been completed.

Table of Contents

List of Figures

List of Tables

Table

CHAPTER 1

Introduction

1.1 Overview

Although the mortality rate of most types of cancer has been continuously declining after 1990, cancer is still the second highest fatal disease in the US.[1] Globally, the death caused by cancer is on the order of 10^7 humans per year.[2] Accompanied by tremendous efforts in improving surgical resection, radiation, and chemotherapy, early diagnosis and detection of tumor cells also attracts great attention. Removing the tumor cells before they grow to a malignant neoplasm may cure several cancer types, such as cervix [3], colon [4] and rectum [5], as well as reduce mortality in other types.[6-8]

High-resolution *in vivo* imaging may serve as the first step in tumor detection and guide further methods to identify the cancer. During the past few decades, technologies such as positron-emission tomography (PET), magnetic resonance imaging (MRI), and computed tomographic scan (CT) were applied to scan the human body to identify tumor formation. However, without a high contrast between the tumor and normal tissues, it is difficult to accurately and unambiguously identify the presence of tumor cells. Therefore, the engineering of “detection-aiding” contrast agents becomes urgent.

Such an agent should contain three major functional components: 1) appropriate biocompatible coating, 2) a targeting moiety, and 3) a reporting moiety. The “detection-

aiding" contrast agent constructed in this study is composed of a functionalized dendrimer coating that displays folate molecules on the surface to facilitate folate-folate receptor interaction.[9] Dendrimers act as a bridge connecting the nanoparticle (NP) core with the targeting moiety and increase the agent's biocompatibility as well. In the core of the complexes are magnetic NPs that are detectable by a sensitive device termed Superconducting Quantum Interference Device (SQUID). Development of this detection method will enrich the knowledgebase of cancer imaging, and stretch the detection limit of tumor formation.

1.2 SQUID

SQUIDs are the most sensitive detectors of magnetic flux. The working principle combines the physical phenomena of flux quantization [10] and Josephson tunneling.[11] There are two types of SQUIDs: *rf* SQUID and *dc* SQUID, the latter of which is the type in this research and is more widely used in biological applications due to lower noise level. The *dc* SQUID will be reviewed here.

1.2.1 Introduction to Superconductivity

Superconductivity describes a phenomenon where many metals show zero resistance to a flow of DC current when the material is below a certain characteristic temperature (T_c). It was discovered by Kamerlingh-Onnes in 1911 that the resistance of mercury abruptly vanished at T = 4.2 K, the boiling point of liquid helium.[12] After that a large number of metallic elements, alloy and compound were found to exhibit superconductivity at various transition temperatures.

Superconductivity is not just perfect conductivity, but also shows magnetically related properties. In 1933, it was found by Walther Meissner and Robert Ochsenfeld that in an external magnetic field once a normal conductor enters the superconducting state, it expels all magnetic flux from its interior.[13] This behavior of maintaining zero magnetic flux density inside a material is called perfect diamagnetism, which is a characteristic property of superconductivity.

However, when the external magnetic field is beyond some certain value, which is termed the critical field (H_c), superconductivity is destroyed and the material transitions back into the normal state. H_c is a temperature dependent variable and the empirical formula states that it becomes higher when temperature decreases.

To understand the physical reason for superconductivity, a number of important phenomenological theories were proposed and successfully explained a lot of the observed phenomena. To name a few, the “two-fluid” model by Gorter and Casimir assumed the electrons in a superconductor can be viewed as a combination of two types: normal and superconducting.[14] The London equation, incorporating the zero resistance of superconductor and perfect diamagnetism, achieved its triumph by explaining the Meissner effect.[15] Further generalization of this equation to the case of strong field was fulfilled by the Ginzburg-Landau theory [16], which integrated the electrodynamic, quantum mechanical and thermodynamic properties of superconductors. A breakthrough was made in 1957 when the first microscopic theory was proposed by John Bardeen, Leon Cooper and Robert Schreiffer to describe superconductivity as an effect of condensation of electron pairs (Cooper pairs), now known as the *BCS* theory.[17] The major success of the *BCS* theory is that the phenomenological theories that we mentioned

previously can be naturally derived from it.[18] However, the *BCS* theory only applies in conventional superconductivity and can not continue its success in the more recent high-temperature class. Despite the lack of a fully successful microscopic explanation of high-T_c materials, superconductivity is a macroscopic quantum phenomenon with long-range order, and this is where the SQUID's working principle originates.

1.2.2 Flux Quantum

The theories of superconductivity brought the prediction of flux quantization in 1950 [10] and the phenomenon was experimentally observed 11 years later.[19, 20] Flux quantization arises from the fact that when a normal state transitions into the ordered superconducting state, the material undergoes a phase transition and the new state can be described by

$$\psi(\vec{r},t) = |\psi(\vec{r},t)| \exp(i\varphi(\vec{r},t)) \tag{1-1}$$

which is a macroscopic wave function of the entire ensemble of superelectrons in the superconductor. It is necessary to consider how an applied magnetic field can affect the wave function. According to the Gauss's law, the applied field ***B*** can be expressed by a vector potential ***A***

$$\vec{B} = \nabla \times \vec{A} \tag{1-2}$$

It can be shown that the effect of ***A*** on the wave function is a multiplication of a factor $\exp(2ie\vec{A}/\hbar)$. Since the wave function must be single valued at any point in the superconductor, this means the phase change around any closed contour must be $2n\pi$.

$$\delta\varphi = \frac{2e}{\hbar}\int \vec{A}\cdot d\vec{l} = 2n\pi \tag{1-3}$$

According to Stoke's theorem,

$$\int \vec{B} \cdot d\vec{S} = \oint \vec{A} \cdot d\vec{l} \tag{1-4}$$

the magnetic flux $\Phi = \int \vec{B} \cdot d\vec{S}$ can only take the following quantized values

$$\Phi = \frac{n\pi\hbar}{e} = \frac{nh}{2e} = n\Phi_0 \tag{1-5}$$

where n is an integer and Φ_0 is called the flux quantum. The value of Φ_0 is small (2.0678×10^{-15} T·m^2), which is approximately 1/25,000 of the flux generated by the Earth magnetic field threading a 1 mm^2 coil. For a singly connected superconductor, as shown in Figure 1.1a, the closed path can be reduced to a path with no length which predicts the magnetic flux has to be zero, i.e. the Meissner effect. The integral along the contour around a hole does not vanish (Figure 1.1b), and there the magnetic flux can take nonzero quantized values.

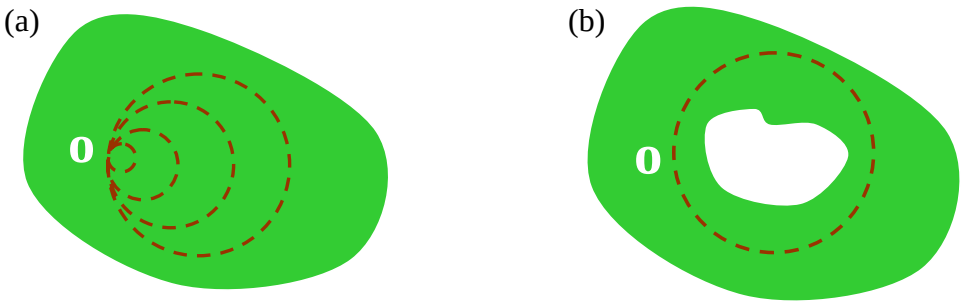

Figure 1.1 The schematic diagram for the explanation of the flux quantum. (a) A single-connected superconductor and (b) a multiple-connected superconductor.

1.2.3 Josephson Effect

When two pieces of superconductors are separated by a small distance, which is on the scale of the coherent length or the penetration depth, they are weakly coupled and form a Josephson junction.[11, 21-23] Common types include point contact junctions, microbridge weak links, SNS and SIS junctions. The last two types consist of a thin

normal conductor (N) or an insulating layer (I) sandwiched by two superconducting electrodes (S), respectively. For the SIS junction with a thin enough barrier, the superelectrons or Cooper pairs can tunnel through the barrier and keep the phase in coherence. It can be shown that the phase difference δ across the weak link is related to the current flowing through the junction by the first Josephson equation [11, 21]:

$$I = I_0 \sin\delta \tag{1-6}$$

where I_0 is the maximum supercurrent or critical current that the junction can support. Any additional current higher than I_0 has to be carried by normal electrons and will experience resistance. Thus a voltage is established across the junction as a function of the phase difference change over time, as described by the second Josephson relation

$$V = \frac{\Phi_0}{2\pi}\frac{d}{dt}\delta \tag{1-7}$$

This is known as the *dc* Josephson Effect. As the biasing current increases from zero, the voltage over the junction remains zero until the critical current value is reached. At that moment, it abruptly jumps to a finite value depending on the properties of the junction.

1.2.4 The *dc* SQUID

If two identical Josephson junctions are connected in parallel to form a loop, the phase of each junction can interfere with each other, which forms a SQUID as illustrated by Figure 1.2a. A steady current I_b is injected into the loop and divided equally by the two branches due to the symmetry of the two junctions. As the external magnetic flux threading the loop varies, the currents in different branches change, which modifies the frequency of phase oscillation, thus influencing the interference between the two currents. It can be proved that the maximum biasing current that can be supplied without

inducing any voltage across the two junctions is modulated by the magnetic flux coupled to the loop:

$$I_{\max} = 2I_0 \left| \cos\left(\pi \frac{\Phi_{ext}}{\Phi_0} \right) \right|. \tag{1-8}$$

In practice, a biasing current slightly higher than $2I_0$ is fed to the SQUID and the voltage V developed across the junctions is measured as a function of the applied magnetic flux. In this way, SQUID acts as a flux-to-voltage transducer with period Φ_0, as shown in Figure 1.2b. To measure small changes in Φ_{ext}, the biasing current is usually set at certain values to maximize the amplitude of the voltage modulation, where $\Phi_{ext} = (2n+1)\Phi_0 / 4 \quad (n = 0,1,2,...)$ meaning the maximum slope of the V-Φ curve.

Due to the sinusoidal relationship of the V-Φ curve, the proportionality between voltage and flux is maintained only for a very small flux change. For practical application, the linear range has to be extended by using a flux-locked loop (FLL). The deviation in voltage from the working point is amplified, integrated and fed back into the SQUID loop through a feedback resistor and a mutually coupled inductor, thus keeping the flux in the SQUID constantly at the optimum working point. The optimum working point is arbitrary as long as it is kept at the maximum V-Φ slope, which means the absolute value of a static field can not be measured by SQUID.

It is not possible to directly use the SQUID loop as the sensor due to its low inductance, maintained to minimize noise. Different types of pick-up coils were designed and coupled to the SQUID loop to sense the field, which also allows flexible spatial sensitivity by changing the shape of the detection coils. The common designs of pick-up coils include magnetometer, first-order and second-order gradiometer, as displayed in

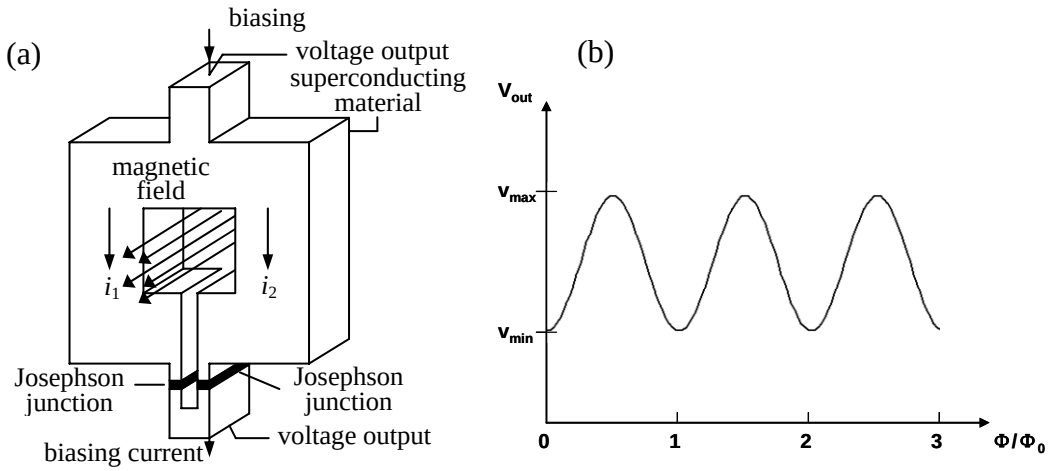

Figure 1.2 (a) The diagram of a *dc* SQUID (b) a typical *V*-Φ characteristic curve of *dc* SQUID. The output voltage is a periodic function of Φ with period of Φ_0.

Figure 1.3. The magnetometer has the simplest detection coil made of a single turn or a few turns of superconducting wire. It's easy to integrate within the SQUID chip but responds to any magnetic flux change through the coil. By connecting two magnetometer coils with opposite polarities while separating them at a certain distance, a first-order gradiometer is constructed. The coils can be placed either along their axis (axial gradiometer) or in their plane (planar gradiometer). For an ideally balanced pick-up coil, a uniform field couples zero SQUID signal while the gradient can be sensed. The advantage of this design is the cancellation of the uniform field changes through the two magnetometer coils, which allows sensitive detection of weak signals against a background that can be many orders higher. Based on this, a second-order gradiometer can be constructed in a similar way by connecting two first-order gradiometers together with opposite orientations. It does not respond to both uniform field and the gradient but only measures the second-order spatial changes. The SQUID that was used in these studies has this type of pick-up coil configuration.

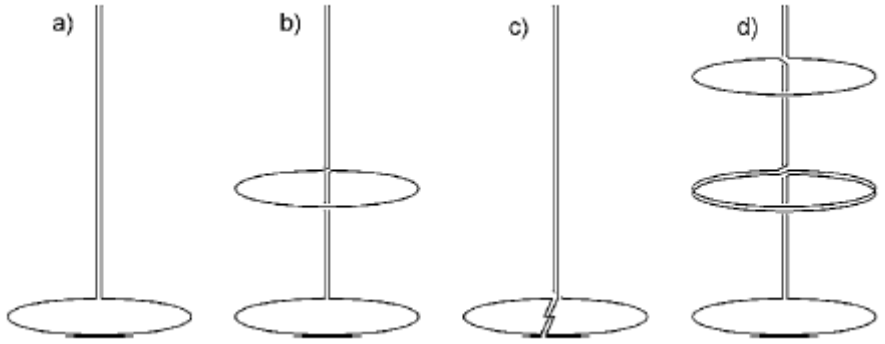

Figure 1.3 Common types of SQUID pick-up coil configurations. (a) Magnetometer, (b) first order axial gradiometer, (c) first order planer gradiometer, and (d) second order axial gradiometer.

1.3 Magnetic Nanoparticles

The term “magnetic nanoparticles” refers the two things: the property and the dimension of the material. “Magnetic” is commonly used for the phenomena of ferromagnetism and ferrimagnetism [24], which are two of the many types of magnetic behaviors. The prefix “nano-” refers to a class of materials, the size of which is in the nanometer scale (often 100nm or smaller).[25] The small size of the particles creates a number of unique properties that the bulk materials do not possess and thus have wide applications, such as high-density information storage [26-28], ferrofluids [29], spintronics [30-32] and many biological applications [25, 33-35] including cell type recognition [36], drug delivery [37, 38], targeted therapeutics [39-41], and intracellular imaging.[9, 42, 43]

1.3.1 Magnetic Properties

1.3.1.1 Diamagnetism

All materials exhibit a diamagnetic response in the presence of a magnetic field. In the classical view of an atom, the electrons are orbiting the nucleus and forming current loops. When an external field is applied, the orbital motion of electrons alters in such a way to oppose the applied field, as predicted by the Len's law. This behavior results in negative susceptibility and causes the material to be repelled by the field. The diamagnetic interaction is weak and disappears when the applied field is removed. Diamagnetic susceptibilities are very small, on the order of 10^{-6} ~ 10^{-4}.[44] Diamagnetism will be dominated when materials are either paramagnetic or ferromagnetic, so it is observable for the atoms with paired electrons only. Examples are molecular hydrogen, water, copper, sodium chloride and all noble gases.

1.3.1.2 Paramagnetism

As opposed to diamagnetism, paramagnetic materials show weak attractions to strong magnets. It originates from the spin and orbital magnetic moments of unpaired electrons.[24, 45] Each atom or molecule can be regarded as a dipole moment and the applied magnetic field tends to align these moments in the direction of the field. The level of alignment is affected by thermal fluctuations, so the magnetization is dependent on temperature which can be described by the Langevin function.[24] Magnetic susceptibilities due to paramagnetism are positive but also very small: on the order of 10^{-3} to 10^{-5}.[46] Similar to diamagnetism, paramagnetic response to field vanishes on the removal of the external magnetic field. Materials belonging to this category include aluminum, manganese, oxygen and rare earth ions.

1.3.1.3 Ferromagnetism and Ferrimagnetism

Materials having similar magnetic properties as iron, nickel and cobalt, which can naturally attract small iron pieces, are said to be ferromagnetic. The property can not be accounted for by the behavior of individual atoms as diamagnetism and paramagnetism. The magnetic moments of adjacent atoms interact so strongly that they preferentially align in parallel with each other, which is called spontaneous magnetization. The Hisenburg exchange energy is proposed to explain this self-alignment of the magnetic moments [47] because the phenomenon is contradictory to the classical electromagnetism. There exists a critical temperature called the Curie point (T_c), beyond which the spontaneous magnetization vanishes and the material behaves in a paramagnetic way.

The ferromagnetic magnetization is not only determined by the strength of the applied field, but also depends on its previous magnetic history (hysteresis). As the biasing field increases, the induced magnetization reaches a maximal value, which is called the saturation magnetization (M_{sat}). After the field is removed, the material still has some residuals magnetism, termed remanence (M_r). An opposite field, which is named the coercive force (H_c), needs to be applied to completely set the magnetization back to zero. According to the magnitude of M_r and H_c, ferromagnetic materials can be further categorized into soft ferromagnetic and hard ferromagnetic.

In bulk materials, it is more energetically favorable to form small regions with opposing magnetization, each of which is spontaneously magnetized and has a net magnetic moment. These regions are called domains and the barriers between adjacent domains are domain walls. Unmagnetized ferromagnetic bulk contains multiple domains

with random orientations so that it displays not net magnetization. As a magnetic field is applied, the domains along the direction of the field expand to other domains thus producing the macroscopic moment. Due to this mechanism of magnetization, the susceptibilities of ferromagnetic materials can be as high as 10^3 to 10^6.

Ferrimagnetic substances have similar magnetic properties as ferromagnetic materials: spontaneous magnetization, hysteresis loops and Curie temperature, but typically have smaller magnetic moments than the ferromagnetic materials. It can be microscopically viewed as two self-aligned sub-lattices with net moments that are in antiparallel orientation with each other. A net magnetization can be observed if the moments of the two sub-lattices are not equal. (In the case of equal moments antiferromagnetism occurs.) Magnetite (Fe_3O_4) is a well known ferrimagnetic material, which was considered ferromagnetic until the work done by Néel in the 1904's.[48]

1.3.1.4 Superparamagnetism

The superparamagnetism theory was first developed by Néel [49], and is the unique property possessed by nano-scaled magnetic particles. Substances with this property behave similarly to paramagnetic, showing no remanence in the absence of magnetic field. However, the susceptibilities of superparamagnetic materials are comparable to those of ferromagnetism because they are ferro- or ferrimagnetic fine particles. When the ferro- or ferrimagnetic materials become so small that the energy of establishing domain walls is larger than the magnetostatic energy caused by paralleled moments [50], particles prefer to stay with single domains. The critical size of single domain particle forming varies with the material of the NPs, but typically within the range of 10 to 100 nm [50, 51]. As an example, the critical size for Fe_3O_4 is 70 nm.[52] In

a single domain, there exists a particular direction which the magnetization is energetically preferable to take. This direction is usually referred to as the easy axis and the associated phenomenon is called magnetic anisotropy.

The zero remanence property is the outcome of small particle size when the thermal energy is high enough to fluctuate and randomize the particles' moments to cause the net magnetization loss in the absence of an applied field. There are two mechanisms related to the process of the magnetization diminishing: Brownian relaxation and Néel relaxation.[53-55] The Brownian relaxation is caused by the physical rotation of the particles, which is described by

$$\tau_B = 3V_H \eta / k_B T \tag{1-9}$$

where V_H is the hydrodynamic volume of the particle, η is the viscosity of the medium, k_B is the Boltzmann constant and T is the absolute temperature. The Néel relaxation happens when the particle becomes much smaller than the critical domain size so that the internal magnetic moment can overcome the energy barrier created by the easy axis due to the thermal excitation.[56] The rotation results in random moment orientations and the magnetization change over time is characterized by

$$\tau_N = \tau_0 \exp(KV / k_B T) \tag{1-10}$$

where τ_0 is usually quoted as 10^{-9} s [57], K is the anisotropy constant, and KV means the height of the energy barrier. The Néel relaxation time constant is exponentially dependent on the volume of particles hence changing much faster with size than the Brownian time constant. Both of these two relaxation processes are present during demagnetization and the effective time constant is

$$\tau_{eff} = \frac{\tau_B \tau_N}{\tau_B + \tau_N}. \quad (1\text{-}11)$$

An example is given in Figure 1.4 by assuming η takes the value of the viscosity of water 10^{-3} kg/m·s , the anisotropy constant is 20 kJ/m^3 which is a typical value of Fe_3O_4 NPs [58, 59] at $T = 300K$. As the particle size changes, the Brownian relaxation time constant is always around μsec or lower, relatively constant compared with the value of the Néel process which spans many orders of magnitude. This provides the basis of applying the magnetic NPs as *in vivo* contrast agent for SQUID detection.

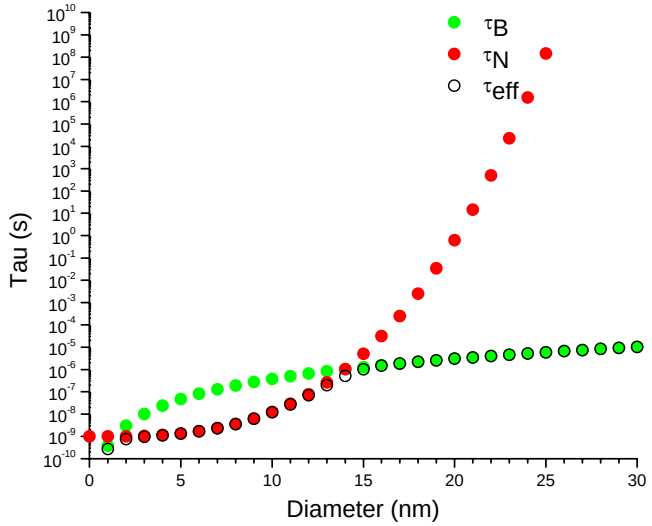

Figure 1.4 Comparison of the Brownian, Néel and effective relaxation time constants on different sizes of Fe_3O_4 NPs by assuming η = 10^{-3}kg/m·s and K = 20kJ/m^3 at T = 300K.

1.3.2 Why "Nanoparticles"?

The application of NPs to biological systems is attractive and promising because of their (1) small size and consequently high surface-to-volume ratio, (2) tailorable physical and chemical properties related to size, shape and composition (3) modifiable surface properties (4) robust structure and stableness. The size advantage of NPs over the

bulk counterpart enables them to function at the cellular and molecular level with the biological entities.[60-64] The high surface-to-volume ratio provides more area for the NPs to carry multiple functional groups to modify the bio-interactions.[54, 63, 65] The size, shape and composition can be systematically varied to produce NPs with specific optical, electrical and magnetic properties suitable for the detection method.[66-71] The advances in techniques for surface modification allow nanoscale arrays of small molecules and biomacromolecules to be conjugated with the NPs.[72-74] Moreover, the NPs can now be synthesized into chemically stable and uniform colloids for in vivo injection.[54, 64, 65]

1.3.3 Targeted Magnetic NPs as Contrast Agent

The idea of targeting the functionalized magnetic NPs to specific biological tissue to increase the imaging contrast is widely used in the magnetic resonance imaging (MRI) technique.[75-77] MRI is one of the best available clinical imaging tools due to its noninvasive nature and decent spatial resolution.[78, 79] Clinically, MRI measures the magnetic relaxation time of protons of water molecules in biological systems and produces intensity maps of tissues. Contrast arises from variations in the density of protons and relaxation times over the body. The targeted magnetic NPs can enhance the contrast by interacting with surrounding water and decreasing the relaxation time of the nearby protons.[78, 80-82] SQUID, as the most sensitive magnetic detector, can sense minute signals from targeted NPs and is under intensive studies, which will be reviewed later in this chapter.

The targeting of NPs can be achieved in two basic modes: passive and active. Passive targeting can occur through the enhance permeability and retention (EPR) effect

[83, 84], which is based on the finding that unhealthy tissues have “leaky” vasculature allowing the NPs to extravasate and accumulate more easily in lesions. A more specific targeting scheme is to conjugate the NPs with molecules that have high affinity to the unique molecular signature of the malignant cells, which is called active targeting.[85] Common strategies utilize the antigen-antibody [86-88] and ligand-receptor interactions [89-91] to increase the residence time on the target. Targeting ligands include proteins [92], peptides [93], aptamers [94-96] and small molecules.[97] For the purpose of targeting cancer, folic acid (FA) is a promising candidate. This ligand has a receptor that is overexpressed on the membrane of a wide range of human cancer cells, including breast, ovary, lung, kidney, endometrium and brain.[98-100] Although normal cells also express folic acid receptors (FARs), the level of expression in malignant tissues is much higher and increases as the cancer grows.[101] Many studies have been carried out and showed specific binding of FA conjugated NPs to a number of tumor cells.[102-104] The small size of FA molecules provides advantages over proteins or peptides in that FA is more robust and therefore reduces the possibility of losing functionality during the synthesis of magnetic NPs. The conjugation of FA to magnetic NPs can be achieved by using Poly(amidoamine) (PAMAM) dendrimers as scaffolds, as demonstrated by the work of our group.[39, 105, 106]

1.4 SQUID Detection of Magnetic NPs

SQUID imaging, a non-invasive method, has been used, but not extensively, in past studies to track the naturally occurring magnetic particles in human organs. Examples include examining human liver iron stores [107] and iron accumulation in lungs.[108] As synthetic techniques have developed, magnetic NPs with better bio-

compatibility and multiple functionality were achieved and more studies were performed on applying SQUID to targeted MNPs, such as locating the sentinel lymph node for breast cancer detection [109] and biological immunoassays.[110-112] Based on the NPs' magnetic properties, primarily three methods were developed for detection of the magnetic signal emanating from them: susceptibility [113-117], remanence [118-122] and relaxivity [123-127] based measurements. The relaxivity based measurement is also known as magnetorelaxometry (MRX). In all of these methods, the detection is based on changes in the magnetic field produced by the magnetic NPs.

1.4.1 Magnetic Susceptibility Based SQUID Measurement

The susceptibility measurement can be divided into DC susceptibility [113, 114, 116] and AC susceptibility [115, 117], where a magnetic field is maintained during the measurement. In the DC method, a constant magnetic field is applied parallel to the SQUID pick-up coil and the NPs are collectively moved to generate magnetic flux changes through the coil. The AC susceptibility measurement alternates the magnetizing field thus creating the oscillation of signals. In either scheme, the applied field is usually several orders of magnitude higher (10^{-4} T) than the signal generated by the magnetic NPs (10^{-11} ~ 10^{-8} T). Therefore, careful adjustment of the SQUID sensor's position is necessary and compensation coils are sometimes required to minimize the net flux in the pick-up coil caused by the biasing field. Because different research groups measured the NP samples at different distances from the SQUID sensor, there's no direct way to compare their detection limit. Typically, at a distance around a millimeter or so the detection limit is about 10^{-1} ~ 10^{0} ng and at distance close to 1 cm the lowest detectable

amount is about 10^2 ~ 10^3 ng. This sensitivity variation with distance agrees with the $1/r^3$ rule of the magnetic field of a dipole moment.

The biggest advantage of susceptibility measurement is that all NPs have contribution to the signal regardless of their individual size. However, due to imperfect balance or pick-up coil vibration, the magnetizing field can cause so large a background noise that prevents the detection limit to be further enhanced. Furthermore, this method has only been applied with SQUID magnetometers or planer gradiometers because it's possible to create a uniform B-field in a small region and compensate the background flux residual through the detector only for simple coil configurations.

1.4.2 Remanence Based SQUID Measurement

Since the Néel relaxation time constant is exponentially dependent on the particle's volume, the magnetic particle size does not need to be too large to display remanence. Iron oxide NPs of 25 nm in diameter have been proven to exhibit magnetic remanence and commonly used in SQUID remanence measurement.[118-122] The typical procedure is to magnetize the NPs in a strong field (10^{-1} to 10^0 T) far enough from the SQUID, then move the magnetized sample near the detector (usually at a speed of 10^1 ~ 10^2 mm/s) and recording the signal. Again, the detection limit is dependent on the distance between the sample and the SQUID sensor, which after conversion is about 10^0 ~ 10^1 ng at a centimeter separation.

The remanence measurement is by far the most sensitive among the three methods because the absence of the external field greatly reduces the background noise and allows the sensitivity of SQUID to be fully realized. By choosing large enough NPs which show remanence, the majority of them give signal contribution. Moreover, the system is easy to

set up and the operation is relatively simple. The limitation of increasing the detection limit comes from the magnetic contaminations in the sample holder which moves along with the sample thus creating false positive signals. Applying the remanence detection to *in vivo* imaging is more challenging due to the biomagnetism [128] and the existence of endogenous magnetic NPs.[129] Current remanence methods were developed by moving the sample in a horizontal plane (either circular or linear), which limits the application to building a scanning system.

1.4.3 SQUID Magnetorelaxometry (MRX)

MRX is the most commonly used technique in the SQUID detection of magnetic NPs and takes the advantage of the superparamagnetic property.[123-127] The whole procedure can be broken down into several steps:

(1) deactivate the SQUID so that it doesn't respond to any magnetic field change;

(2) apply a biasing field to magnetize the NPs;

(3) turn off the biasing field;

(4) after a short delay, reactivate the SQUID and start data acquisition.

As the technique was being developed, the experimental parameters used in the above procedures varied by a considerable amount.[124, 126, 130, 131] But today these numbers are converging on an optimum. Typical values are 10 ~ 30 Gauss for the magnetizing field, 15 ~ 30 ms of the delay time and 1 ~ 2 sec for data taking. The MRX detection limit is not as high as that for remanence detection, about 10^3 ng at a converted 1 cm distance. One group has claimed a 17 ng detection limit of Fe_3O_4 NPs at 2 cm in an unshielded environment, however did not provide the data of any nanogram samples.[132] In their later publication [133], the deducted magnetic signal for 17 ng

from higher masses is much lower than the ambient noise, which means this amount can hardly be detected.

SQUID-MRX, similar to the remanence method, has a low noise level because no magnetic filed is present during the measurement. It is very sensitive to the magnetic NPs' size due to the exponential form of the Néel relaxation. This property is both an advantage and disadvantage of this technique. According to the different time scales of Brownian and Néel relaxation (Figure 1.4), NPs above a certain size has much shorter Brownian relaxation time than Néel time. For *in vivo* applications, contrast will be established between unbound and bound particles. Importantly, biomagnetism and endogenous NPs will not have the same relaxation time scale as the injected NPs, thus will not be observed. However, the sensitive size dependence means not all NPs contribute to signal, because some decay either too fast (small) or too slow (large) and are undetectable within the measurement time window. This puts limit on the sensitivity and requires monodispersed NPs to be synthesized. Also, the rapid quenching of the biasing field is handled by a special electrical circuit, which complicates the system setup.

1.4.4 SQUID versus Other Cancer Detection Techniques

SQUID imaging is a promising complementary method to the prevailing cancer detection techniques, including ultrasound, PET (Positron Emission Tomography), CT (Computational Tomography) and MRI due to its non-invasive nature. SQUID detects magnetic signals from the magnetic contrast agents, which can penetrate the human body. This offers an advantage over ultrasound because of the reflection of sound from tissue to gas and inability to pass through the bone. And the magnetism-based detection, which is

also used in MRI, makes SQUID imaging superior to PET and CT scans where the radiation exposure is unavoidable.

Compared with MRI, SQUID imaging system of cancer cells by using magnetic NPs as contrast agents is still in its infancy. It is attractive due to its extremely high sensitivity which offers the possibility of early stage tumor diagnosis. Moore *et al.* has achieved concentrations between 11.9 and 118 ng of Fe per million tumor cells [134] and Lewin *et al.* showed even higher concentration (10 – 30 μg per million cells).[135] Based on the current sensitivity achieved by the SQUID measurement, it is very possible to detect 10^6 cells (1 mm^3) at a few centimeters away. Besides, SQUID detection is quantitative and more reliable because it provides a direct measurement of the amount magnetic NPs while the MRI signal is an indirect reflection of the contrast agents and is affected by their distribution. Because of the large magnetic field, MRI is not suitable for people with a cardiac pacemaker, cerebral aneurysm clips and any metallic fragment near eyes or blood vessels. The last advantage is that the SQUID system is more financially affordable without the need of building the strong magnet. The SQUID imaging system, as a complementary tool to MRI, has significant potential and deserves attention.

1.5 Dissertation Rationale

The ultimate goal of this dissertation is to develop a SQUID detection system of magnetic NPs for potential *in vivo* cancer imaging. A wide range of techniques and methods have been applied such as system automation, circuit design, synthetic chemistry, nanomaterial characterization, theoretical modeling and computational simulation.

Chapter 2 talks about the remanence based measurement system with 1D scanning ability developed in my research. For imaging purposes, vertical oscillation is utilized to save the horizontal motion for translational scanning. Sensitivity and spatial resolution related to this system will be discussed. A theoretical model is brought forward, which can quantitatively determine the masses and positions of NPs from the scanned images, especially the depth. Because of the advantages of the MRX method, a MRX system is also established, which is described in chapter 3. Detailed discussions are provided on how the technical difficulties can be conquered, such as fast field switching and noise reduction. The particle size dependence of the SQUID signal is tested in experiments on NPs in sizes sorted by centrifugation. A series of commercially available NP samples are measured to explore the method's best sensitivity and computer simulations are employed to help explaining the possibility of sensitivity improvement. Since commercial NPs do not have variable size and modifiable surfaces, a synthetic route which allows particle size control and FA conjugation for targeting purposes is needed. In chapter 4, I introduce a hydrothermal synthesis method for Fe_3O_4 NPs and show the magnetic properties of the as-synthesized NPs can be tuned by varying the chemical reagent concentrations. SQUID-MRX calibrations are performed on these NPs, followed by functionalization and *in vitro* application of the NPs under MRX measurements.

1.6 Reference

1. *Cancer facts and figures*, A.C. Society, 2008.

2. *Global cancer facts and figures*, A.C. Society, 2007.

3. Bazant-Hegemark, F., et al., *Review: optical micrometer resolution scanning for non-invasive grading of precancer in the human uterine cervix.* Technol Cancer Res Treat, 2008. **7**(6): p. 483-96.

4. Mano, M.S. and F. Duhoux, *Colon cancer: update on adjuvant therapy.* Clin Colorectal Cancer, 2008. **7**(3): p. 178-83.

5. Heron, D.E., et al., *PET-CT in radiation oncology: the impact on diagnosis, treatment planning, and assessment of treatment response.* Am J Clin Oncol, 2008. **31**(4): p. 352-62.

6. Brooks, M., *Breast cancer screening and biomarkers.* Methods Mol Biol, 2009. **472**: p. 307-21.

7. Klapman, J. and M.P. Malafa, *Early detection of pancreatic cancer: why, who, and how to screen.* Cancer Control, 2008. **15**(4): p. 280-7.

8. Spangenberg, H.C., R. Thimme, and H.E. Blum, *Advances in prevention and diagnosis of hepatocellular carcinoma.* Expert Rev Gastroenterol Hepatol, 2008. **2**(3): p. 425-33.

9. Wang, S.H., et al., *Dendrimer-functionalized iron oxide nanoparticles for specific targeting and imaging of cancer cells.* Adv. Funct. Mater., 2007. **17**(16): p. 3043-3050.

10. London, F., *Superfluids*. 1950, New York: Wiley.

11. Josephson, B.D., *Possible New Effects in Superconductive Tunnelling.* Physics Letters, 1962. **1**(7): p. 251-253.

12. Onnes, H.K., *Further experiments with liquid helium G on the electrical resistance of pure metals, etc VI On the sudden change in the rate at which the resistance of mercury disappears.* Proceedings of the Koninklijke Akademie Van Wetenschappen Te Amsterdam, 1912. **14**: p. 818-819.

13. Meissner, W. and R. Ochsenfeld, *Short initial announcements.* Naturwissenschaften, 1933. **21**: p. 787-788.

14. Gorter, C.J. and H. Casimir, *On supraconductivity I.* Physica, 1934. **1**: p. 306-320.

15. London, F. and H. London, *The electromagnetic equations of the supraconductor.* Proceedings of the Royal Society of London Series a-Mathematical and Physical Sciences, 1935. **149**(A866): p. 0071-0088.

16. Ginzburg, V.L. and L.D. Landau, Zh. Eksperim. i Teor. Fiz., 1950. **20**: p. 1064.

17. Bardeen, J., L.N. Cooper, and J.R. Schrieffer, *Microscopic Theory of Superconductivity.* Physical Review, 1957. **106**(1): p. 162-164.

18. Gorkov, L.P., *Microscopic Derivation of the Ginzburg-Landau Equations in the Theory of Superconductivity.* Soviet Physics Jetp-Ussr, 1959. **9**(6): p. 1364-1367.

19. Deaver, B.S. and W.M. Fairbank, *Experimental Evidence for Quantized Flux in Superconducting Cylinders.* Physical Review Letters, 1961. **7**(2): p. 43-&.

20. Doll, R. and M. Nabauer, *Experimental Proof of Magnetic Flux Quantization in a Superconducting Ring.* Physical Review Letters, 1961. **7**(2): p. 51-&.

21. Josephson, B.D., *Supercurrents through Barriers.* Advances in Physics, 1965. **14**(56): p. 419-&.

22. Likharev, K.K., *Dynamics of Josephson Junctions and Circuits*. 1986, New York: Gordon and Breach.

23. Barone, A. and G. Paterno, *Physics and Application of the Josephson Effect*. 1982, New York: John Wiley & Sons.

24. Willard, M.A., et al., *Chemically prepared magnetic nanoparticles.* International Materials Reviews, 2004. **49**(3-4): p. 125-170.

25. Moghimi, S.M., A.C. Hunter, and J.C. Murray, *Nanomedicine: current status and future prospects.* Faseb Journal, 2005. **19**(3): p. 311-330.

26. Black, C.T., et al., *Spin-dependent tunneling in self-assembled cobalt-nanocrystal superlattices.* Science, 2000. **290**(5494): p. 1131-1134.

27. Goya, G.F., et al., *Static and dynamic magnetic properties of spherical magnetite nanoparticles.* Journal of Applied Physics, 2003. **94**(5): p. 3520-3528.

28. Matsunaga, T., *Applications of Bacterial Magnets.* Trends in Biotechnology, 1991. **9**(3): p. 91-95.

29. Raj, K., B. Moskowitz, and R. Casciari, *Advances in Ferrofluid Technology.* Journal of Magnetism and Magnetic Materials, 1995. **149**(1-2): p. 174-180.

30. Li, C., et al., *Synthesis, electronic properties, and applications of indium oxide nanowires.* Molecular Electronics Iii, 2003. **1006**: p. 104-121.

31. Liao, Z.M., et al., *Spin-filter effect in magnetite nanowire.* Nano Letters, 2006. **6**(6): p. 1087-1091.

32. Lu, Z.L., et al., *Large low-field magnetoresistance in nanocrystalline magnetite prepared by sol-gel method.* Journal of Physical Chemistry B, 2006. **110**(47): p. 23817-23820.

33. Daniel, M.C. and D. Astruc, *Gold nanoparticles: Assembly, supramolecular chemistry, quantum-size-related properties, and applications toward biology, catalysis, and nanotechnology.* Chemical Reviews, 2004. **104**(1): p. 293-346.

34. Parak, W.J., et al., *Biological applications of colloidal nanocrystals.* Nanotechnology, 2003. **14**(7): p. R15-R27.

35. Rosi, N.L. and C.A. Mirkin, *Nanostructures in biodiagnostics.* Chemical Reviews, 2005. **105**(4): p. 1547-1562.

36. Shen, L.F., P.E. Laibinis, and T.A. Hatton, *Bilayer surfactant stabilized magnetic fluids: Synthesis and interactions at interfaces.* Langmuir, 1999. **15**(2): p. 447-453.

37. Kukowska-Latallo, J.F., et al., *Nanoparticle targeting of anticancer drug improves therapeutic response in animal model of human epithelial cancer.* Cancer Research, 2005. **65**(12): p. 5317-5324.

38. Thomas, T.P., et al., *Tissue distribution and real-time fluorescence measurement of a tumor-targeted nanodevice by a two photon optical fiber fluorescence probe - art. no. 60950Q.* Nanobiophotonics and Biomedical Applications III, 2006. **6095**: p. Q950-Q950

39. Quintana, A., et al., *Design and function of a dendrimer-based therapeutic nanodevice targeted to tumor cells through the folate receptor.* Pharmaceutical Research, 2002. **19**(9): p. 1310-1316.

40. Majoros, I.J., et al., *Poly(amidoamine) dendrimer-based multifunctional engineered nanodevice for cancer therapy.* Journal of Medicinal Chemistry, 2005. **48**(19): p. 5892-5899.

41. Thomas, T.P., et al., *Targeting and inhibition of cell growth by an engineered dendritic nanodevice.* Journal of Medicinal Chemistry, 2005. **48**(11): p. 3729-3735.

42. Morawski, A.M., G.A. Lanza, and S.A. Wickline, *Targeted contrast agents for magnetic resonance imaging and ultrasound.* Current Opinion in Biotechnology, 2005. **16**(1): p. 89-92.

43. Mornet, S., et al., *Magnetic nanoparticle design for medical diagnosis and therapy.* Journal of Materials Chemistry, 2004. **14**(14): p. 2161-2175.

44. Pankhurst, Q.A., et al., *Applications of magnetic nanoparticles in biomedicine.* Journal of Physics D-Applied Physics, 2003. **36**(13): p. R167-R181.

45. Skomski, R., *Nanomagnetics.* Journal of Physics-Condensed Matter, 2003. **15**(20): p. R841-R896.

46. Saini, S., et al., *Magnetism - a Primer and Review.* American Journal of Roentgenology, 1988. **150**(4): p. 735-743.

47. Buschow, K.H.J. and F.R. de Boer, *Physics of Magnetism and Magnetic Materials*. 2003, New York: Kluwer Academic Publishers Group.

48. Néel, L., *Antiferromagnetism and Ferrimagnetism.* Proceedings of the Physical Society of London Section A, 1952. **65**(395): p. 869-885.

49. Néel, L., Ann. Geophys., 1949. **5**: p. 99-136.

50. Batlle, X. and A. Labarta, *Finite-size effects in fine particles: magnetic and transport properties.* Journal of Physics D-Applied Physics, 2002. **35**(6): p. R15-R42.

51. Lu, A.H., E.L. Salabas, and F. Schuth, *Magnetic nanoparticles: Synthesis, protection, functionalization, and application.* Angewandte Chemie-International Edition, 2007. **46**(8): p. 1222-1244.

52. LesliePelecky, D.L. and R.D. Rieke, *Magnetic properties of nanostructured materials.* Chemistry of Materials, 1996. **8**(8): p. 1770-1783.

53. Fannin, P.C., B.K.P. Scaife, and S.W. Charles, *The Measurement of the Frequency-Dependent Susceptibility of Magnetic Colloids.* Journal of Magnetism and Magnetic Materials, 1988. **72**(1): p. 95-108.

54. Vatta, L.L., R.D. Sanderson, and K.R. Koch, *Magnetic nanoparticles: Properties and potential applications.* Pure and Applied Chemistry, 2006. **78**(9): p. 1793-1801.

55. Wilson, S.A., et al., *New materials for micro-scale sensors and actuators An engineering review.* Materials Science & Engineering R-Reports, 2007. **56**(1-6): p. 1-129.

56. Gubin, S.P., et al., *Magnetic nanoparticles: Preparation methods, structure and properties.* Uspekhi Khimii, 2005. **74**(6): p. 539-574.

57. Néel, L., *Some Theoretical Aspects of Rock-Magnetism.* Advances in Physics, 1955. **4**(14): p. 191-243.

58. Fannin, P.C. and S.W. Charles, *Measurement of the Neel Relaxation of Magnetic Particles in the Frequency-Range 1khz to 160mhz.* Journal of Physics D-Applied Physics, 1991. **24**(1): p. 76-77.

59. Fannin, P.C. and S.W. Charles, *On the Calculation of the Neel Relaxation-Time in Uniaxial Single-Domain Ferromagnetic Particles.* Journal of Physics D-Applied Physics, 1994. **27**(2): p. 185-188.

60. Azzazy, H.M.E., M.M.H. Mansour, and S.C. Kazmierczak, *Nanodiagnostics: A new frontier for clinical laboratory medicine.* Clinical Chemistry, 2006. **52**(7): p. 1238-1246.

61. Krishnan, K.M., et al., *Nanomagnetism and spin electronics: materials, microstructure and novel properties.* Journal of Materials Science, 2006. **41**(3): p. 793-815.

62. Tartaj, P., et al., *The preparation of magnetic nanoparticles for applications in biomedicine.* Journal of Physics D-Applied Physics, 2003. **36**(13): p. R182-R197.

63. Tartaj, P., et al., *Advances in magnetic nanoparticles for biotechnology applications.* Journal of Magnetism and Magnetic Materials, 2005. **290**: p. 28-34.

64. Xu, C.J. and S.H. Sun, *Monodisperse magnetic nanoparticles for biomedical applications.* Polymer International, 2007. **56**(7): p. 821-826.

65. Portet, D., et al., *Nonpolymeric coatings of iron oxide colloids for biological use as magnetic resonance imaging contrast agents.* Journal of Colloid and Interface Science, 2001. **238**(1): p. 37-42.

66. Sun, Y.G. and Y.N. Xia, *Shape-controlled synthesis of gold and silver nanoparticles.* Science, 2002. **298**(5601): p. 2176-2179.

67. Chiang, I.C. and D.H. Chen, *Synthesis of monodisperse FeAu nanoparticles with tunable magnetic and optical properties.* Advanced Functional Materials, 2007. **17**(8): p. 1311-1316.

68. Vestal, C.R. and Z.J. Zhang, *Synthesis and magnetic characterization of Mn and Co spinel ferrite-silica nanoparticles with tunable magnetic core.* Nano Letters, 2003. **3**(12): p. 1739-1743.

69. Xie, J., et al., *One-pot synthesis of monodisperse iron oxide nanoparticles for potential biomedical applications.* Pure and Applied Chemistry, 2006. **78**(5): p. 1003-1014.

70. Jin, R.C., et al., *Photoinduced conversion of silver nanospheres to nanoprisms.* Science, 2001. **294**(5548): p. 1901-1903.

71. Sau, T.K. and C.J. Murphy, *Room temperature, high-yield synthesis of multiple shapes of gold nanoparticles in aqueous solution.* Journal of the American Chemical Society, 2004. **126**(28): p. 8648-8649.

72. Ginger, D.S., H. Zhang, and C.A. Mirkin, *The evolution of dip-pen nanolithography.* Angewandte Chemie-International Edition, 2004. **43**(1): p. 30-45.

73. Kenseth, J.R., et al., *Investigation of approaches for the fabrication of protein patterns by scanning probe lithography.* Langmuir, 2001. **17**(13): p. 4105-4112.

74. Wadu-Mesthrige, K., et al., *Fabrication and imaging of nanometer-sized protein patterns.* Langmuir, 1999. **15**(25): p. 8580-8583.

75. Corot, C., et al., *Recent advances in iron oxide nanocrystal technology for medical imaging.* Advanced Drug Delivery Reviews, 2006. **58**(14): p. 1471-1504.

76. McCarthy, J.R. and R. Weissleder, *Multifunctional magnetic nanoparticles for targeted imaging and therapy.* Advanced Drug Delivery Reviews, 2008. **60**(11): p. 1241-1251.

77. Sun, C., J.S.H. Lee, and M.Q. Zhang, *Magnetic nanoparticles in MR imaging and drug delivery.* Advanced Drug Delivery Reviews, 2008. **60**(11): p. 1252-1265.

78. Artemov, D., *Molecular magnetic resonance imaging with targeted contrast agents.* Journal of Cellular Biochemistry, 2003. **90**(3): p. 518-524.

79. Weissleder, R., *Molecular imaging in cancer.* Science, 2006. **312**(5777): p. 1168-1171.

80. Bulte, J.W.M. and D.L. Kraitchman, *Iron oxide MR contrast agents for molecular and cellular imaging.* Nmr in Biomedicine, 2004. **17**(7): p. 484-499.

81. Lawaczeck, R., M. Menzel, and H. Pietsch, *Superparamagnetic iron oxide particles: contrast media for magnetic resonance imaging.* Applied Organometallic Chemistry, 2004. **18**(10): p. 506-513.

82. Sunderland, C.J., et al., *Targeted nanoparticles for detecting and treating cancer.* Drug Development Research, 2006. **67**(1): p. 70-93.

83. Maeda, H., *The enhanced permeability and retention (EPR) effect in tumor vasculature: The key role of tumor-selective macromolecular drug targeting.* Advances in Enzyme Regulation, Vol 41, 2001. **41**: p. 189-207.

84. Maeda, H., et al., *Tumor vascular permeability and the EPR effect in macromolecular therapeutics: a review.* Journal of Controlled Release, 2000. **65**(1-2): p. 271-284.

85. Weissleder, R., A. Bogdanov, and M. Papisov, *Drug targeting in magnetic resonance imaging.* Magn Reson Q, 1992. **8**(1): p. 55-63.

86. Hu, F.Q., et al., *Preparation of biocompatible magnetite nanocrystals for in vivo magnetic resonance detection of cancer.* Advanced Materials, 2006. **18**(19): p. 2553-+.

87. Huh, Y.M., et al., *In vivo magnetic resonance detection of cancer by using multifunctional magnetic nanocrystals.* Journal of the American Chemical Society, 2005. **127**(35): p. 12387-12391.

88. Remsen, L.G., et al., *MR of carcinoma-specific monoclonal antibody conjugated to monocrystalline iron oxide nanoparticles: The potential for noninvasive diagnosis.* American Journal of Neuroradiology, 1996. **17**(3): p. 411-418.

89. Berry, C.C., et al., *The influence of transferrin stabilised magnetic nanoparticles on human dermal fibroblasts in culture.* International Journal of Pharmaceutics, 2004. **269**(1): p. 211-225.

90. Moore, A., et al., *Human transferrin receptor gene as a marker gene for MR imaging.* Radiology, 2001. **221**(1): p. 244-250.

91. Qian, Z.M., et al., *Targeted drug delivery via the transferrin receptor-mediated endocytosis pathway.* Pharmacological Reviews, 2002. **54**(4): p. 561-587.

92. Kresse, M., et al., *Targeting of ultrasmall superparamagnetic iron oxide (USPIO) particles to tumor cells in vivo by using transferrin receptor pathways.* Magnetic Resonance in Medicine, 1998. **40**(2): p. 236-242.

93. Wunderbaldinger, P., L. Josephson, and R. Weissleder, *Tat peptide directs enhanced clearance and hepatic permeability of magnetic nanoparticles.* Bioconjugate Chemistry, 2002. **13**(2): p. 264-268.

94. Farokhzad, O.C., et al., *Nanopartide-aptamer bioconjugates: A new approach for targeting prostate cancer cells.* Cancer Research, 2004. **64**(21): p. 7668-7672.

95. Herr, J.K., et al., *Aptamer-conjugated nanoparticles for selective collection and detection of cancer cells.* Analytical Chemistry, 2006. **78**(9): p. 2918-2924.

96. Yigit, M.V., et al., *Smart "Turn-on" magnetic resonance contrast agents based on aptamer-functionalized superparamagnetic iron oxide nanoparticles.* Chembiochem, 2007. **8**(14): p. 1675-1678.

97. Weissleder, R., et al., *Cell-specific targeting of nanoparticles by multivalent attachment of small molecules.* Nature Biotechnology, 2005. **23**(11): p. 1418-1423.

98. Campbell, I.G., et al., *Folate-Binding Protein Is a Marker for Ovarian-Cancer.* Cancer Research, 1991. **51**(19): p. 5329-5338.

99. Ross, J.F., P.K. Chaudhuri, and M. Ratnam, *Differential Regulation of Folate Receptor Isoforms in Normal and Malignant-Tissues in-Vivo and in Established Cell-Lines - Physiological and Clinical Implications.* Cancer, 1994. **73**(9): p. 2432-2443.

100. Weitman, S.D., et al., *Distribution of the Folate Receptor Gp38 in Normal and Malignant-Cell Lines and Tissues.* Cancer Research, 1992. **52**(12): p. 3396-3401.

101. Lu, Y.J. and P.S. Low, *Folate-mediated delivery of macromolecular anticancer therapeutic agents.* Advanced Drug Delivery Reviews, 2002. **54**(5): p. 675-693.

102. Shi, X.Y., et al., *Dendrimer-functionalized shell-crosslinked iron oxide nanoparticles for in-vivo magnetic resonance imaging of tumors.* Advanced Materials, 2008. **20**(9): p. 1671-+.

103. Sun, C., R. Sze, and M.Q. Zhang, *Folic acid-PEG conjugated superparamagnetic nanoparticles for targeted cellular uptake and detection by MRI.* Journal of Biomedical Materials Research Part A, 2006. **78A**(3): p. 550-557.

104. Zhang, Y., et al., *Self-assembled coatings on individual monodisperse magnetite nanoparticles for efficient intracellular uptake.* Biomedical Microdevices, 2004. **6**(1): p. 33-40.

105. Hong, S., et al., *The binding avidity of a nanoparticle-based multivalent targeted drug delivery platform.* Chemistry & Biology, 2007. **14**(1): p. 107-115.

106. Shukla, R., et al., *Tumor angiogenic vasculature targeting with PAMAM dendrimer-RGD conjugates.* Chemical Communications, 2005(46): p. 5739-5741.

107. Brittenham, G.M., et al., *Magnetic-Susceptibility Measurement of Human Iron Stores.* New England Journal of Medicine, 1982. **307**(27): p. 1671-1675.

108. Cohen, D., *Ferromagnetic Contamination in Lungs and Other Organs of Human Body.* Science, 1973. **180**(4087): p. 745-748.

109. Tanaka, S., et al., *Lymph-node detection system using a high T-c SQUID and ultra-small particles.* Ieice Transactions on Electronics, 2002. **E85c**(3): p. 687-690.

110. Chemla, Y.R., et al., *Ultrasensitive magnetic biosensor for homogeneous immunoassay.* Proceedings of the National Academy of Sciences of the United States of America, 2000. **97**(26): p. 14268-14272.

111. Enpuku, K., et al., *High Tc SQUID system and magnetic marker for biological immunoassays.* Ieee Transactions on Applied Superconductivity, 2003. **13**(2): p. 371-376.

112. Weitschies, W., et al., *Determination of relaxing or remanent nanoparticle magnetization provides a novel binding-specific technique for the evaluation of immunoassays.* Pharm. Pharmacol. Lett, 1997. **7**: p. 1-7.

113. Enpuku, K., et al., *Detection of magnetic nanoparticles with superconducting quantum interference device (SQUID) magnetometer and application to immunoassays.* Japanese Journal of Applied Physics Part 2-Letters, 1999. **38**(10A): p. L1102-L1105.

114. Enpuku, K., et al., *Application of high T-c SQUID magnetometer to biological immunoassays.* Ieee Transactions on Applied Superconductivity, 2001. **11**(1): p. 661-664.

115. Tanaka, S., et al., *Application of high TcSQUID magnetometer for sentinel-lymph node biopsy.* Ieee Transactions on Applied Superconductivity, 2001. **11**(1): p. 665-668.

116. Tanaka, S., et al., *Detection of magnetic nanoparticles in lymph nodes of rat by high T-C SQUID.* Ieee Transactions on Applied Superconductivity, 2003. **13**(2): p. 377-380.

117. Yang, T.Q., et al., *Detection of magnetic nanoparticles with ac susceptibility measurement.* Physica C-Superconductivity and Its Applications, 2004. **412-14**: p. 1496-1500.

118. Enpuku, K., et al., *Magnetic immunoassays utilizing magnetic markers and a high-T-C SQUID.* Ieee Transactions on Applied Superconductivity, 2005. **15**(2): p. 660-663.

119. Enpuku, K., et al., *Application of HTS SQUIDs to biological immunoassays.* Physica C-Superconductivity and Its Applications, 2004. **412-14**: p. 1473-1479.

120. Kawagishi, K., et al., *Detection of fine magnetic particles coated on a thread using an HTS-SQUID.* Physica C-Superconductivity and Its Applications, 2004. **412-14**: p. 1491-1495.

121. Kotitz, R., et al., *SQUID based remanence measurements for immunoassays.* Ieee Transactions on Applied Superconductivity, 1997. **7**(2): p. 3678-3681.

122. Tsukamoto, A., et al., *Development of multisample biological immunoassay system using HTS SQUID and magnetic nanoparticles.* Ieee Transactions on Applied Superconductivity, 2005. **15**(2): p. 656-659.

123. Chemla, Y.R., et al., *Ultrasensitive magnetic biosensor for homogeneous immunoassay.* Proc. Natl. Acad. Sci. U. S. A., 2000. **97**(26): p. 14268-14272.

124. Grossman, H.L., et al., *Detection of bacteria in suspension by using a superconducting quantum interference device.* Proc. Natl. Acad. Sci. U. S. A., 2004. **101**(1): p. 129-134.

125. Haller, A., et al., *Low T-c SQUID measurement system for magnetic relaxation immunoassays in unshielded environment.* IEEE Trans. Appl. Supercond., 2001. **11**(1): p. 1371-1374.

126. Lange, J., et al., *Magnetorelaxometry - a new binding specific detection method based on magnetic nanoparticles.* J. Magn. Magn. Mater., 2002. **252**(1-3): p. 381-383.

127. Lee, S., et al., *Magnetic gradiometer based on a high-transition temperature superconducting quantum interference device for improved sensitivity of a biosensor.* Appl. Phys. Lett., 2002. **81**(16): p. 3094-3096.

128. Williamson, S.J. and L. Kaufman, *Biomagnetism Topical Review.* Journal of Magnetism and Magnetic Materials, 1981. **22**(2): p. 129-201.

129. Johnsen, S. and K.J. Lohmann, *Magnetoreception in animals.* Physics Today, 2008. **61**(3): p. 29-35.

130. Cayless, A.T., et al., *High-Sensitivity Measurements of Neel Relaxation in Fine Particle Ferromagnetic Systems.* Journal of Magnetism and Magnetic Materials, 1983. **30**(3): p. 303-311.

131. Chantrell, R.W., S.R. Hoon, and B.K. Tanner, *Time-Dependent Magnetization in Fine-Particle Ferromagnetic Systems.* Journal of Magnetism and Magnetic Materials, 1983. **38**(2): p. 133-141.

132. Romanus, E., et al., *Determination of energy barrier distributions of magnetic nanoparticles by temperature dependent magnetorelaxometry.* Nanotechnology, 2003. **14**(12): p. 1251-1254.

133. Romanus, E., et al., *Energy barrier distributions of maghemite nanoparticles.* Nanotechnology, 2007. **18**(11): p. -.

134. Moore, A., et al., *Tumoral distribution of long-circulating dextran-coated iron oxide nanoparticles in a rodent model.* Radiology, 2000. **214**(2): p. 568-574.

135. Lewin, M., et al., *Tat peptide-derivatized magnetic nanoparticles allow in vivo tracking and recovery of progenitor cells.* Nature Biotechnology, 2000. **18**(4): p. 410-414.

CHAPTER 2

Remanence Measurement-Based SQUID System with In-depth Resolution

2.1 Introduction

Over the past decade, *in vivo* imaging techniques using magnetic nanoparticles (NPs) as contrast agents for disease diagnosis, especially cancers, have undergone rapid development.[1, 2] The earlier the tissue lesion is detected, the better the chance that it can be treated. The use of superconducting quantum interference devices (SQUIDs), the most sensitive magnetic sensors to date [3], stands out as a promising technique for imaging of targeted magnetic NPs.

SQUID imaging, due to is non-invasive nature, has been applied to: tracking the naturally stored magnetic particles in human organs [4, 5], detecting targeted magnetic NPs in the sentinel lymph node [6] and biological immunoassays.[7-9] This strategy is becoming more promising as the quality of magnetic NPs has been greatly improved with higher bio-compatibility achieved and multiple functional ligands conjugated to the surface.[10, 11] The detection methods using SQUID are closely related to the size-dependent magnetic properties of magnetic NPs and three such methods have been developed. They are susceptibility [12-16], remanence [8, 17-20] and magnetorelaxometry.[7, 21-24]

The advantage of the remanence measurement is the highest sensitivity among the three techniques. The high sensitivity results from the absence of magnetizing field during measurement and no NP size dependency, as long as the particles are large enough to exhibit remanence. The iron oxide NPs used for remanence detection typically have an average diameter of 25nm.[18-20, 25] For this size, Brownian rotation occurs on the micro-second scale, which is not observable whereas Néel relaxation can take many hours. Contrast arises when the NPs are bound to the target so that Brownian rotation is quenched. Remanence measurement typically requires movement of the sample to generate a magnetic signal change for the SQUID to detect. Instead of using lateral movement as previously reported [18, 20], our system utilizes vertical oscillation which frees the horizontal plane for translational scanning. A 1-D scanning stage based on this remanence method is described in this chapter with studies on reconstructing the NPs' distribution from the image. This method complements existing SQUID measurement techniques and excels due to its high sensitivity and portability.

2.2 Methods

2.2.1 Setup of the SQUID Imaging System

The SQUID used in this study, as well as the rest of the dissertation, was a 2nd order gradiometer system, Model 601 dc LTS, provided by the Tristan Technology Inc. The manufactured device is composed of a cryogenic system, LTS dc SQUID sensor and control electronics. The cryogenic system includes a liquid helium dewar (Model BMD-9), single channel probe (Model BMP-9), cryogenic cable and second order gradiometer detection coil. The control electronics system consists of liquid helium level sensor, flux-

locked loop (Model iFL-301-L), fiber-optic connecting cable and LTS multi-channel SQUID control unit (Model iMC-303). The SQUID controller has various gains (×1 to ×500) available, which means the sensitivity of the output voltage to the detected magnetic field can be varied over a wide range. The liquid helium level meter was purchased from the American Magnetics, Inc. (Model 110A, analog) and assembled with the SQUID system in the lab.

Based on this device, a remanence measurement-based SQUID imaging system was developed, a photograph of which is shown in Figure 2.1. The system was mostly made of wood and assembled with glue and copper screws to avoid the magnetic noise

Figure 2.1 Picture of the remanence measurement-base SQUID imaging system with 1D scanning ability.

from iron pieces being detected by the SQUID sensor. The maximum lateral translation is about 20 cm. Due to the high sensitivity of SQUID, magnetic impurities in the oscillation stage can influence the signal significantly. A wide range of materials were tested including aluminum, various kinds of plastic, wood, glass, foam pad, etc. Glass and foam pad showed minimum signals and foam pad was chosen because it's easier to work with.

Figure 2.2 shows a schematic diagram of the experimental setup. To generate a magnetic flux change in the SQUID pick-up coils, the sample was vertically oscillated. The oscillation was driven by a stepping motor, which was controlled by an EA-40 Precision Sine Drive. The rotation rate could be adjusted by the front panel from 0.2 to 2 Hz with a resolution of 0.01 Hz. In order to drive the translation motion, a more powerful stepping motor was used, which has single step size of 7.5°, translation to a 2.5 mm lateral motion. This motor was controlled by a SC1125-3-MS stepper motor controller (from Salem Controls, Inc.), which was connected to the parallel port of a computer. The laser came from a laser pointer with the power smaller than 5 mW and wavelength within the range of 630~680 nm. A Thorlabs' DET110 high-speed silicon detector was used to detect the laser beam and convert the optical signal into an electronic signal. The photo detector had spectral range from 350 to 1100 nm and response time around 20 ns. The output of the detector was connected to a resistor to induce a voltage, which was sent to a lock-in amplifier (Ithaco, Model 3961B) as the reference signal. The lock-in amplifier features a frequency range of 0.5 to 200,000 Hz and the maximum sensitivity is 100 nVrms. The use of lock-in amplifier enabled noise reduction as well as signal amplification.

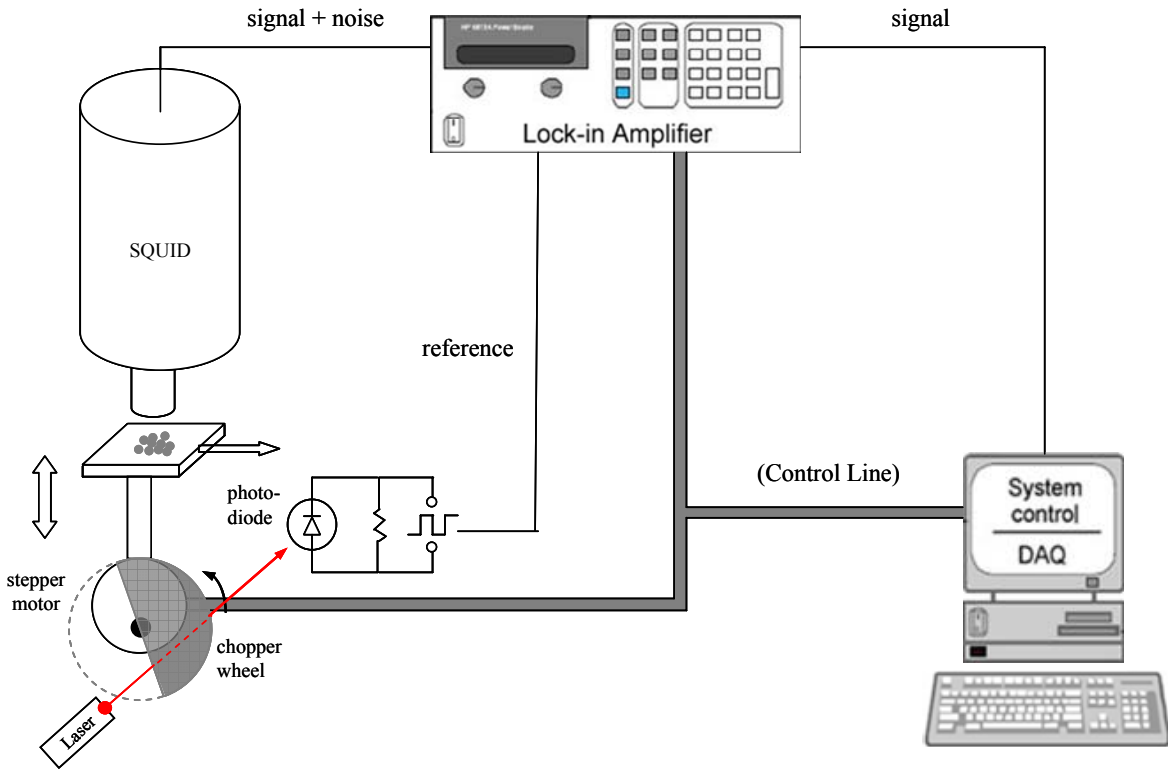

Figure 2.2 Schematic representation of the remanence experimental set-up that uses vertical oscillation to generate magnetic field change and uses horizontal direction for translation.

The oscillation generating stepping motor rotated off-center, driving the sample containing magnetic NPs to move up and down under the SQUID sensor at a chosen frequency (*f*). This motor had a semicircular chopper attached to its axle with the laser generator and the photo detector located on different sides of the chopper. The laser beam and the photo detector were aligned so that the detector generated on/off states when the chopper rotated. Hence a square wave of frequency (*f*) was formed and sent to the lock-in amplifier as the reference signal. The lock-in amplifier filtered out noises at frequencies other than *f*. Measurements were able to be performed without the use of an electromagnetically shielded room due to the noise rejection of the phase sensitive detection.

In a typical experiment, a vertical oscillation of the sample at 2 Hz with amplitude of 0.3 cm was used. The translational stepping motor moved the whole stage horizontally in one dimension, with a typical step size of 0.25 cm. The lock-in amplifier applies a low-pass filter with a 3 Hz cutoff to the signal generated by the SQUID to remove the interference from the power cables (60 Hz and its harmonics) and random events. The time constant was set to 3 s to ensure sufficient time for the low-pass filter to achieve equilibrium. During movement of the translation stage from one location to another, the data acquisition was suspended for about 20 s and resumed when the lock-in amplifier reached equilibrium. The system was fully controlled by a computer through a LabVIEW interface. From the panel, the measurement numbers at each position, the time interval between two positions and the direction and size of the translation can be varied. The display window on the bottom-left corner was designed to observe the data taken at the current position and discard the ones that were interfered with unexpected incidents due to the unshielded condition.

2.2.2 Dry Nanoparticle Preparation

γ-Fe_2O_3 (99+%, Alfa Aesar, USA) NPs with an average diameter of 25 ± 19 nm were used (Figure 2.3). NPs were suspended in deionized water and vortexed to achieve good dispersion. Serial dilutions were prepared and each was loaded onto a piece of 0.5 × 0.5 cm^2 filter paper. The loaded filter paper was magnetized in the vertical direction under a 1-T magnetic field for approximately 30 s by using a permanent magnet. The residual magnetization was measured by SQUID. The samples prepared in this way were used for quantitative calibration.

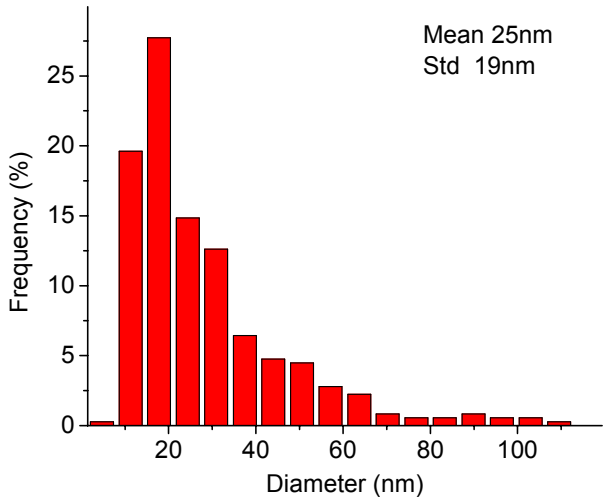

Figure 2.3 Size distribution histogram of the γ-Fe_2O_3 NPs by measuring 300 NPs from TEM images.

The spatial resolution study used samples prepared in the same way. Filter paper with different areas, 1×1 cm^2 and 0.2×0.2 cm^2 were scanned instead to test the influence of sample size. The 1D scanning stage translated the samples at a step size of 0.25 cm and at each position the signal was averaged over 15 measurements before moving on.

2.2.3 Tissue Mimicking Phantom Measurements

To represent tissue imaging conditions, cylindrical tissue samples (hotdogs) were used as a phantom. A small volume (5 μL or less) of NP fluid was injected by a microsyringe into selected sites. A phantom segment (3 cm long) was first magnetized and pre-scanned along its cylindrical axis before any injection of NPs. After NPs were injected, it was magnetized and scanned again and the pre-scan was subtracted to acquire the net signal. The injection sites were selected at lateral separations of 1, 1.5, and 2 cm and at depths of 0.5 and 1 cm below the upper surface.

2.2.4 Theoretical Model

A theoretical model of the depth dependence of the remanence measurement has been developed. The *x*-*z* coordinate system and the angle θ are defined as shown in Figure 2.4, changing from 0 to π representing a scan of sample along the x-axis. As a 2nd order gradiometer, the SQUID detector has three sets of pick-up coils, with diameters of 1 cm and 4 turns in each set and negligible thickness. Separations between adjacent sets are 5 cm. Distance between the Dewar's inside bottom and the middle of the closest coil is 0.2 cm and *D* denotes the Dewar's tail separation (0.9 cm). During the sample's oscillation, *a*, *b* are the nearest and farthest distances, respectively between the sample and the Dewar's bottom. Two assumptions were made:

1) The ensemble of magnetized NPs is regarded as a single magnetic moment;
2) The magnetic flux threading each coil is approximately equal to the product of the central field strength and the coil area.

The magnetic field produced by a magnetic moment can be expressed as:

$$\vec{B}(\vec{x}) = \frac{\mu_0}{4\pi}\left[\frac{3\vec{n}(\vec{n}\cdot\vec{m})-\vec{m}}{|\vec{x}|^3}\right] \tag{2-1}$$

In our case, the expression can be reduced to the z-component:

$$B_z = \frac{\mu_0 m}{4\pi h^3}\left(3\sin^2\theta - 1\right)\sin^3\theta \tag{2-2}$$

By multiplying the area and number of turns of each set of pick-up coils to this field (B_z) and considering the polarity of each set, the net flux can be calculated. The sample oscillation is simulated by changing the parameter *h* (Figure 2.4). The flux achieves maximum and minimum values during the change. Half of the maximum and minimum difference is recorded as the signal amplitude. This amplitude is numerically

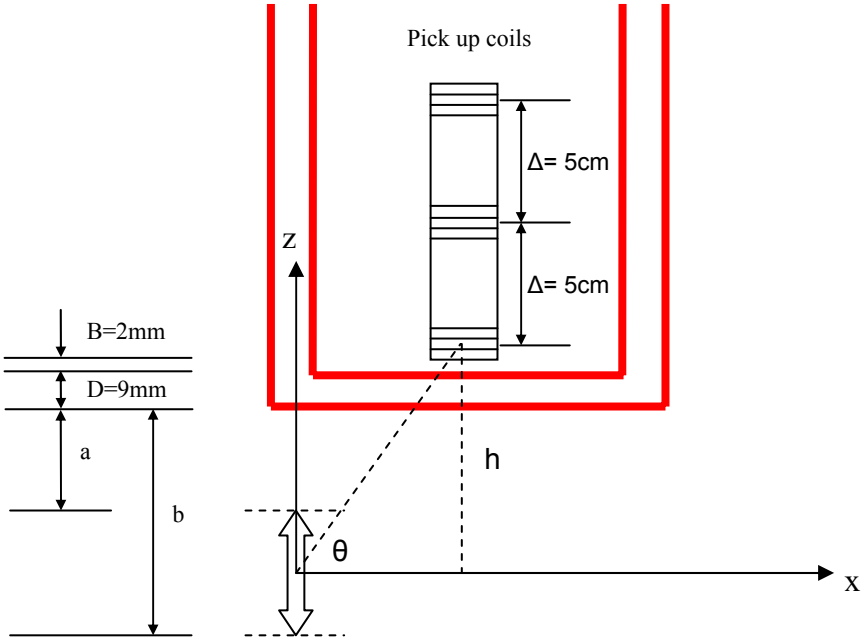

Figure 2.4 Schematic illustration of the theoretical model on the remanence measurement SQUID system.

calculated and compared with the SQUID measurement. Equation (2) has zeros at θ = 0.62 (<π/2) and 2.53 (>π/2) located on either side of the central peak, indicating that the signal minima will be detected around these two points. Note that the magnetic flux changes sign as scanning of NPs passes through the two minima, which means a π-phase shift in the lock-in amplifier phase reading.

2.3 Results and Discussion

2.3.1 Calibration and Sensitivity

A series of Fe_2O_3 samples with various iron masses ranging from 60 ng to 24 μg were measured for calibration. A linear relationship (with slope = 0.95 and coefficient of regression R^2 = 0.98) between the mass of NPs and the detected magnetic field was observed (Figure 2.5). During the measurement, a constant background field of about (3

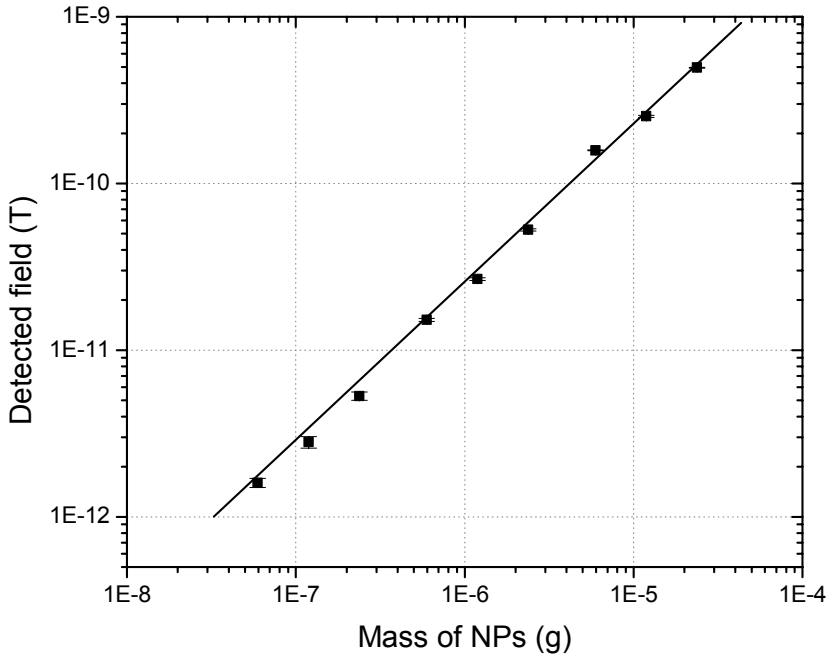

Figure 2.5 A calibration curve shows a linear relationship between the detected magnetic field and the mass of Fe_2O_3 NPs. All data points were obtained by averaging over 60 measurements with background field of 3×10^{-13} T subtracted.

$\pm$ 0.5) $\times$ 10^{-13} T was present. Therefore with a signal-to-noise ratio of 1, the minimum detectable limit was 10 ng of particles with the sample at a distance of 1.7 cm from the SQUID lowest coil. The distance was calculated by adding *B* and *D* (see section 2.2.4 and Figure 2.4), the distance from the bottom of the Dewar to the equilibrium position of the oscillation. This sensitivity is similar to, or slightly better, than previously reported remanence methods.[18, 20, 26]

It is important to recognize that not all the NPs are observable in the remanence measurement. Instead, only particles with relaxation time longer than the measurement time scale can be detected. In our experimental setup, the integration time of the lock-in amplifier is 3 s, which means that NPs with relaxation time shorter than 3 s make no

contribution to the signal. In the application of the system to *in vivo* imaging, for the NPs bound to the target, they are immobilized and the magnetic moments decay through the Néel mechanism only, which is predicted by:

$$\tau_N = \tau_0 \exp(KV / k_B T) \tag{2-3}$$

where $\tau_0 = 10^{-9}$ s and K is the magnetic anisotropy constant. Assuming the bulk γ-Fe_2O_3 K value (2.5×10^4 J/m^3) [21], the relaxation time of NPs with d = 25 nm is 3×10^{12} s, meaning these immobilized NPs provide measurable signals. For other particles that are not bound to any tissue, the Brownian mechanism dominates the relaxation process, and has a time constant described by:

$$\tau_B = 3\eta V_H / k_B T \tag{2-4}$$

where, η is the medium viscosity and V_H is the hydrodynamic volume. Taking the viscosity of water ($\eta = 10^{-3}$ kg/m·s), the NPs need to agglomerate to 2 μm in diameter (equivalently a cluster of 512,000 NPs) to achieve relaxation time around 3 s. Particles of this size are too large to be allowed in the body, and will be filtered out. To avoid such agglomeration from occurring, an appropriate surfactant coating for better bio-compatibility needs to be applied to the NPs reducing the particle interaction, as has been achieved by our group.[10]

As long as the lock-in amplifier's range did not change, the fluctuation of the detected signal was always about 0.5×10^{-13} T, independent of the sample's mass. For higher fields arising from more particles, the SQUID signal exceeds the lock-in amplifier's current range and a higher range must be used. Though this higher range of amplification results in larger standard deviations, the relative error (ratio of the standard deviation to the measuring range) remained constant. In all measurements, the SQUID

was used with a gain (×10) corresponding to a conversion constant of 16.2 nT/V. Although higher gains were available, they did not enhance the sensitivity because both signal and noise were increased by the same amount.

2.3.2 Lateral Spatial Resolution of the Scanning System

Two Fe_2O_3 NP samples with the same mass (300 ng in each) and area (~1 × 1 cm^2) were positioned with various separations and scanned under the SQUID system. The oscillation amplitude (0.3 cm) and the distance from the SQUID coil (1.7 cm) remained consistent. Figure 2.6 (a) shows a typical profile over only one Fe_2O_3 NP sample. A large center peak with two side minima was observed. This agrees with the prediction of the theoretical model. The reason for the two minima was explained in section 2.2.4, and is due to the near zero magnetic flux threading the lowest pick-up coils. The half-peak width is approximately 2 cm, implying that the minimal identifiable distance between two samples should be about 2 cm. This prediction is confirmed by the SQUID measurements on samples with two spots at various separation distances, 1.5 - 2.5 cm from center to center. These samples were scanned along the line connecting their centers. The signals generated show that individual spots can only be identified when the center-to-center separation is larger than 2 cm, i.e. the edge-to-edge separation equals 1 cm (Figure 2.6 b-d).

To further investigate the sample size dependence of the spatial resolution, smaller spots with area roughly 0.2 × 0.2 cm^2 were tested, as illustrated by Figure 2.7. The results show that the minimal resolvable center-to-center distance is 1.25 cm. However, it actually does not suggest an improvement of the resolving ability of SQUID, because the edge-to-edge separation is 1.05 cm after subtracting the sample size. The

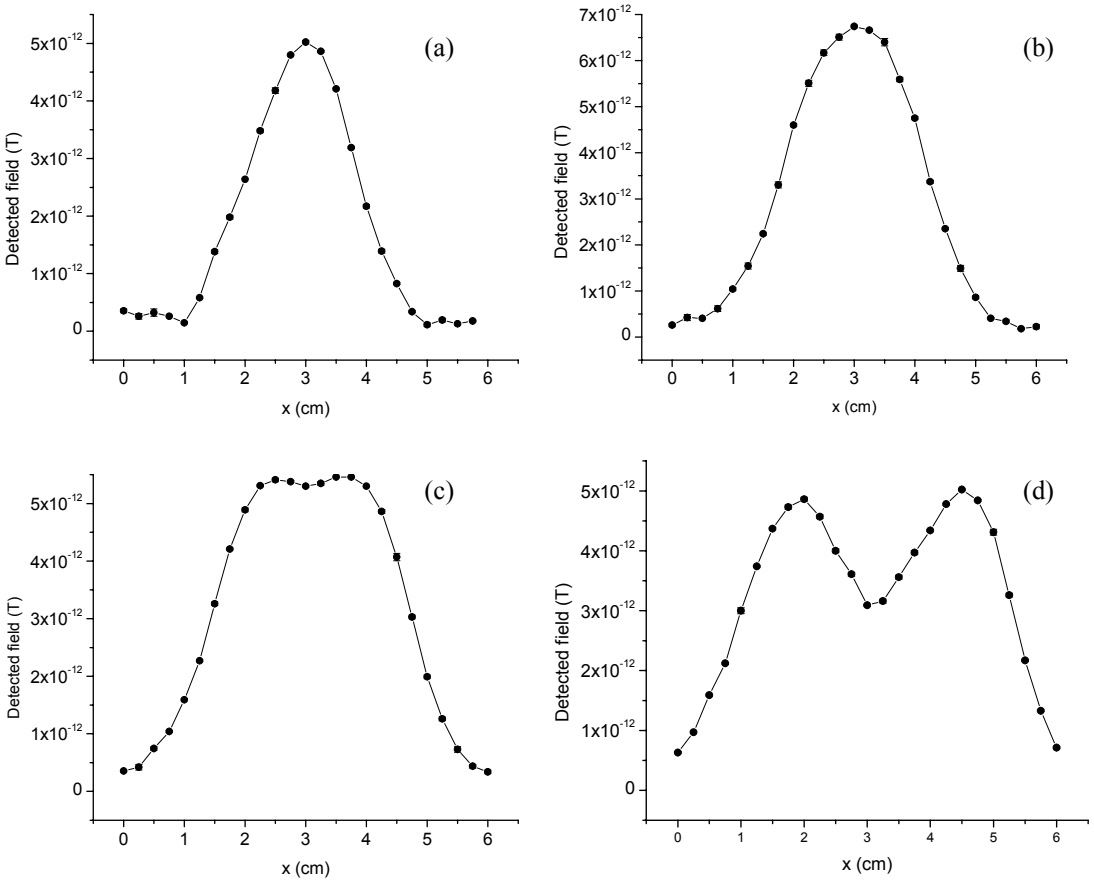

Figure 2.6 Lateral spatial resolution of 300 ng Fe_2O_3 NP spots with 1×1 cm^2 sample area. (a) A typical scanning profile of one spot. Two similar sample spots (as in (a)) were scanned in-line at different separations: (b) 1.5 cm, (c) 2 cm (d) 2.5 cm.

minimum separation distance obtained from these results coincides with the pick-up coil diameter of the SQUID which is also 1 cm, suggesting that the spatial resolution limit is physically restricted by the pick-up coil size.

2.3.3 Correlation of Peak Width and NP Position

In the spatial resolution study, when a single sample spot was scanned, a central signal peak with two subsidiary minima was generated. The peak width, defined as the separation of the two minima, was found to be dependent on the vertical distance between the sample and the SQUID pick-up coils. In order to have significant signal at a

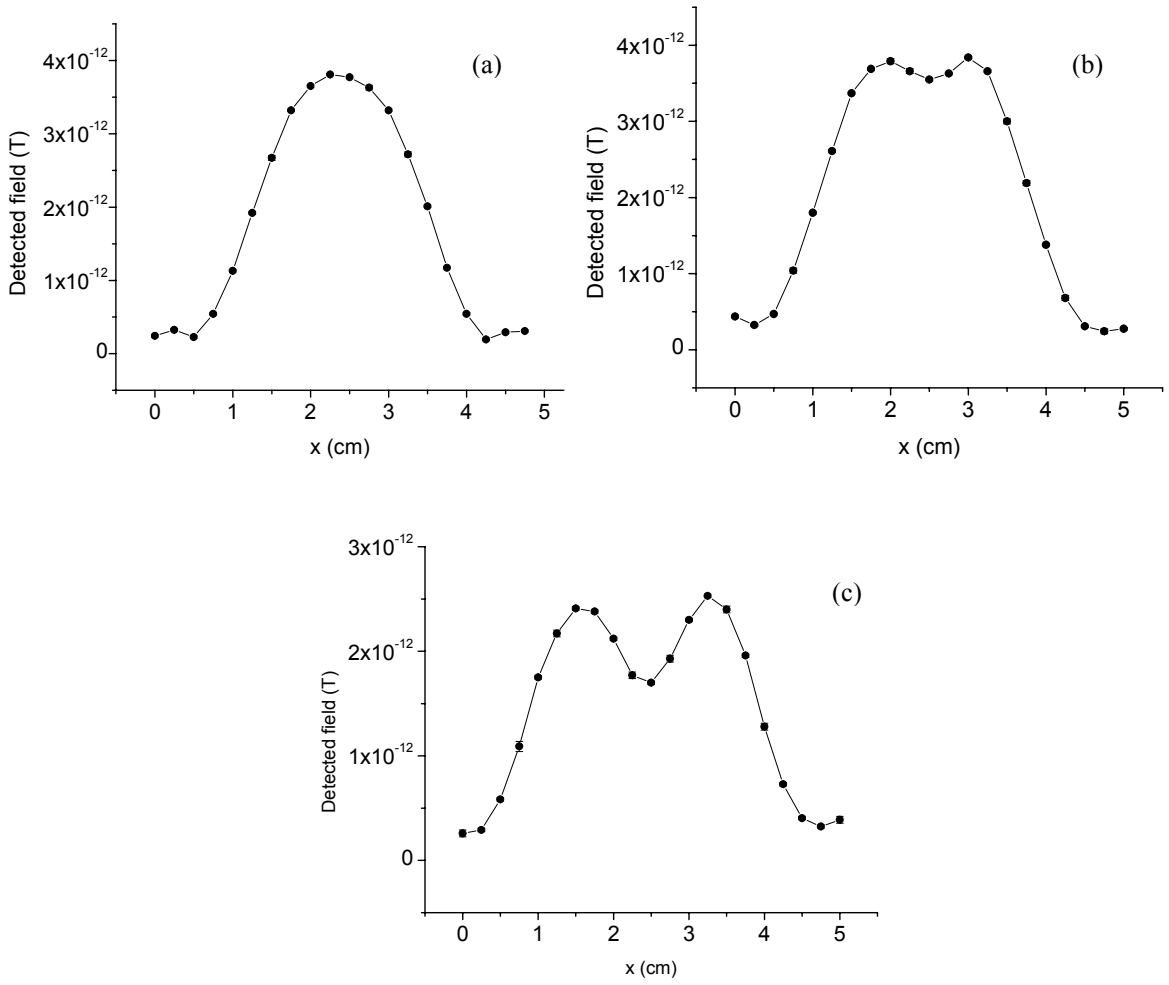

Figure 2.7 Lateral spatial resolution of 150 ng Fe_2O_3 NP spots with 0.2×0.2 cm^2 sample area. Two spots were scanned in-line at different separations: (a) 1 cm, (b) 1.25 cm (c) 1.5 cm.

greater distance, 11.9 μg Fe_2O_3 NPs was measured with its oscillation center to the closest pick-up coil at 1.7, 2.1 and 2.7cm while the oscillation amplitude was kept constant (0.3 cm). The peak widths were approximately 2.75, 3.25 and 4 cm respectively. The scanned curves are shown in Figure 2.8 (a), where larger distance results in wider central peak.

To compare the experimental data with the theoretical predictions, the x-position was converted into the angle θ as defined in section 3 and re-plotted in Figure 2.8 (b)

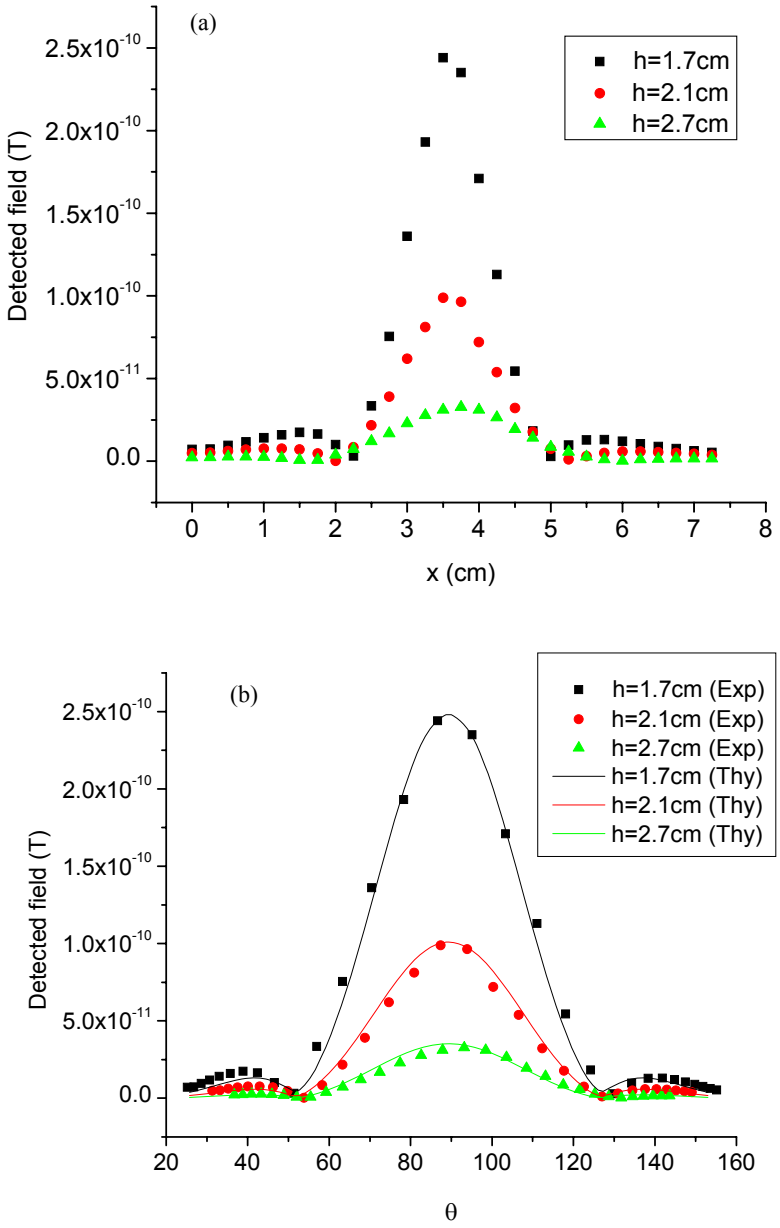

Figure 2.8 Relationship between the scanned peak width and NPs' vertical position. (a) Experimental data when the sample to pick-up coil distances are 1.7, 2.1 and 2.7cm (b) theoretical fittings (solid lines) are consistent with experimental data (dots).

(represented by dots). Simulations were performed at these vertical sample-to-coil distances (h = 1.7, 2.1 and 2.7 cm) using the parameters in the system setup. Due to the unknown magnetic remnant moment of the NPs, a common factor was used to normalize

all three simulated curves to agree with the experimental data. The fitting results are shown in Figure 2.8 (b) by solid lines. Based on this calculation and the mass of the NPs used, the remnant mass magnetization of the Fe_2O_3 NPs was estimated to be 1.1 emu/g. As can be seen from the plot, the angle spanned by the minima is almost constant, which agrees with the model because of the vanishing B_z field. Further computation with larger ranges of vertical sample-to-coil distance (h = 1.3 to 3 cm) shows that the angle changes within the range of 52.2˚ to 52.8˚, with a minimum at h = 1.85 cm. This near-constant span angle dictates that the wider peak in terms of distance along the scan direction implies the sample is farther away from the detector.

This remanence estimation will contain uncertainty due to the model's assumptions. Specifically, the finite sample area, the non-uniformity of field threading the pick-up coils and the lock-in amplifier's gain will all contribute to this uncertainty. However, due to the constancy of the normalization factor, the measurements can be calibrated with standard samples. Since the NPs' position relates to the scanned peak maximum and width, the determination of the particles' position and mass will be unique.

2.3.4 Reconstruction of NPs' Distribution from Images

To resolve NPs not only in the lateral direction but also at different depths, hotdog phantoms were used as matrices and injected with NPs at two points. In the first study, a 5 μL injection containing 10 μg NPs was injected at 0.5 cm below the upper surface with separations at 1, 1.5 and 2 cm. During the SQUID measurement, the distance from the lowest coils to the upper surface was kept the same as before (1.7 cm). This distance was subtracted from the z-distance parameter determined by the model to calculate the actual depth of the NPs in the sample. Pre-scan curves were subtracted from the scan results and

net signals are plotted in Figure 2.9. To fit the experimental data, the model needs to incorporate two NP sources simultaneously. One cannot simply add individual curves together because signals from the two sources are not always in phase. Instead, the Levenberg-Marquardt algorithm was applied until the best fitting was achieved. In Figure 2.9, the solid lines are the best fittings after adding both sources in phase and the dashed lines represent signals from each sources in the absence of the other. In the regions where their central peaks overlap and shoulder peaks overlap, they are in phase and reinforce each other.

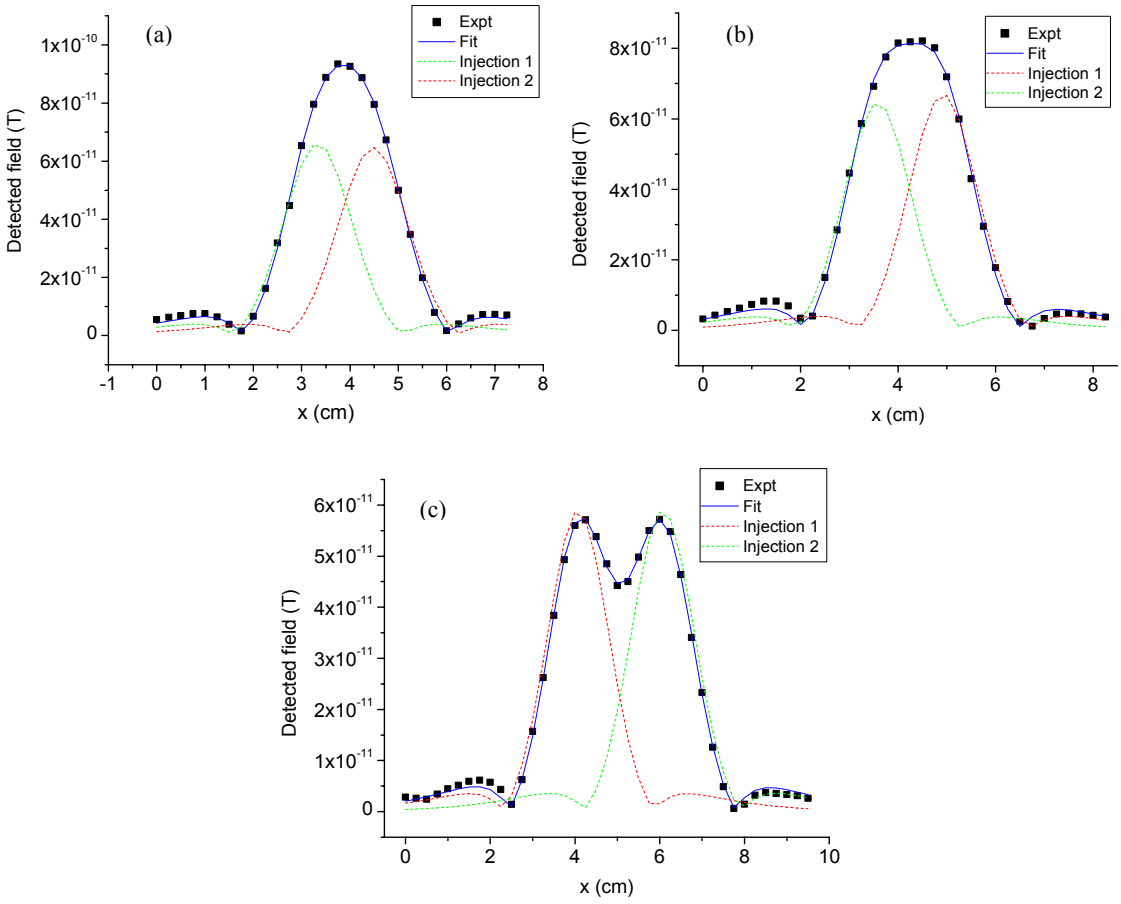

Figure 2.9 Phantom study of same amount of Fe_2O_3 NP injection (10 μg) at different lateral separations: (a) 1 cm (b) 1.5 cm and (c) 2 cm below the upper surface by 0.5 cm.

The fitting results are summarized in Table 2.1. When the lateral separation between the injections is larger than the spatial resolution limit of the SQUID scanning system (case b and c), one can tell from the resultant curves (Figure 2.9 b and c) that there are more than one NP injections in the phantoms. To fit the curves, it is obvious to include two remanence sources in the model and the results match the experimental controls. As the separation decreases down to 1 cm, within the resolution limit, only a single peak is observed. Two scenarios need to be evaluated: one injection and two injections to figure out which case is more reasonable. If one remanence source is considered in the model, the fitting residuals are five times higher than assuming two sources, suggesting the two-injection assumption is closer to the real case. Moreover, the fitting results with one injection turn out to be 1.32 cm in depth and 47.31 μg in amount. Since we know the total injected amount of NPs are 20 μg (Table 2.1), which is much less than 47.31 μg, the possibility of one injection can be ruled out.

Since the peaks in the SQUID image can be affected by both the mass of the NPs and the vertical distance to the pick-up coils, similar scanning peaks may be observed due to fewer NPs that are positioned nearer the detector, as compared with more NPs that are

Table 2.1 Phantom study of same amount of NP injection (10 μg) at different lateral separations.

		Experimental controls			Fitting results		
		lateral separation (cm)	depth in phantom (cm)	amount of NPs (μg)	lateral separation (cm)	depth in phantom (cm)	amount of NPs (μg)
Case (a)	Injection 1	1	0.5	10	3.33	0.57	9.76
	Injection 2		0.5	10	4.45	0.61	10.33
Case (b)	Injection 1	1.5	0.5	10	3.55	0.52	8.67
	Injection 2		0.5	10	4.93	0.57	9.85
Case (c)	Injection 1	2	0.5	10	4.08	0.59	9.17
	Injection 2		0.5	10	6.07	0.64	10.69

farther away. Our image fitting algorithm is able to discriminate between these two cases. To demonstrate this, one phantom was injected at two spots with 10 μg and 5 μg Fe_2O_3 NPs at a depth of 0.5 cm below the upper surface. A second phantom was prepared by injecting two locations both with 10 μg, one injection was at a depth of 0.5 cm and the other at a depth of 1cm. The horizontal separation of the injections in both cases was 1.5 cm. The data dots in Figure 2.10 display similar scanning patterns acquired from these two phantoms both have a smaller peak on the right side of the major one. One of them is generated by the phantom with spots having different NP masses (Figure 2.10a), while the other one is due to the phantom that had the NPs at different depths (Figure 2.10b). By comparing these two curves, we can differentiate between them. On the right part of the major peak (the lower portion), Figure 2.10b has a larger shoulder than Figure 2.10a, implying a wider peak generated by the second injection spot in (b). Due to the near-constant span angle, this wider peak means the second injection is deeper than (a). The fitting parameters supported the observation and quantitatively determined the difference

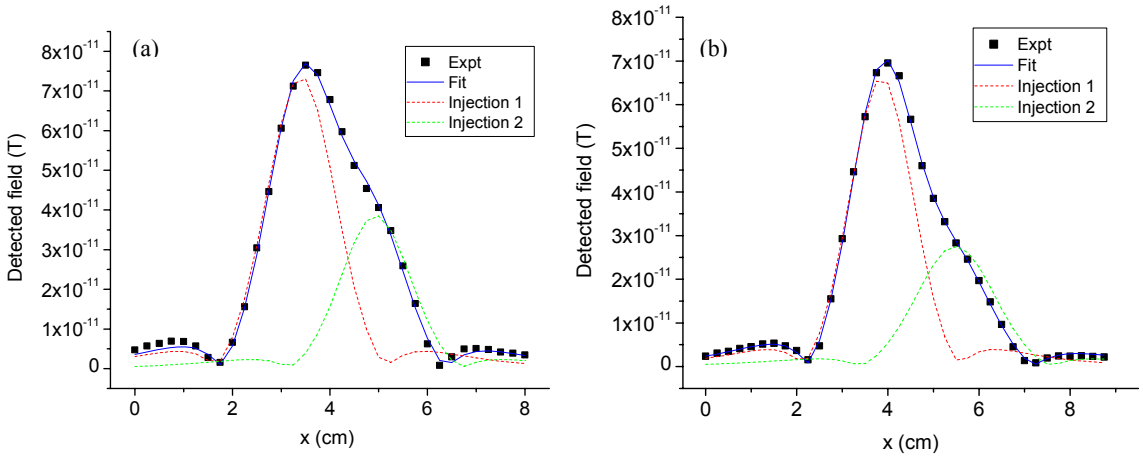

Figure 2.10 Phantom study of different amounts of Fe_2O_3 NP injection at the same lateral separation (1.5 cm) but different depths. (a) 10 μg and 5 μg both at 0.5 cm below the upper surface (b) 10 μg at 0.5 cm and 1 cm below the upper surface respectively.

of the two cases: the NP injections on the right side are 5.92 μg at 0.58 cm deep and 8.82 μg at 1.03 cm respectively (Table 2.2).

Table 2.2 Phantom study of different amounts of NP injection at different depths.

		Experimental controls			Fitting results		
		lateral separation (cm)	depth in phantom (cm)	amount of NPs (μg)	lateral separation (cm)	depth in phantom (cm)	amount of NPs (μg)
Case (a)	Injection 1	1.5	0.5	10	3.40	0.56	10.62
	Injection 2		0.5	5	4.94	0.58	5.92
Case (b)	Injection 1	1.5	0.5	10	3.88	0.52	8.86
	Injection 2		1.0	10	5.48	1.03	8.82

These experiments to reconstruct the NPs' distribution in phantoms illustrate the ability of SQUID measurement to capture both the amount and position of the magnetic field generated by the source. The model suggests a way to quantitatively locate the NPs in tissue, providing a means for the detection of early stage tumors and thereby offering an alternative imaging technique for clinical applications.

2.4 Reference

1. McCarthy, J.R. and R. Weissleder, *Multifunctional magnetic nanoparticles for targeted imaging and therapy.* Advanced Drug Delivery Reviews, 2008. **60**(11): p. 1241-1251.

2. Sun, C., J.S.H. Lee, and M.Q. Zhang, *Magnetic nanoparticles in MR imaging and drug delivery.* Advanced Drug Delivery Reviews, 2008. **60**(11): p. 1252-1265.

3. Mahdi, A.E. and D.J. Mapps. *High-T-c SQUIDs: the ultra sensitive sensors for non-destructive testing and biomagnetism*. in *2nd European Conference on Magnetic Sensors and Actuators*. 1998. Sheffield, England: Elsevier Science Sa.

4. Brittenham, G.M., et al., *Magnetic-Susceptibility Measurement Of Human Iron Stores.* New Engl. J. Med., 1982. **307**(27): p. 1671-1675.

5. Cohen, D., *Ferromagnetic Contamination In Lungs And Other Organs Of Human Body.* Science, 1973. **180**(4087): p. 745-748.

6. Tanaka, S., et al., *Lymph-node detection system using a high T-c SQUID and ultra-small particles.* IEICE Trans. Electron., 2002. **E85C**(3): p. 687-690.

7. Chemla, Y.R., et al., *Ultrasensitive magnetic biosensor for homogeneous immunoassay.* Proc. Natl. Acad. Sci. U. S. A., 2000. **97**(26): p. 14268-14272.

8. Enpuku, K., et al., *Application of HTS SQUIDs to biological immunoassays.* Physica C-Superconductivity and Its Applications, 2004. **412-14**: p. 1473-1479.

9. Weitschies, W., et al., *Determination of relaxing or remanent nanoparticle magnetization provides a novel binding-specific technique for the evaluation of immunoassays.* Pharm. Pharmacol. Lett. , 1997. **7**: p. 1-7.

10. Shi, X.Y., et al., *Dendrimer-functionalized shell-crosslinked iron oxide nanoparticles for in vivo magnetic resonance imaging of tumors.* Adv. Mater., 2008. **20**(9): p. 1671-1678.

11. Wang, S.H., et al., *Dendrimer-functionalized iron oxide nanoparticles for specific targeting and imaging of cancer cells.* Adv. Funct. Mater., 2007. **17**(16): p. 3043-3050.

12. Enpuku, K., et al., *Detection of magnetic nanoparticles with superconducting quantum interference device (SQUID) magnetometer and application to immunoassays.* Japanese Journal of Applied Physics Part 2-Letters, 1999. **38**(10A): p. L1102-L1105.

13. Enpuku, K., et al., *Application of high T-c SQUID magnetometer to biological immunoassays.* Ieee Transactions on Applied Superconductivity, 2001. **11**(1): p. 661-664.

14. Tanaka, S., et al., *Application of high TcSQUID magnetometer for sentinel-lymph node biopsy.* Ieee Transactions on Applied Superconductivity, 2001. **11**(1): p. 665-668.

15. Tanaka, S., et al., *Detection of magnetic nanoparticles in lymph nodes of rat by high T-C SQUID.* Ieee Transactions on Applied Superconductivity, 2003. **13**(2): p. 377-380.

16. Yang, T.Q., et al., *Detection of magnetic nanoparticles with ac susceptibility measurement.* Physica C-Superconductivity and Its Applications, 2004. **412-14**: p. 1496-1500.

17. Enpuku, K., et al., *Magnetic immunoassays utilizing magnetic markers and a high-T-C SQUID.* Ieee Transactions on Applied Superconductivity, 2005. **15**(2): p. 660-663.

18. Kawagishi, K., et al., *Detection of fine magnetic particles coated on a thread using an HTS-SQUID.* Physica C-Superconductivity and Its Applications, 2004. **412-14**: p. 1491-1495.

19. Kotitz, R., et al., *SQUID based remanence measurements for immunoassays.* Ieee Transactions on Applied Superconductivity, 1997. **7**(2): p. 3678-3681.

20. Tsukamoto, A., et al., *Development of multisample biological immunoassay system using HTS SQUID and magnetic nanoparticles.* Ieee Transactions on Applied Superconductivity, 2005. **15**(2): p. 656-659.

21. Grossman, H.L., et al., *Detection of bacteria in suspension by using a superconducting quantum interference device.* Proc. Natl. Acad. Sci. U. S. A., 2004. **101**(1): p. 129-134.

22. Haller, A., et al., *Low T-c SQUID measurement system for magnetic relaxation immunoassays in unshielded environment.* IEEE Trans. Appl. Supercond., 2001. **11**(1): p. 1371-1374.

23. Lange, J., et al., *Magnetorelaxometry - a new binding specific detection method based on magnetic nanoparticles.* J. Magn. Magn. Mater., 2002. **252**(1-3): p. 381-383.

24. Lee, S., et al., *Magnetic gradiometer based on a high-transition temperature superconducting quantum interference device for improved sensitivity of a biosensor.* Appl. Phys. Lett., 2002. **81**(16): p. 3094-3096.

25. Enpuku, K., et al., *Biological immunoassay utilizing magnetic marker and high T-c superconducting quantum interference device magnetometer.* Jpn. J. Appl. Phys., 2003. **42**(12A): p. L1436-L1438.

26. Enpuku, K., et al., *Quantitative evaluation of magnetic immunoassay with remanence measurement.* Supercond. Sci. Technol., 2006. **19**: p. S257-S260.

CHAPTER 3

SQUID Magnetorelaxometry

3.1 Introduction

Magnetorelaxometry (MRX) is the measurement of the magnetization relaxation process of magnetic NPs after they are polarized in a biasing field by quickly removing the field. Common detectors used to record the magnetic signal change over time include fluxgate [1-3] and SQUID.[4-6] Since the magnetic signal change is very weak, SQUID, the most sensitive magnetic field sensor, is promising and has been used widely.

In the SQUID-MRX measurement, magnetic NPs are first aligned in a transient biasing field and the decaying signal is then recorded after the field is switched off. There is typically a short time delay (15 ~ 30 ms) [7-9] between the switching-off and the time data taking is started to allow for the magnetizing field to completely disappear. A special circuit needed to be designed and the goal in my system setup is to turn off 100 G magnetic field within a few milliseconds. The measurement time usually varies from 1 sec to a few minutes.

As shown in chapter 1, magnetic NPs have two mechanisms for their magnetic relaxation: Brownian and Néel. The Brownian relaxation is the physical rotation of the NPs which has μsec time scale, while the time constant of Néel relaxation spans several orders of magnitude with particle size varying. Since the measurement of SQUID-MRX can observe the magnetic decay from msec to sec, only particles which have proper size

(i.e. proper time constant of decay) can be detected. This means only a fraction of the NP ensemble contributes to the signal and the percentage of the fraction is the key factor affecting the detection sensitivity.

To address these questions, this chapter is composed of three parts: the system setup, SQUID-MRX characterization of magnetic NPs, and the sensitivity study of the SQUID-MRX measurement. First, the system setup discusses the circuit design that controls the rapid turn-off of the B-field and noise reduction techniques. Second, the characterization section shows how to relate the MRX signal to the amount of NPs and how the signal changes with the size distribution of NPs. Lastly, the sensitivity study attempts to find the best sensitivity by using several commercial Fe_3O_4 NP products with different size distributions. Simulations are performed based on one of the particles' magnetic property and theoretical prediction of sensitivity is proposed.

3.2 SQUID-MRX System Setup

3.2.1 Overall Setup and Measuring Procedure

The schematic diagram of the whole system is sketched in Figure 3.1. To reduce the electromagnetic noise, the SQUID was placed in two shields: a *rf* screen room and a mu-metal tube. To achieve the best shielding effect, the middle set of the pick-up coils was adjusted approximately to be at the midpoint of the mu-metal tube. A control circuit was designed to switch the current on and off in the biasing coil within msec time scale. A computer with a National Instrument 12-bit DAQ board (AT-MIO-16) was used to both trigger the current in the solenoid and digitize the signal acquired from the SQUID controller. Each part of the system will be discussed in detail in the following sections.

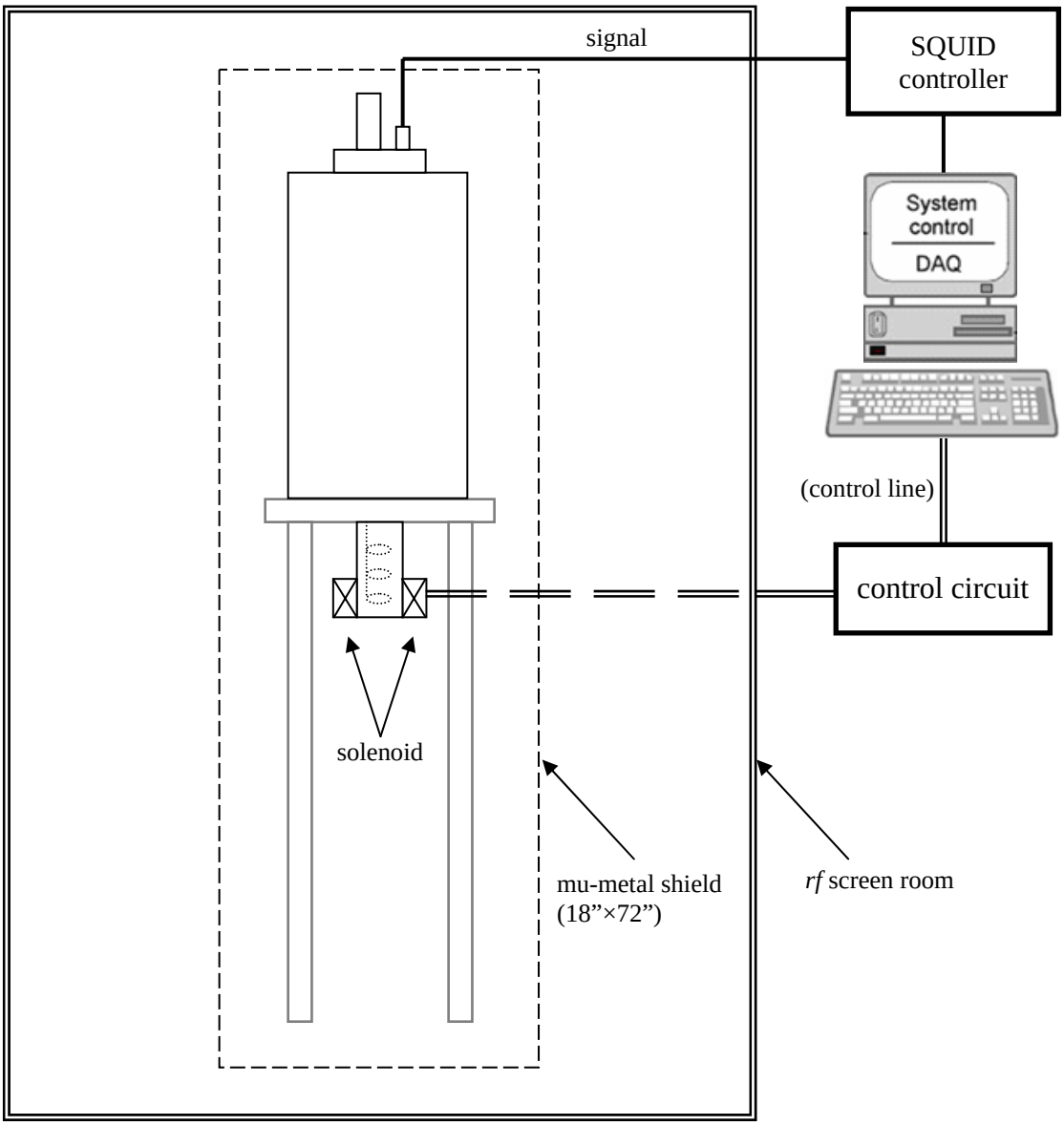

Figure 3.1 Schematic diagram of the SQUID-MRX system setup, which includes two shields for noise reduction, a magnetizing coil with its controller and data taking device.

The measurement sequence designed for my system is following:

(1) apply a reset pulse (5V) to the SQUID feedback controls;

(2) apply current (up to 5 A) to the coil to produce a biasing field for 1 s;

(3) turn off the current quickly (within several ms);

(4) after 15 ms delay, remove the reset pulse and start data acquisition for 1 s.

Due to the existence of unavoidable magnetic field decay not coming from the magnetic NP sample, the background curve needs to be calibrated first. In the absence of any sample, the measuring sequence was repeated 10 times and the data were averaged to determine the background signal. Then a sample was placed beneath the SQUID detector, usually 1.5 cm between the sample and the sensor, and the same pulse was applied 10 times. Signals were averaged to enhance the signal-to-noise ratio and the background was subtracted.

3.2.2 Electromagnet and the Control Circuit

The electromagnet was made in the form of a solenoid by winding copper wires around a plastic spool. The plastic spool has inner diameter 3.35", which is slightly larger than the diameter of the SQUID tail and can be mounted around the tail when it's in use. The solenoid has length 1.06", which fits 14 copper wires of gauge 13 (1.828 mm in diameter) winding in parallel. The copper wire winds the spool in 14 layers while every other layer has 13 turns, resulting in 188 turns in total. The resistance and inductance of the solenoid were measured to be 0.5 Ω and 6 mH respectively. The inductance was also calculated theoretically [10], to be about 5 mH.

After the solenoid was mounted on the SQUID tail, the magnetic field at the center of the solenoid bottom plane (where the NP sample will be placed) was calibrated by using a F.W. Bell series 9900 Gaussmeter. The earth field strength ~ 0.5 G in the z-direction was subtracted from the magnetic field generated by the coil. The data are displayed in Figure 3.2 and the magnetic field increases with current at a rate of 21.6 G/A.

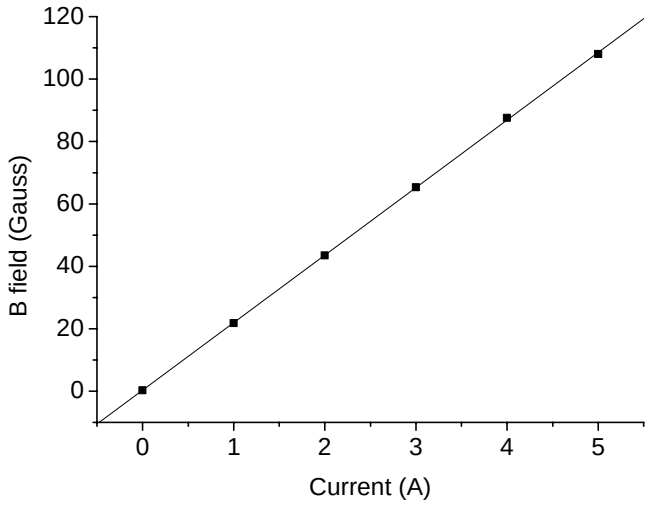

Figure 3.2 The calibration line of the biasing field and current.

The entire electric circuit controlling the solenoid is shown in Figure 3.3. It can be divided into two parts: a fast action switch (the non-shaded part between connectors 1 and 2) and the circuit that handles the energy dissipation after switching off (the shaded part). In both parts, batteries are used as power sources to eliminate AC component that might generate noise. The fast action switch consists of an n-channel MOSFET (JEDEC TO-220AB from Fairchild Semiconductor), a high-speed MOSFET driver (TC1427CPA from Microchip), a battery set (4.5 V) supplying gate voltage for the MOSFET and a TTL signal generator that sets the "on/off" state of the switch. The TTL signal comes from the DAQ board output channel, which can be controlled by a computer. The purpose of using the MOSFET driver is to separate the TTL triggering part (the computer) from the solenoid circuit to minimize the influence from the control side.

In order to release the magnetic field energy stored in the solenoid during a short time, a circuit was designed which can control up to 5 A current (~100 Gauss in terms of the magnetic field) as illustrated the shaded region in Figure 3.3. The basic idea of the

design is by placing a capacitor in parallel with the solenoid, the stored magnetic field energy can be quickly transferred into the electrical field energy stored in the capacitor. Then the energy will be gradually dissipated by a resistor connected to across the capacitor. The diode in the circuit prevents the backflow of current to the coil. A mechanical relay, connected with the solenoid, is used to physically disconnect the coil from the circuit. Due to its intrinsic time delay (about 5 ms), it allows enough time for the majority of the energy to be transferred to the capacitor before it disconnects the circuit.

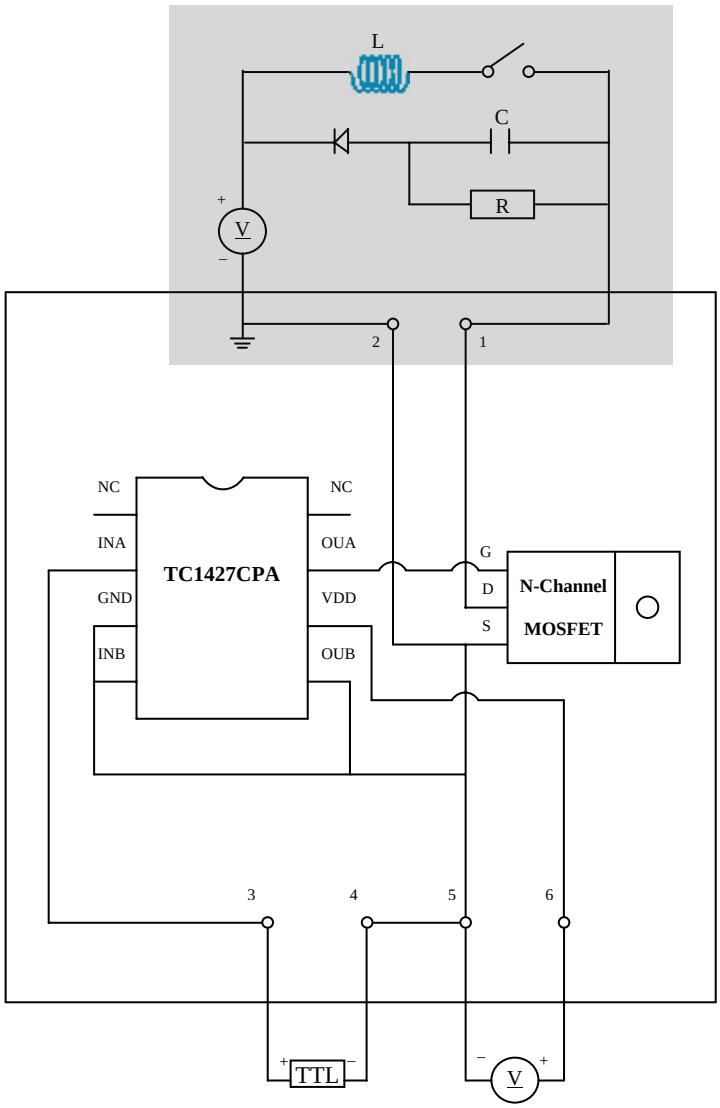

Figure 3.3 Schematic diagram of the circuit controlling the magnetizing coil.

The advantage of this design is that the energy dissipation by the resistor can take a much longer time than that required for the SQUID measurement delay. No high power resistor is necessary and the energy release and measurement can take place at the same time. To find out the specific requirements on the electronic devices in the design, the circuit behavior of the discharging process was theoretically analyzed. During the time that the solenoid is discharging, the following equations are applied

$$-L\frac{dI}{dt}=\frac{\int i_1 dt}{C} \tag{3-1}$$

$$-L\frac{dI}{dt}=i_2 R \tag{3-2}$$

$$I=i_1+i_2 \tag{3-3}$$

where I denotes the current flowing in the solenoid and i_1, i_2 are the currents in the capacitor and the resistor respectively. The equations can be combined and simplified to one 2nd order differential equation of $I(t)$

$$\frac{d^2 I}{dt^2}+\frac{1}{RC}\frac{dI}{dt}+\frac{1}{LC}I=0 \tag{3-4}$$

By solving this equation, the eigenvalues are found to be

$$\lambda_{1,2}=\frac{-1\pm\sqrt{1-4\frac{R^2 C}{L}}}{2RC}$$

The discharging behavior has three scenarios depending on the values of R, C and L.

i) $4\frac{R^2 C}{L}=1$, critical damping

ii) $4\frac{R^2 C}{L}<1$, over damping

iii) $4\frac{R^2C}{L} > 1$, under damping

Theoretically, the solution for each scenario can be obtained and compared. The one that has the least electrical requirements on the resistor and capacitor will be the choice. However, there is a simpler way to determine the answer. By doing some mathematical rearrangements on the discriminant, we get:

$$\frac{R^2C}{L} = \frac{R^2C^2}{\left(\sqrt{LC}\right)^2} = \left(\frac{\tau_{RC}}{\tau_{LC}}\right)^2$$

where, τ_{RC} and τ_{LC} are the characteristic time of the *RC* and *LC* circuit. In order for the energy to transfer from the inductor to the capacitor in a shorter time than to be released by the resistor, the characteristic time of the *RC* circuit needs to be much greater than the *LC* circuit. This means $\frac{R^2C}{L} >> 1$ must be satisfied and case (iii) (the under damping mode) is the choice. Under this approximation and with the initial conditions, the eigenvalues and the solutions to the differential equations are

$$\lambda_{1,2} = \frac{-1 \pm 2iR\sqrt{\frac{C}{L}}}{2RC} = -\gamma \pm i\omega$$

$$I(t) = I_0 e^{-\gamma t}\cos\omega t$$

$$i_1(t) = I_0 e^{-\gamma t}\left(\cos\omega t - \sqrt{\frac{L}{R^2C}}\sin\omega t\right)$$

$$i_2(t) = I_0 e^{-\gamma t}\sqrt{\frac{L}{R^2C}}\sin\omega t$$

where $\gamma = \frac{1}{2RC}$ and $\omega = \sqrt{\frac{1}{LC}}$.

Due to the presence of a diode, current can not flow back to charge the solenoid. So the solution works only for T/4 (where T is the period) from the beginning of discharging. Assuming at time t_1 the discharging completes, so $t_1 = \frac{\pi}{2}\sqrt{LC}$, which is the theoretical minimum delay time of the MRX measurement. Once the t_1 value is set (for example 1 ms), the capacitance can be determined. Then the resistance can be calculated depending on how long we choose for the energy to dissipate on the resistor (usually a few seconds). The longer dissipation time requires lower power requirements for the resistor.

Finally, the capacitor was chosen with C = 33 μF and maximum voltage = 100V, while the resistor has R = 15 kΩ. For these values, t_1 = 0.7 ms and τ_{RC} = 0.5 s. It can be further shown that for a field of 100 Gauss (I_0 = 5A), the maximum voltage appearing on the capacitor is no more than 67 V, which is lower than the capacitor's break down voltage. The maximum current through the resistor happens at time t_1, which is equal to 0.0045 A. Thus the maximum instantaneous power consumption on the resistor is only 0.3 W. Compared with a resistor-only discharging circuit, to release the energy within t_1 = 0.7 ms the average power is over 100 W, which requires an array of resistors. Our design is easier to implement and potentially can handle even higher biasing fields.

Using the Gaussmeter, the field change after the control circuit is switched off was recorded. To observe the whole process of the field decaying, the DQA board was set to start recording the magnetic field 10 ms earlier than the "off" TTL signal was sent out. Due to the delay of the DAQ board, the turn-off time of the field is 9.5 ms, as shown in Figure 3.4. And after 2 ms, the residual magnetic field was reduced to a level that can not be sensed by the Gaussmeter.

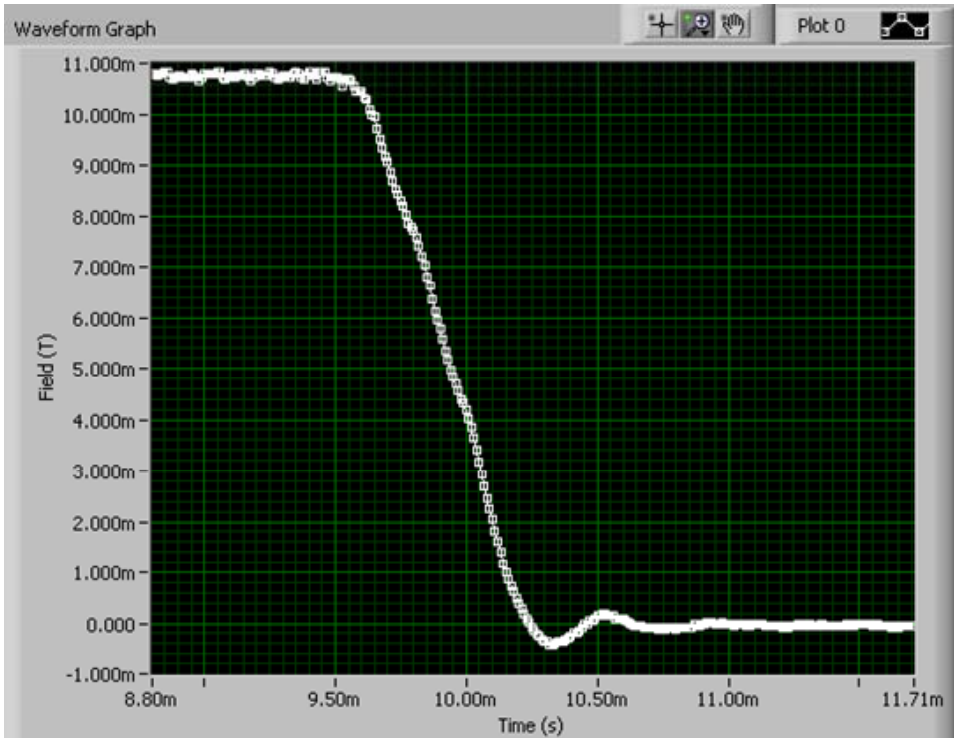

Figure 3.4 Switching off behavior of the biasing field recorded by the Gaussmeter.

3.2.3 Noise Reduction Technique – Hardware

SQUID operations can be disturbed by electromagnetic (EM) fields from a wide range of sources including power cables, transformers, motors, computers and permanent magnets. Unlike the remanence measurement using a lock-in amplifier to eliminate noise, MRX records the magnetic decay of NPs at all frequencies. So adequate shielding of both radio frequency (*rf*) and low-frequency screening is necessary to achieve high SQUID-MRX sensitivity.

When an EM wave encounters a piece of metal, part of the wave can penetrate into it and experience an exponential decay of amplitude. The decay can be expressed by $\exp(-d/\delta)$, where d is the distance into the metal that the wave travels and δ is the

penetration depth. For the case of metals, δ can be very small and the EM field is confined in a thin layer close to the surface. This effect is known as the skin effect and δ is usually called the skin depth, which is determined by [11, 12]:

$$\delta = \left(\frac{1}{\pi \mu \sigma f} \right)^{1/2}$$

where permeability $\mu = \mu_r \mu_0$ (μ_r is the relative permeability and $\mu_0 = 4\pi \times 10^{-7}$ is the permeability of vacuum), σ is the electrical conductivity and f is the EM wave frequency. Since the skin depth is dependent on frequency, the *rf* and low-frequency EM noise have to be dealt with different materials.

Two shields are used to reduce the noise on the SQUID, as illustrated in Figure

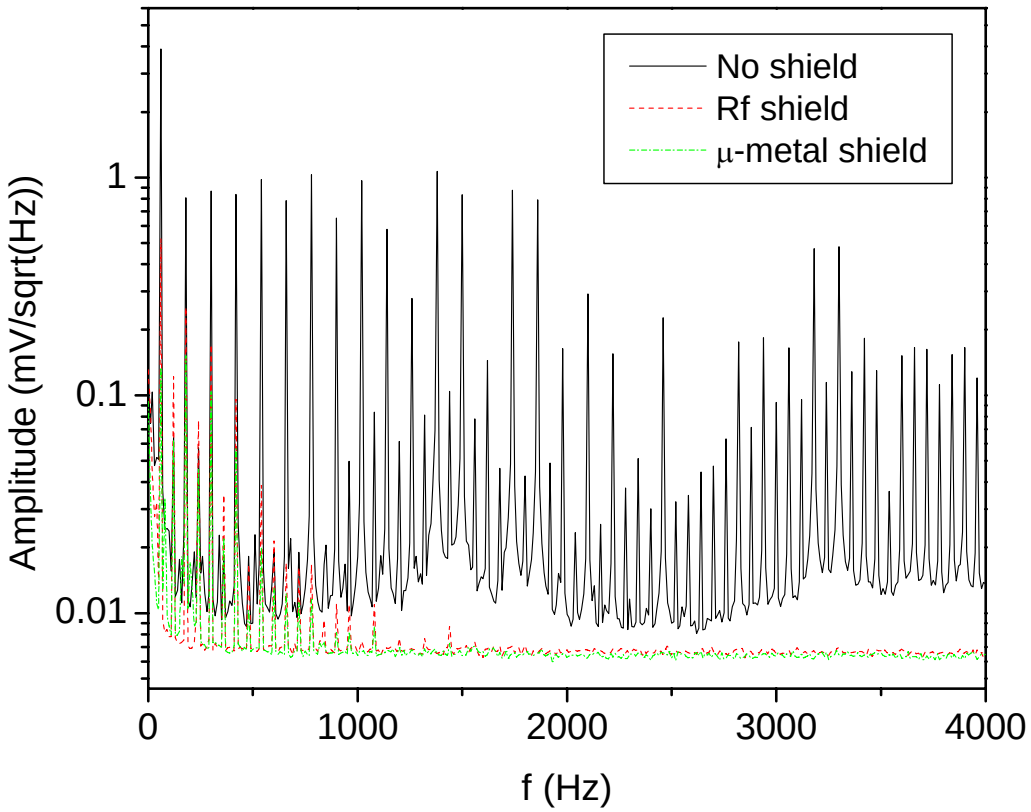

Figure 3.5 The noise level analysis of the SQUID system with the two shields.

3.1. The copper screen room is effective in screening out the *rf* interference (kilohertz and higher). Another inner shield is made of mu-metal with μ_r = 50,000, which can greatly decrease the skin depth of low-frequency waves which are usually generated by power lines and moving magnetic objects. This shield has a cylindrical shape with diameter 18" and height 72". A Hewlett Packard signal analyzer (model 3561A) was used to characterize the noise level of the SQUID. As can be seen in Figure 3.5, the noise at frequencies higher than 1 kHz was significantly suppressed by two orders of magnitude. And the mu-metal further decreases the low frequency component, for example 60 Hz, to about ¼ of the original level.

3.2.4 Noise Reduction Technique – Software

As can be seen from Figure 3.5, the shields are not able to eliminate all the noise, especially the 60 Hz component and the harmonics. Therefore, several algorithms on data processing were developed to enhance the signal-to-noise ratio. These techniques include a moving average of the time course curve, Fourier transform and averaging over a number of trials. The moving average averages every four data points on the relaxivity curve. The Fourier transform was used to minimize the influence of 60 Hz EM waves from power lines. The frequency spectrum is generated and the spikes at 60 Hz and its harmonics are removed and transformed back to the real time space. Averaging a measurement N times can improve the signal-to-noise ratio by a factor of $\sqrt{N}$.

The system was controlled by a computer through the GPIB interface. The program was implemented with LabVIEW software and a control panel was designed for operation. From there, the number of iterations, time delay after field switching off, parameters of noise reduction methods and the fitting model can all be adjusted.

3.3 SQUID-MRX Characterization of Magnetic NPs

3.3.1 Methods

Maghemite NPs (Fe_2O_3, gamma, 99+%, from Alfa Aesar, USA) were centrifuged at a series of speeds to separate the NPs by size. Certain amount of NPs were dissolved in water, vortexed to a form uniform suspension in a tube and sent for centrifuging. After the centrifugation, the suspension was extracted and transferred to another tube and the precipitate was dissolved in water for later usage. The extracted suspension was centrifuged at a higher speed to precipitate smaller particles. The above procedure was repeated three times more to produce four ferrofluids of Fe_2O_3 NPs. The experimental parameters for centrifugation are 2000 rpm for 6 min, 3000 rpm for 7 min, 4500 rpm for 7 min and 11000 rpm for 7 min sequentially.

The NP concentration of each ferrofluid was determined by the dry weight measurement. Specifically, four glass bottles were desiccated and weighed. Then 200 μl of suspension from each ferrofluid was transferred to a bottle and desiccated overnight. The new weights of the bottles were measured and the concentration of the NPs can be calculated by dividing the mass different with the 200 μl volume.

Transmission Electron Microscopy (TEM) was used to study the size of the NPs. A Philips CM-100 microscope equipped with a Hamamatsu digital Camera ORCA-HR operated using AMT software (Advanced Microscopy Techniques Corp, Danver, MA) was used to acquire the NPs' morphology. The operation voltage was kept at 60kV. To prepare the TEM sample, a small volume of the iron oxide colloidal suspension (5 μl) was released onto a 200-mesh carbon film coated copper grid and air-dried before is was loaded into the microscope.

Specimens for SQUID-MRX measurement were prepared as dry samples, the details of which are described in Chapter 2. Briefly, a droplet of NP solution was absorbed by a piece of filter paper (typically 0.5 × 0.5 cm^2) and dried at room temperature. Then this piece of paper is placed beneath the SQUID detector for measurement.

By drying the ferrofluid on filter paper, the NPs are immobilized and magnetic relaxation can only happen through the Néel mechanism. For each individual NP, the relaxivity takes an exponential form, the rate of which is determined by the Néel relaxation time constant. However, the average decay behavior of an NP ensemble takes a logarithmic form due to the size distribution of these NPs. In terms of the magnetic field that is emanating from the NPs and detected by the SQUID, the decay can be expressed as

$$B(t) = B' + B_0 \ln(1 + \frac{t_c}{t}) \tag{3-5}$$

where the characteristic time $t_c = t_{mag}$ (time of biasing field applied) in the weak field approximation.[13] Since SQUID only detects changes in magnetic field, B' has no physical significance because it means an arbitrary static field. B_0 reflects the amplitude of the decay, which contains the sample information.

The MRX measurement was performed in an unshielded environment. The biasing field that was applied was about 100 G for 1 s. The delay time was 15 ms and the SQUID recording time was 1 s. Each experimental curve was an average over ten measurements and the constant background decay was subtracted from the signal. Five experimental curves were acquired for each sample. They are fitted by using equation (3-5) and the fitting parameters are then averaged for plotting.

3.3.2 Results and Discussion

A typical relaxivity curve is shown in Figure 3.6, where the "no sample" curve was acquired in the absence of the NPs after the background was subtracted and the other curve measured in the presence of 120 μg Fe_2O_3 NPs shows clear signal decay versus time. The curves "thickness" or noise fluctuation is about 15 pT, which was achieved in the unshielded environment after the software filtering was applied. The "thickness" is a key factor in the detection limit since when the overall decay is smaller than the fluctuation, fitting curves can not be accurately determined.

By applying equation (3-5) to fit the experimental curve with NPs, the best-fit parameters B' and B_0 can be determined to be 218.9 and 80.7 pT, respectively. The value of B' is a random number from one trial to another and can be ignored because it contains

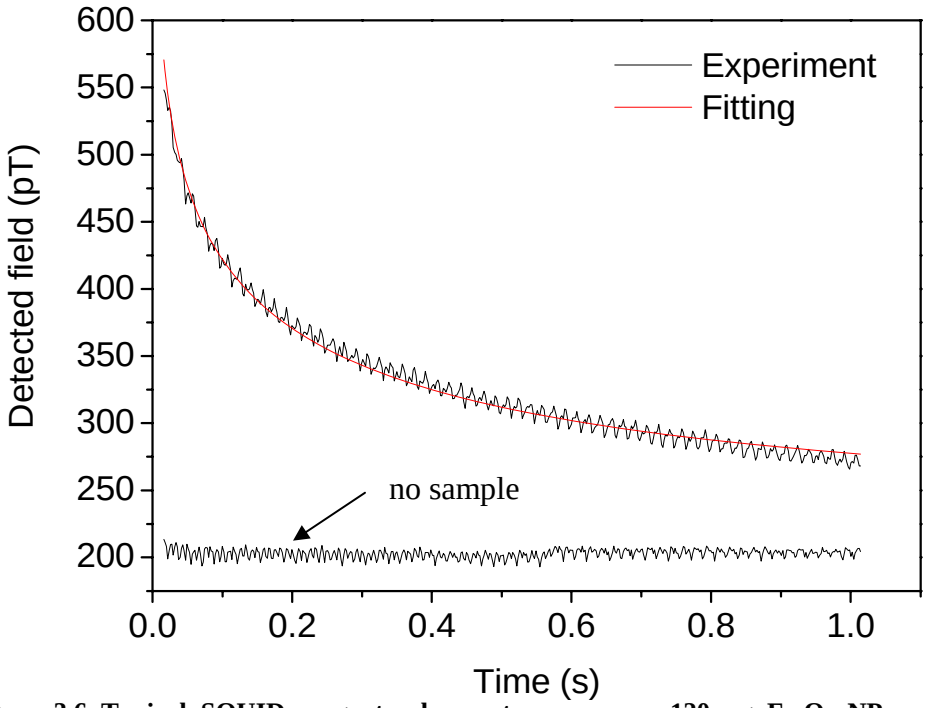

Figure 3.6 Typical SQUID magnetorelaxometry curve on 120 μg Fe_2O_3 NPs with theoretical fitting $B(t) = B_0\ln(1+1/t)+ B'$, where B_0 = 80.7 pT and B' = 218.9 pT. The factor B_0 is proportional to the amount of NPs as shown in Figure 3.7.

no information about the sample. B_0 depends on a number of parameters, which includes the excitation field strength and exposure time, SQUID recording time, distance from the sample to the SQUID detector, temperature, magnetic properties and mass of the NPs.

However, as long as the SQUID measuring parameters are kept fixed and the measured NPs are from the same product, the mass of the NPs is the only factor that affects B_0. Different amounts of NPs (from 15 to 120 μg) were measured and curves were fitted using the same procedure as described above. This relationship between the amount of NPs and the fitting parameter B_0 was found to be linear, as illustrated by Figure 3.7. The slope of the curve (0.6975 pT/μg) represents the sensitivity of MRX on this particular NP ensemble and can be used to characterize the NPs.

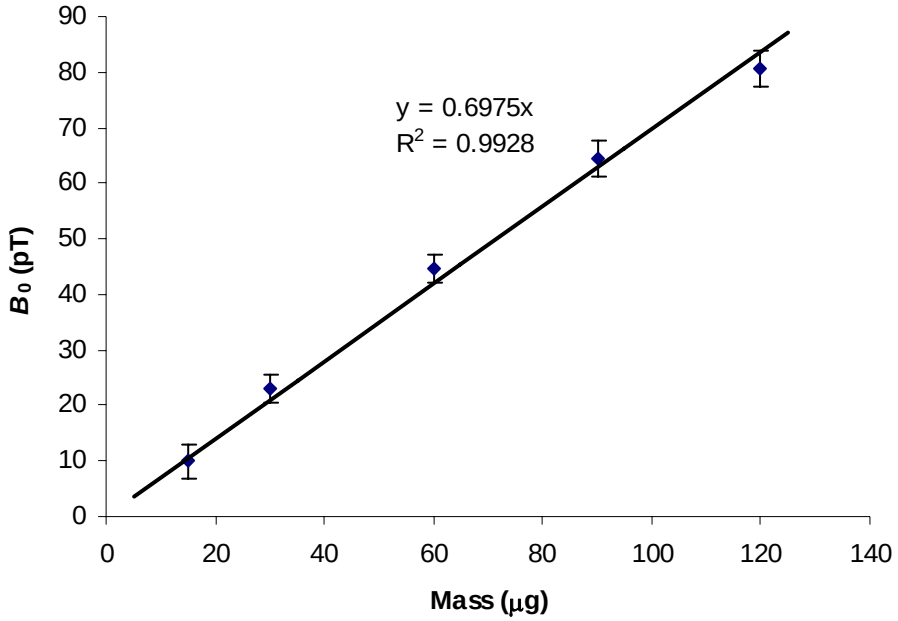

Figure 3.7 The calibration curve shows a linear relationship between the magnetic decay amplitude (B_0 fitted from equation (3-5)) and the mass of Fe_2O_3 NPs. All data points were obtained by averaging over 50 measurements.

In the MRX technique, only a small fraction of the NPs can be observed due to the fact that particles with different sizes have different relaxation time scale. Therefore, a way to increase the measurement's sensitivity is to change the NPs' size distribution. Figure 3.8 shows a TEM image of the original particles and about 300 NPs were selected for diameter measurement to generate the statistical histogram. These particles have mean diameter 25 nm with standard deviation 19 nm. Then centrifugation was applied to separate the particles by their size and four ferrofluids were formed and labeled as A, B, C and D. TEM images were taken on each separated NP sample and their diameters were measured and statistically analyzed, yielding (A) 63 ± 27 nm, (B) 43 ± 17 nm, (C) 33 ± 11 nm, and (D) 20 ± 9 nm, as shown Figure 3.9.

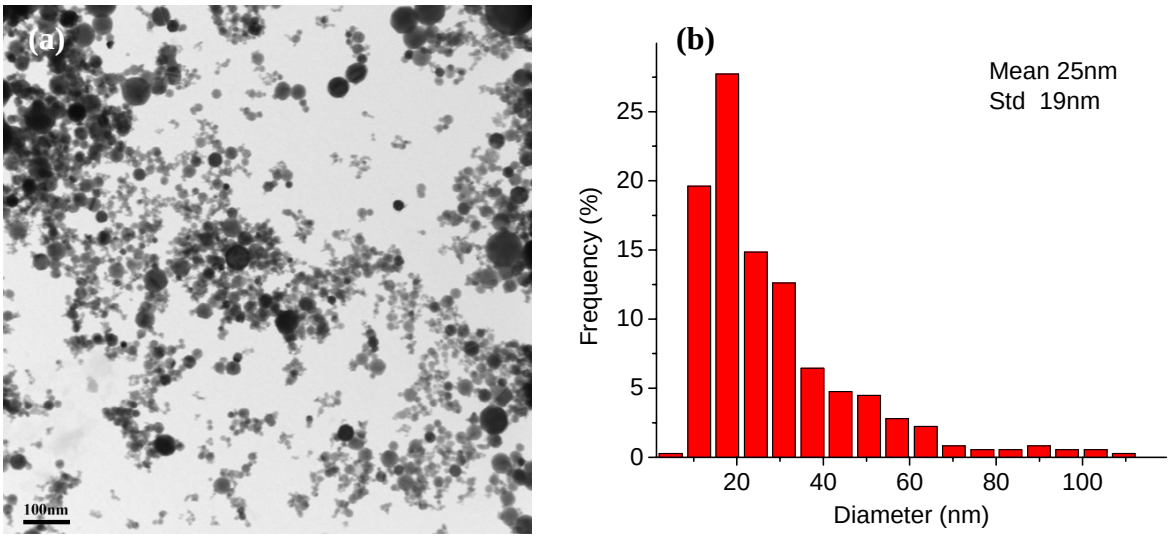

Figure 3.8 (a) A TEM image of the Fe_2O_3 NPs, (b) the size distribution histogram obtained by statistically measuring about 300 particles

To compare the MRX signal of these separated NPs to the original one, the same amount of NPs from each ferrofluid was calibrated using the same SQUID parameters. Figure 3.10 shows the relaxivity curves on 120 μg NPs from A, B, C, D as well as the original NP sample. The magnetic decay amplitude B_0 of each curve is summarized in

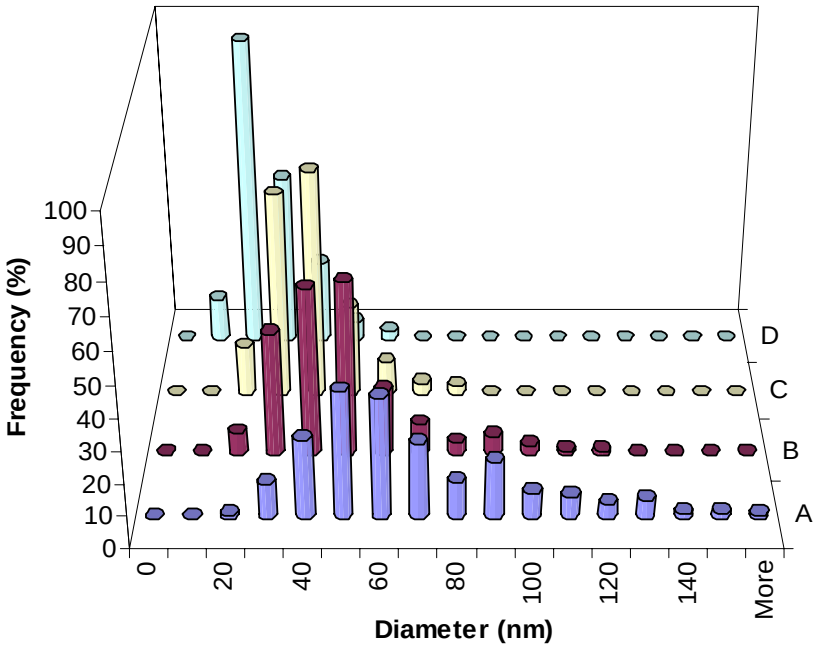

Figure 3.9 Size distribution histograms of the NPs after centrifugation. (A) 63 ± 27 nm, (B) 43 ± 17 nm, (C) 33 ± 11 nm and (D) 20 ± 9 nm.

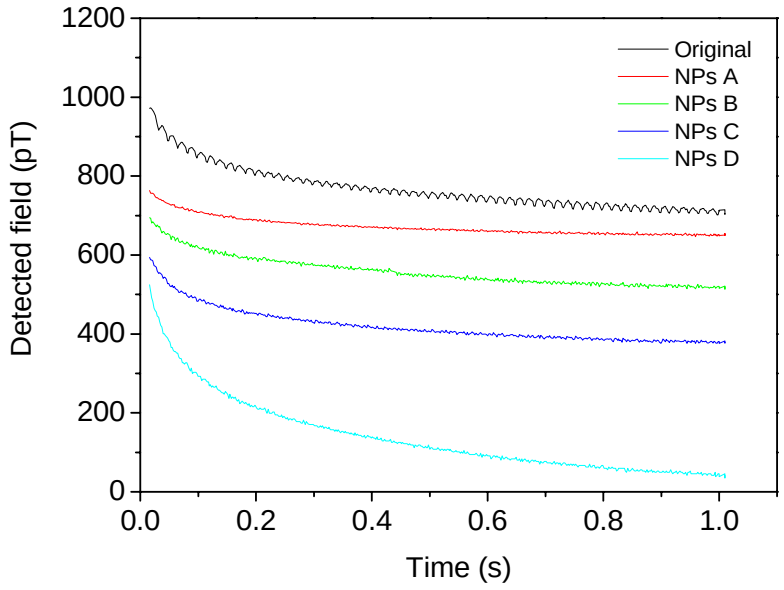

Figure 3.10 Comparison of the SQUID-MRX relaxivity curves on 120μg Fe_2O_3 NPs of different size distributions.

Table 3.1, where ferrofluid D exhibits the largest decay with B_0 = 143.4 pT. More measurements were performed with different masses of these NPs samples. The magnetic

decay amplitudes were plotted versus the mass of NPs in Figure 3.121. Sample D shows the largest slope, which is 1.7 times bigger than the slope of the original NPs, implying a 1.7-fold enhancement of the sensitivity was achieved. This phenomenon matches our expectation because the NP's relaxivity time depends on its size. The Néel relaxation of magnetic NPs is described by

$$\tau_B = \tau_0 \exp(KV / k_B T) \tag{3-6}$$

where τ_0 is usually quoted as 10^{-9} s and K is the magnetic anisotropy constant. Assuming the bulk-Fe_2O_3 K value (2.5×10^4 J/m^3) [14], the relaxivity time constant is 2.62 s at particle diameter of 19 nm. Since sample D has NPs with a mean diameter of 20 nm, it has the higher fraction of NPs around the optimal size, these leading to the highest detection sensitivity. To roughly verify this hypothesis, we assume that the NP's diameter distribution follows the lognormal form. Then the probability densities at 19 nm of D and the original samples are 0.049 and 0.031 respectively. The ratio of the densities is about 1.6, which is close to the sensitivity enhancement.

Table 3.1 Summary of SQUID-MRX decay amplitudes of 120 μg Fe_2O_3 NPs versus size distributions.

	Original	NPs A	NPs B	NPs C	NPs D
Diameter (nm)	25 ± 19	63 ± 27	43 ± 17	33 ± 11	20 ± 9
Decay amplitude B_0 (pT)	80.7	33.7	56.2	63.5	143.4

According to the NP concentration of A to D determined by the dry weight method, the original NPs can be viewed as a composite of A to D neglecting the loss of particles during the separation procedure. Based on these ferrofluids' concentrations, the

mass ratio of A to D in the original NP product is approximately 3:1:1:2. Using the slopes of the lines of NPs A to D in Figure 3.11, we can calculate that the sensitivity of the original NPs is equal to 0.6, which is approximately equal (14% less) to the measured value.

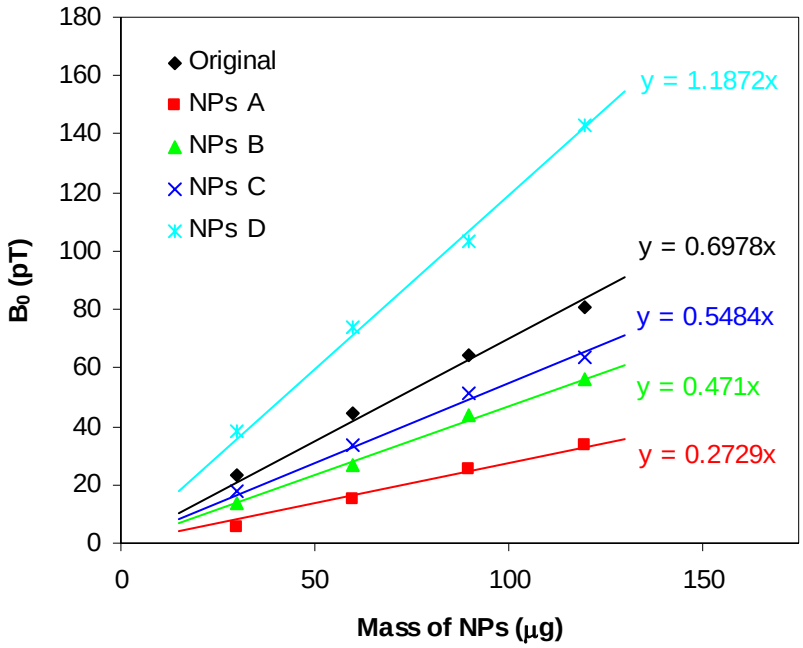

Figure 3.11 SQUID-MRX sensitivity study of the Fe_2O_3 NPs with different size distributions.

3.4 The Sensitivity Study of SQUID-MRX

3.4.1 Methods

Hardware shielding was used to reduce the noise level in the recorded signal as described in section 3.2.3. Due to the high permeability of the mu-metal, it can be easily magnetized when the magnetizing field for magnetic NPs is applied and will in turn affect the SQUID data. So the biasing field was reduced to 15 G to avoid the

demagnetization of the mu-metal being detected by SQUID. Other experimental parameters were kept the same as the previous section.

Because some of the magnetic NPs are coated with a certain surfactant to both increase the bio-compatibility and reduce the particles' interaction, they are not pure iron oxide. Inductively Coupled Plasma – Mass Spectroscopy (ICP–MS) was used to determine the iron content of each sample for directly comparing their sensitivities. NPs were weighted and dissolved in a volume of strong acid, such as nitric acid or aqua regia. The iron concentration was measure by ICP–MS and the iron content in each particle can be calculated.

The magnetic properties of the NPs were studied by a Quantum Design MPMS-5 SQUID magnetometer (San Diego, CA) at room temperature. Ferrofluid containing a known amount of NPs was dropped onto a piece of filter paper. The sample was dried in air to immobilize the NPs and loaded into a plastic capsule for measurement.

3.4.2 MRX Sensitivity on Various Fe_3O_4 NPs

A relaxation curve as well as a "no sample" curve is shown in Figure 3.12, where "no sample" represents the no-particle background signal. The relaxation was measured on 10 μg of Chemicell product 1811. Compared with Figure 3.6, the "thickness" of the curve was reduced to 3 pT in the presence of the two shields, which means a five-time enhancement on the noise reduction.

Due to the size dependence of the MRX signal, eight different Fe_3O_4 NPs with various diameters were selected for the sensitivity study. Four of them were obtained from Chemicell GmbH Inc, which were already coated with starch. They are labeled as CC 1811, CC 1911, CC 2011 and CC 1502. Two came from Nano Armor: NA I and NA

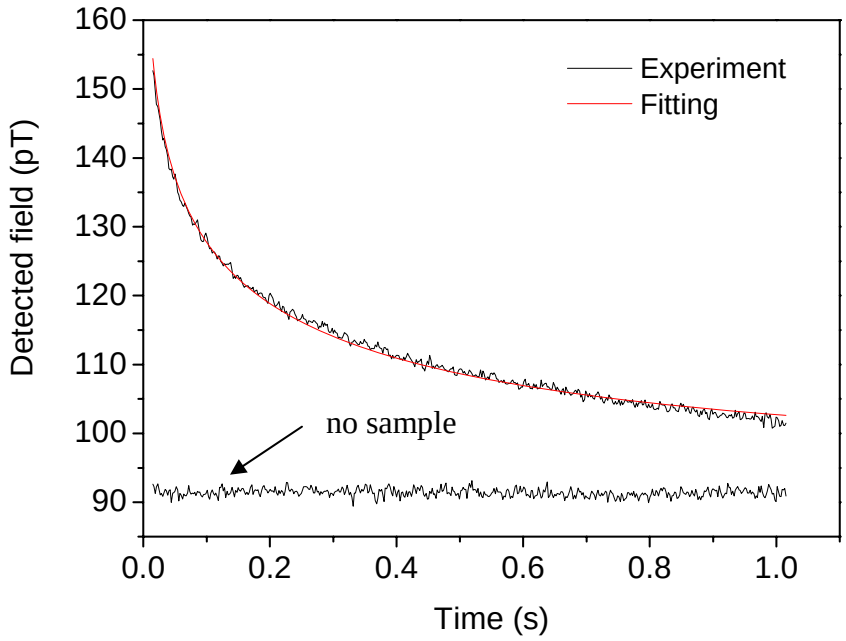

Figure 3.12 Typical SQUID magnetorelaxometry curve on 10 μg CC1811 NPs measured in the screen rooms. The fitting parameters are B_0 = 92.5 pT and B' = 14.7 pT.

II. One was purchased from Meito Sanyo Co. Ltd with Dextran as the surface layer. The eighth sample was synthesized in our group (#229-89) and the detailed protocol can be found in the reference [15]. The diameters of these NPs were characterized by measuring about 300 particles of each product from the TEM images. The results are summarized in Table 3.2. For Néel relaxation investigations, the anisotropy constant K of Fe_3O_4 NPs is commonly used as (1-5) × 10^4 J/m^3.[16, 17] By using equation (3-6), for the relaxation time to match the measurement time scale, the NP size must vary from 12 to 25 nm. The diameters of the chosen NPs range from 8 to 26 nm, covering the theoretical size scope.

MRX measurements were performed on the above NPs, the relaxivity curves were fitted and the decay amplitudes (B_0) were plotted versus the calculated amount of iron in Figure 3.13. All the particles exhibit linear relationship between the decay amplitude B_0 and the mass of iron but they have different slopes or different sensitivities.

Table 3.2 The size distribution of the Fe_3O_4 NPs used in the MRX sensitivity study.

	CC 1811	CC 1911	CC 2011	CC 1502
Diameter (nm)	12 ± 3	8 ± 2	11 ± 3	14 ± 3
	Meito	229-89	NA I	NA II
Diameter (nm)	9 ± 2	8.4 ± 1.4	15 ± 3	26 ± 6

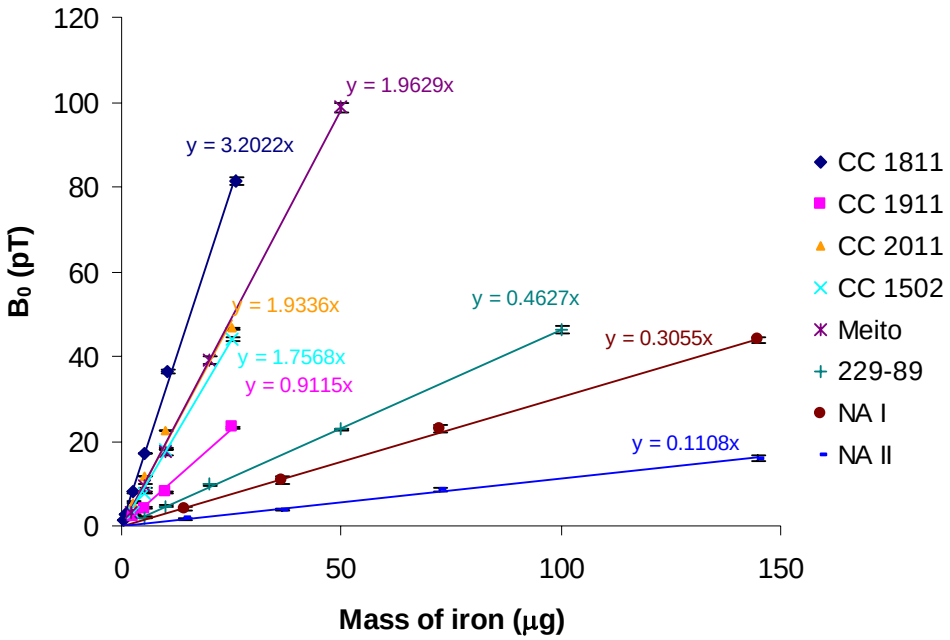

Figure 3.13 MRX sensitivities on various Fe_3O_4 NP samples. The lines are calibrated with the mass of iron was due to different Fe_3O_4 mass percentage in each sample.

The sensitivity of each type of NPs was plotted in Figure 3.14 against the mean diameter. Product CC 1811 shows the highest sensitivity (3.2 pT/μg Fe), which decreases when the NPs are either larger or smaller. If we set the lowest detectable amount to when the overall decay equals the "thickness" of the relaxivity curve (3 pT), the fitting

parameter B_0 is about 1 pT. So the detection limit on product CC 1811 is about 300 ng of iron.

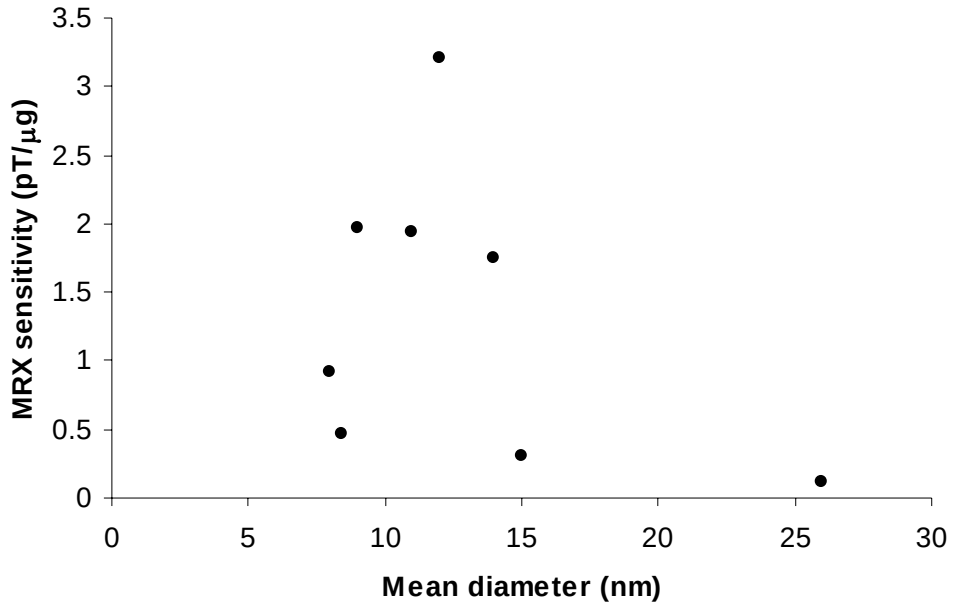

Figure 3.14 The dependence of the MRX sensitivity on the mean size of Fe_3O_4 NPs.

Figure 3.14 may not quantitatively reflect the sensitivity dependence on size because the NPs were prepared in different ways and are not likely to have the same anisotropy constant value. But it suggests that the sensitivity of MRX is much lower than remanence measurements due to the contribution from only a small portion of NPs. How sensitive can SQUID-MRX be: nanogram or sub-microgram? A computer simulation of the MRX process was applied to address this question.

3.4.3 The Theoretical Model Description

We study the magnetization process of a single magnetic NP in the presence of a weak field. Without losing generosity, we assume that the angle between the easy axis

and the biasing field $\boldsymbol{B}$ is φ and the angle between the magnetization vector $m = M_s V$ (where M_s is the saturation magnetization) and $\boldsymbol{B}$ is θ, as depicted in Figure 3.15. Then the energy of the particle is given by

$$E(\theta) = KV\sin^2(\theta) - mB\cos(\varphi) = KV\left(\sin^2(\theta) - 2h\cos(\varphi)\right) \tag{3-7}$$

where K is the anisotropy constant and V is the size of the particle. For simplicity, h is

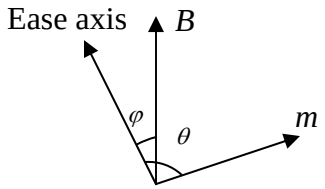

Figure 3.15 Schematic diagram of a magnetic NP orientation.

defined as $h = B/B_K = B/(2K/M_s)$, which B_K is called the anisotropy field. For the small field approximation, $h << 1$ and the presence of the biasing field B can be regarded as a perturbation on the magnetic anisotropy energy. In this case, the energy maximum and minimum occurs approximately at $\theta = \pi/2$ and $\theta = \pi$. The energy barrier for the magnetic moment to rotate into the biasing field direction is

$$\Delta E = E\left(\theta = \frac{\pi}{2}\right) - E(\theta = \pi) = KV\left(1 - 2h\left(\cos\varphi + \sin\varphi\right)\right) \tag{3-8}$$

Then the relaxation time into this field direction is dependent on the angle between the $\boldsymbol{B}$ and the easy axis.

$$\tau_H(\varphi) = \tau_0 \exp\left(\frac{\Delta E}{K_B T}\right) = \tau_0 \exp\left(\frac{KV}{K_B T}\left(1 - 2h\left(\cos\varphi + \sin\varphi\right)\right)\right) \tag{3-9}$$

Note that when the external field is zero, this equation reduces to the Néel relaxation formula (3-6). If the magnetizing field is applied for some time t', the magnetization from the particles with volume between V and $V + \mathrm{d}V$ is given by

$$dm = \left(1 - e^{-t'/\tau_H}\right)\chi\rho VBf(V)dV \tag{3-10}$$

where χ is the mass susceptibility, ρ is the density of the NPs and $f(V)$ is the particle volume distribution function. After the biasing field is switched off, the magnetization begins to decay according to the Néel relaxation mechanism. At any moment t, the magnetization of the NP ensemble can be obtained by integrating over all sizes

$$m(t) = \int_0^\infty \left(1 - e^{-t'/\tau_H}\right)e^{-t/\tau_N}\chi\rho VBf(V)dV \tag{3-11}$$

In the simulation, the NPs were partitioned into different volumes with the easy axis taking different orientations. In each particular group, the NPs were regarded as identical particles and their contribution to $m(t)$ was calculated. The total signal was computed by adding all the groups up and fitted by equation (3-5) to compare with the experimental data.

3.4.4 The Sensitivity Study Using the Model

To theoretically study the sensitivity, I chose CC 1811 NPs and studied their magnetization curve because it has the best signal among all the samples in the MRX study. The magnetic hysteresis loop was measured by a Quantum Design SQUID magnetometer, as shown by Figure 3.16. The particles are superparamagnetic and show no remanence at room temperature. The particles' mass susceptibility χ was calculated from the SQUID magnetometry measurement (Figure 3.16), which is 0.0918 emu/g·G per gram of the NP conjugate. Given the iron concentration determined by the ICP–MS 12.9 mg/ml and the NP concentration 25 mg/ml, the χ value for per gram of Fe is 0.178 emu/g·G. By doing this conversion, we can ignore the coating's influence on the particle density and assume the Fe_3O_4 cores having the same density as bulk material, which is

5.1 g/cm^3. Their diameter distribution was characterized by the lognormal distribution according to the size statistics from TEM images (12 ± 3 nm). In the simulation, all other parameters are kept the same as the experiment. To briefly summarize them, the distance from the sample to the SQUID detector was 1.5 cm, the biasing field was 15 G applied for 1 s, the time delay was 15 ms and data were taken for 1 s.

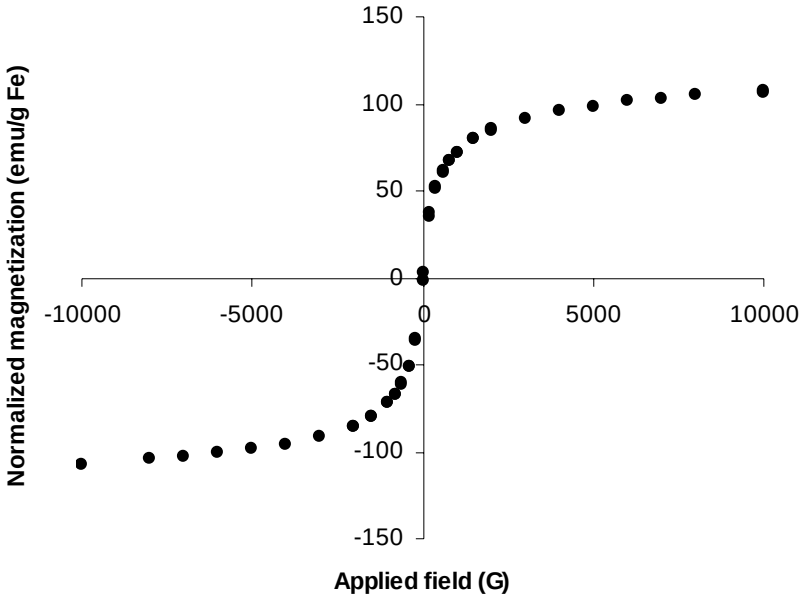

Figure 3.16 Magnetic hysteresis curve of Fe_3O_4 NPs - CC 1811. The data was taken at 20°C and the curve was normalized to per gram of Fe.

Because the experimental relaxivity curve can be very well fitted by equation (3-5), the simulation can also be verified by fitting the simulated data with this equation. Figure 3.17 shows one set of simulation data for 1.38 μg of Fe_3O_4 NPs or 1 μg of Fe in Fe_3O_4 at 20°C. The fitting parameters B' and B_0 are 0.082 and 3.96 pT, respectively. Parameter B_0 also means the measurement sensitivity is 3.96 pT/μg Fe, which is about 1.2 times larger than the experimentally measured value. In the simulation, we assumed the anisotropy constant K = 50 kJ/m^3, which has the highest sensitivity at 20°C. The

discrepancy is probably coming from the real *K* value of the NPs differing from the assumed value. By matching the calculated sensitivity with the experimental value, the *K* value was found to be 33 kJ/m^3.

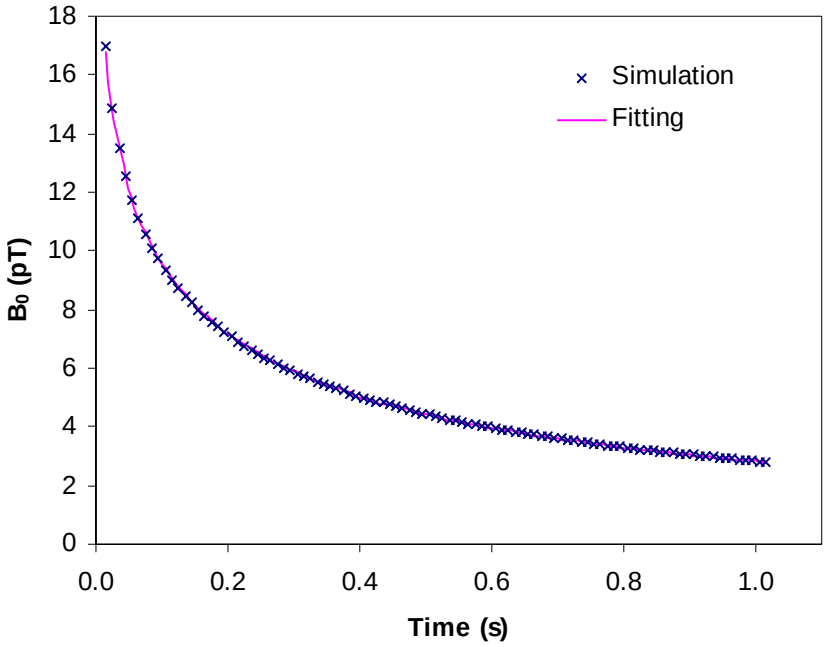

Figure 3.17 A simulated relaxivity curve on 1.38 mg Fe_3O_4 by assuming the magnetic properties of CC 1811 (χ = 0.178 emu/g·G, d = 12 ± 3nm) and K = 50 kJ/m^3 at T = 20°C. The curve was also fitted by equation (3-5) and the best fit parameters were *B*' = 0.082 pT and B_0 = 3.96 pT.

The MRX sensitivity on magnetic NPs depends on the particle size distribution and the temperature at which the measurements are carried out. If the anisotropy constant (*K*) is fixed, each mean size corresponds to an optimal temperature where the highest sensitivity is achieved. Due to the unknown *K* value, series of simulations with different *K*'s were performed for a temperature range from -260°C to 200°C to find out the best sensitivity, as shown in Figure 3.18. The results show no significant difference in the best sensitivity with different anisotropy constants. From *K* = 50 kJ/m^3 to 10 kJ/m^3, it is increased by only 1.1 times and the sensitivity is no more than 4.5 pT/μg of Fe. There are

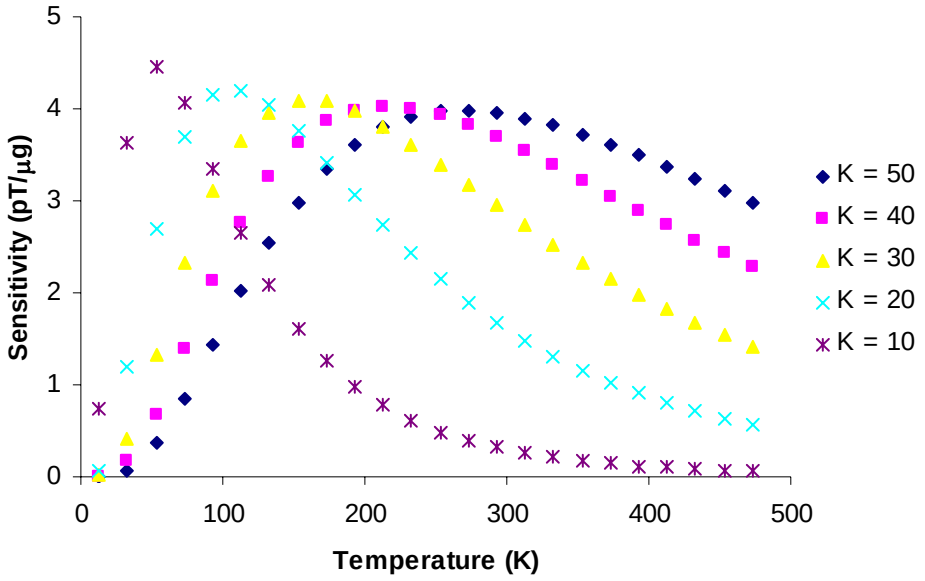

Figure 3.18 The simulated curves of sensitivity versus temperature with different anisotropy constant (*K*) values by assuming the magnetic properties of CC 1811. There exists an optimal temperature for any *K* value, where the sensitivity achieves maximum.

two facts worth mentioning about Figure 3.18. As the *K* value becomes smaller, the optimal temperature decreases, which is because to keep τ_N comparable to the measurement time scale, T has to be decreased to compensate the change in *K*. Another fact is that at the optimal temperature, the lower *K* value gives higher sensitivity. This can be explained by lowering the anisotropy constant, particles in a wider size range can have proper relaxivity time constant so that the signal is higher.

Besides the mean diameter, the standard deviation of the particle size distribution affects the MRX signal, because it determines what fraction of the NPs can be observed. Standard deviations in diameter from 0.5 to 3 nm were tested in the model and the results were plotted in Figure 3.19. As can be expected, the peak is higher and when the size distribution is narrower because a larger fraction of NPs can contribute to the signal at the optimal temperature. When the standard deviation is reduced to 0.5 nm, 6% relative

deviation to the mean size, which has been achieved by some NP synthesis techniques [18-20], the sensitivity at the optimal temperature is 21 pT/μg. By assuming the minimum determinable B_0 is ~ 1 pT in our SQUID-MRX system, the detection limit for the ideal sized NPs with 6% deviation in the diameter distribution can be 48 ng.

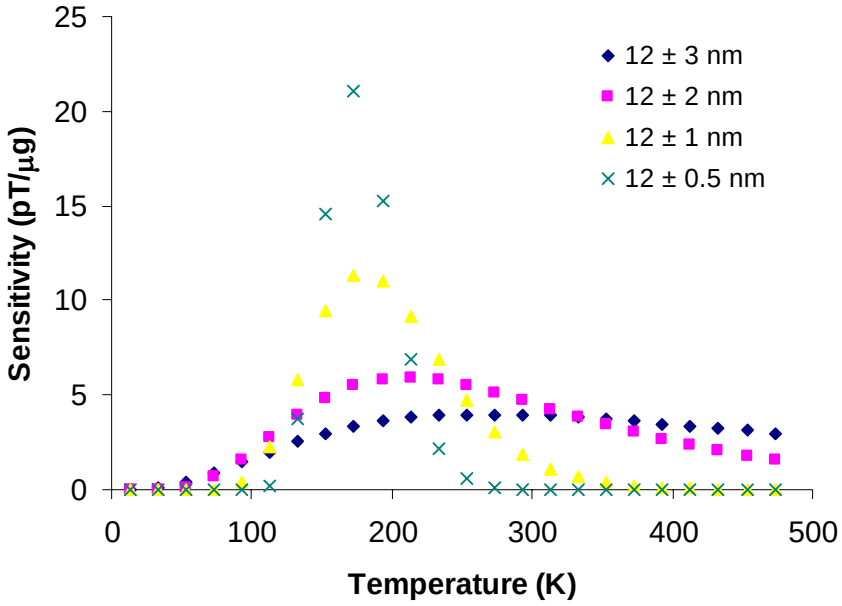

Figure 3.19 Simulations of the MRX sensitivity dependence on the standard deviation of NP's diameter with the magnetic properties of CC 1811. It shows a 5-fold increment on the best sensitivity at its optimal temperature when the standard deviation decreases from 3 nm to 0.5 nm.

To summarize, the close match of the experimental sensitivity and the theoretical values show that the SQUID-MRX system is working at its operational optimum. The small discrepancy between theory and measurement may come from the assumed anisotropy constant in the simulation has the highest sensitivity at room temperature while the real value does not. Without further reducing the electromagnetic noise, the only way to increase the detection limit is to acquire magnetic NPs which have a narrow

size distribution and the optimal MRX temperature around the room temperature. Our theory and measurement point to the optimum value being ~ 12 nm.

3.5 Reference

1. Heim, E., et al., *Fluxgate magnetorelaxometry of superparamagnetic nanoparticles for hydrogel characterization.* Journal Of Magnetism And Magnetic Materials, 2007. **311**(1): p. 150-154.

2. Ludwig, F., E. Heim, and M. Schilling, *Magnetorelaxometry of magnetic nanoparticles - a new method for the quantitative and specific analysis of biomolecules.* 2004 4th Ieee Conference On Nanotechnology, 2004: p. 245-248.

3. Ludwig, F., et al., *Magnetorelaxometry of magnetic nanoparticles in magnetically unshielded environment utilizing a differential fluxgate arrangement.* Review Of Scientific Instruments, 2005. **76**(10).

4. Chemla, Y.R., et al., *Ultrasensitive magnetic biosensor for homogeneous immunoassay.* Proceedings Of The National Academy Of Sciences Of The United States Of America, 2000. **97**(26): p. 14268-14272.

5. Eberbeck, D., et al., *Binding kinetics of magnetic nonoparticles on latex beads studied by magnetorelaxometry.* Applied Organometallic Chemistry, 2004. **18**(10): p. 542-547.

6. Kötitz, R., et al., *Biomagnetism: Fundamental Research and Clinical Applications*, ed. C. Baumgartner, L. Deecke, and S.J. Williamson. 1995, Amsterdam: Elsevier Science. 785.

7. Flynn, E.R. and H.C. Bryant, *A biomagnetic system for in vivo cancer imaging.* Physics In Medicine And Biology, 2005. **50**(6): p. 1273-1293.

8. Romanus, E., et al., *Determination of energy barrier distributions of magnetic nanoparticles by temperature dependent magnetorelaxometry.* Nanotechnology, 2003. **14**(12): p. 1251-1254.

9. Romanus, E., et al., *Energy barrier distributions of maghemite nanoparticles.* Nanotechnology, 2007. **18**(11): p. -.

10. Grover, F.W., *Inductance calculation, working formula and tables*. 1982: Dover publications. 286.

11. Chatternton, P.A. and M.A. Houlden, *EMC - Electromagnetic Theory to Practical Design*. 1992, Chicheser: Wiley.

12. Lammeraner, J. and M. Stafl, *Eddy Currents*. 1966, London: ILIFFE Books Ltd.

13. Chantrell, R.W., S.R. Hoon, and B.K. Tanner, *Time-Dependent Magnetization in Fine-Particle Ferromagnetic Systems.* Journal of Magnetism and Magnetic Materials, 1983. **38**(2): p. 133-141.

14. Grossman, H.L., et al., *Detection of bacteria in suspension by using a superconducting quantum interference device.* Proc. Natl. Acad. Sci. U. S. A., 2004. **101**(1): p. 129-134.

15. Shi, X.Y., et al., *Synthesis, characterization, and intracellular uptake of carboxyl-terminated poly(amidoamine) dendrimer-stabilized iron oxide nanoparticles.* Phys. Chem. Chem. Phys., 2007. **9**(42): p. 5712-5720.

16. Fannin, P.C. and S.W. Charles, *Measurement of the Neel Relaxation of Magnetic Particles in the Frequency-Range 1khz to 160mhz.* Journal of Physics D-Applied Physics, 1991. **24**(1): p. 76-77.

17. Fannin, P.C. and S.W. Charles, *On the Calculation of the Neel Relaxation-Time in Uniaxial Single-Domain Ferromagnetic Particles.* Journal of Physics D-Applied Physics, 1994. **27**(2): p. 185-188.

18. Yu, W.W., et al., *Synthesis of monodisperse iron oxide nanocrystals by thermal decomposition of iron carboxylate salts.* Chemical Communications, 2004(20): p. 2306-2307.

19. Jana, N.R., Y.F. Chen, and X.G. Peng, *Size- and shape-controlled magnetic (Cr, Mn, Fe, Co, Ni) oxide nanocrystals via a simple and general approach.* Chemistry of Materials, 2004. **16**(20): p. 3931-3935.

20. Sun, S.H. and H. Zeng, *Size-controlled synthesis of magnetite nanoparticies.* J. Am. Chem. Soc., 2002. **124**(28): p. 8204-8205.

CHAPTER 4

Hydrothermal Synthesis of Fe_3O_4 Nanoparticles and the *In Vitro* Study with SQUID Magnetorelaxometry

4.1 Introduction

Due to the particle size sensitivity of the SQUID magnetorelaxometry (MRX) method, controlled synthesis of magnetic nanoparticles (NPs) is necessary for applications using this technique. In our group, monodisperse functionalized Fe_3O_4 NPs were already achieved and both in vitro and in vivo applications were successful.[1-4] However, these particles have too small sizes (5 nm and 8 nm in diameter) for the SQUID-MRX measurement and their synthetic routes do not allow the proper size to be made. Meanwhile, the commercially acquired NPs have excellent detection sensitivity with MRX, but these particles are pre-coated with certain kinds of surfactants and not adaptable with our functionalization scheme. For example, the NPs from Chemicell have starch coating layers and those from the Meito Sangyo Co. are encapsulated with dextran. In order to make proper magnetic nanoparticles both for the MRX measurement and with modifiable surface for folic acid (FA) attachment, I developed a hydrothermal synthetic method for Fe_3O_4 NPs with the ability producing variable size, and thus tunable magnetic properties.

There are several factors making colloidal iron oxide NPs advantageous for biological applications. They have excellent magnetic properties with typical saturation magnetization in the range of 30-50 emu/g.[5] Therefore they can generate sufficient contrast in low doses.[6, 7] In clinical MRI, the commonly used dose of iron oxide NPs is 1 mg iron per kg of tissue weight, which is small to the naturally occurring amount of iron (3500 mg) in human body.[8, 9] Some metallic NPs, including iron, cobalt, nickel and their alloys, are also attractive because they have similar or even stronger ferromagnetic properties. But their chemical instability induces cytotoxicity and susceptibility to oxidation so that robust protection, such as gold and silica, is required, which complicates the synthetic process.[10-13] Also it has been demonstrated that amorphous coatings cannot protect the metallic core from oxidation.[14] Furthermore, iron oxide NPs are the only inorganic particulate contrast agents for in vivo human applications now in Phase-III trials.[15-17]

Commonly employed chemical methods of iron oxide NPs synthesis can be divided into two main categories: 1) coprecipitation of Fe (II) and Fe (III) ions in a basic aqueous solution [2, 18-20] and 2) thermal decomposition of iron organometallic compounds in organic solvent.[21, 22] Acqueous coprecipitation is a conventional, facile way to prepare colloidal iron oxide NPs.[23] It is easy to scale up to large amounts [24] and no phase transfer needs to be performed to make them water soluble.[3, 4] But this method generates iron oxide NPs with a fixed mean diameter, lacking the ability to control the particle size. Also the materials obtained with this method can be poorly crystalline and are polydisperse in many cases.[25, 26] The organic approaches of iron oxide NPs preparation have been recently developed [22, 27-30], mostly inspired by the

success of nonacqueous synthesis of high-quality semiconductor nanocrystal.[31, 32] Iron organometallic compounds, such as $Fe(CO)_5$ [21], or Fe(III) acetylacetonate [$Fe(acac)_3$] [22], are used as precursors to form a solution with oleic acid, trimethylamine oxide, octyl ether or other kinds of combinations [21] of organic solvents. Then the mixture undergoes a high temperature (~ 300°C) decomposition procedure to produce the iron oxide NPs. The synthesized NPs are monodisperse in size and the diameter can be varied from a few nanometers to about 15 nm in a single step.[33] Further growth of the NPs needs to be done from seed-mediated reactions using the prepared NPs and allowing the diameter to be tuned up to 20 nm, with each new growth reaction increasing the diameter by ~ 2 nm.[34] This approach involves toxic organic reagents, multiple reaction steps, and high reaction temperature. Moreover, phase transfer of the NPs to aqueous solution is necessary when these particles are used for biological applications.[1, 35]

In this chapter, a simple, facile hydrothermal approach was developed to synthesize Fe_3O_4 NPs. The size of the formed Fe_3O_4 NPs can be tuned through variation of the reaction conditions. Accordingly the magnetic properties of the synthesized Fe_3O_4 NPs can be varied. These NPs were investigated using the SQUID-MRX technique and the results clearly reveal that the particle size can significantly affect the MRX sensitivity. Functionalization of the synthesized NPs was performed through layer-by-layer (LbL) assembly with polystyrene sulfonate sodium salt (PSS), folic acid (FA)- and fluorescein isothiocyanate (FI)-modified poly(amidoamine) (PAMAM) dendrimers of generation 5 ($G5.NH_2$-FI-FA). The fluorescence moiety was added as an additional signal reporter. The in vitro experiments were characterized by flow cytometry, inductively coupled plasma – mass spectroscopy (ICP-MS) and MRX, and results were compared.

4.2 Methods

4.2.1 Materials

All chemicals used were reagent grade from commercial sources. $FeCl_2 \cdot 4H_2O$ (99%) and ammonia (28%) were purchased from Aldrich. Ethanol was obtained from AAPER Alcohol & Chemistry Co. Water used in all experiments was purified using a Milli-Q Plus 185 water purification system (Millipore, Bedford, MA) with resistivity higher than 18 MΩ·cm.

4.2.2 Synthesis of Fe_3O_4 NPs

In a typical synthesis (e.g., product 1 in Table 4. 1), $FeCl_2 \cdot 4H_2O$ (0.5 g) was dissolved in 25 mL water. Under vigorous stirring, ammonium hydroxide (2.5 mL) was added and the suspension has continuously stirred in air for 10 min, allowing the iron (II) to be oxidized. The reaction mixture was then autoclaved (Tuttnauer 2540M Analog Autoclave, Krackeler Scientific, Inc, Albany, NY) in a sealed pressure vessel with a volume of 48 mL at 134˚C for 3 h and cooled to room temperature. The black precipitate was collected and purified with water via a centrifugation-dispersion process. The final Fe_3O_4 NP suspension was lyophilized to obtain black dry powder.

4.2.3 Fabrication of Multifunctional Dendrimer Coated Fe_3O_4 NPs

The functionalization of the synthesized NPs followed the reported protocol achieved by Shi in our group.[2] A suspension of Fe_3O_4 NPs (5 mg in 0.5 mL water) was mixed and shaken with 1 mL of PSS (polystyrene sulfonate sodium salt) solution, which has concentration of 2mg/mL and contains 0.5 M NaCl. After 20 min of the PSS adsorption, the mixture was centrifuged at 7000 for 10 min. The precipitated NPs were

water washed and centrifuged for three cycles. Then 1 mL of G5.NH_2-FI-FA solution (1 mg/mL with 0.5 M NaCl) was added, shaken and purified in the same way.

A following acetylation reaction is necessary to neutralize the NP's surface charge caused by the remaining amine groups on G5.NH_2-FI-FA dendrimers. The Fe_3O_4/PSS/G5.NH_2-FI-FA NPs in 1 mL water were added with triethylamine (2.5 μL) and methanol solution containing 18.2 mg/mL acetic anhydride in 1.7 μL. The mixture was shaken for 24 hrs and purified with water through centrifugation-redispersion procedure for 4 times. The control group Fe_3O_4/PSS/G5.NHAc-FI, in comparison to Fe_3O_4/PSS/G5.NHAc-FI-FA, was prepared in the same manner without FA conjugation. The iron concentration of the NP suspension was determined by the ICP-MS method, which are 5.16 mg/mL for Fe_3O_4/PSS/G5.NHAc-FI and 5.44 mg/mL for Fe_3O_4/PSS/G5.NHAc-FI-FA.

4.2.4 Cell Culture

Human epithelial cancer cells (ATCC, Manassas, Virginia, USA), which are known as KB cells and overexpress FARs, were used in the *in vitro* experiments. The cells grown in FA-free medium will express high-levels of FAR, while the cells grown in FA-rich media will express low-level FAR. The KB cells were maintained at 37°C and 5% CO_2 in RPMI 1640 medium supplemented with 10% heat-inactivated fetal bovine serum (FBS) and 100 units/mL penicillin and 100 μg/mL of streptomycin. To study the targeting capabilities of the dendrimer-coated magnetic nanoparticles, the cells were seeded in tissue culture flasks. After the incubation, cells were trypsinized with 0.25% trypsin-EDTA and centrifuged at 2000 rpm for 5 min. The resulting cell pellets were then resuspended in PBS. Two washes with phosphate-buffered saline (PBS) were performed

and the cells were centrifuged as above. The PBS was aspirated from the cells and they were washed with PBS three times. Samples prepared for the SQUID measurement contained 8.8×10^7 cells in a total volume of 350 μL. Cells for the flow cytometry and ICP-MS studies were taken out from the same incubation and will be discussed in the following sections. As a control, a group of KB-cells were incubated in the presence of 100 μM free FA to block the FARs on the cell surfaces.

4.2.5 Transmission Electron Microscopy (TEM)

TEM experiments were performed either on a Philips CM-100 microscope operating at 60 kV or on a JEOl 2010F analytical electron microscope operating at 200 kV. The former TEM was equipped with a Hamamatsu digital Camera ORCA-HR and operated using AMT software (Advanced Microscopy Techniques Corp, Danver, MA) for the study of the NP morphology. The latter TEM was used to analyze the selected area electron diffraction (SAED) of the NPs. TEM samples were prepared by placing one drop of diluted iron oxide suspension (5 μL) onto a 200-mesh carbon-coated copper grids and air-dried before measurements.

4.2.6 X-ray Diffraction (XRD)

The crystalline structure and the size of the products were determined by a Scintag powder XRD system using Cu Kα radiation with a wavelength of 1.5404 Å at 40 kV and 30 mA. First, a coarse scan from 20° to 70° (2θ) was performed to acquire an overall spectrum to identify the crystal structure. Then, a finer scan of the major peak was repeated to produce a smoother peak for better estimating the size of NPs.

4.2.7 X-ray Photoelectron Spectroscopy (XPS)

XPS was performed using a Kratos Ultra DLD XPS operated at 15 kV using a monochromated Al source that can give an energy resolution of ~ 0.5 eV. Both broad and narrow (or core) scans were carried out to collect XPS spectra.

4.2.8 SQUID magnetometry

The magnetic hysteresis loops were measured using a Quantum Design MPMS-5 SQUID magnetometer (San Diego, CA) at room temperature. The Fe_3O_4 NP powder was loaded into a plastic capsule and the capsule was put into a plastic straw before measurement.

4.2.9 SQUID magnetorelaxometry (SQUID-MRX)

The system setup and experimental parameters are the same as chapter 3, section 3.3. Briefly, hardware screenings including the *rf* shield and the mu-mteal shield were utilized to reduce noise. Magnetic biasing field of 15 G was applied for a time period of 1 s. The time delay between the turn-off of field and beginning of data taking was 15 ms and data were recorded for 1 s. Each measurement was an average of 10 trials and 5 measurements were made for each sample.

To quantitatively relate the amount of the NPs with the SQUID signal, equation (3-5) was applied to fit the decay curve. The fitting parameter - decay amplitude B_0 was used to characterize the NPs' mass.

4.2.10 Flow Cytometry

Flow cytometry was conducted to detect the fluorescent signals from the fluorescein present on the surface of the NPs. The measuring system is composed of a

Beckman-Coulter EPICS-XL MCL flow cytometer and Expo32 software (Beckman-Coulter, Miami, Florida) for data analysis. An aliquot of the cells (1.76×10^6) prepared for the SQUID was taken out, mixed with an additional 1.5 mL PBS and used for the flow cytometry measurement.

4.2.11 Inductively Coupled Plasma-Mass Spectroscopy (ICP-MS)

Iron concentrations in this study were all measured by using a ThermoFisher Finnegan Element inductively coupled high-resolution mass spectrometer. To ionize the Fe element from the NPs or cells, aqua regia was made in the volume ratio of 3:1 HCl to HNO_3. Due to the detection range of the ICP-MS method, the dissolved solution must be diluted to a proper concentration. For the cell culture, 100 μL of cells was dissolved and diluted to 1 mL by the acid and high purity water. The solution was further diluted by a factor of 20. The unstained cells were diluted only by two.

4.3 Results and Discussion

4.3.1 Characterization of Fe_3O_4 NPs

A typical TEM image of the as-synthesized Fe_3O_4 NPs (product 1 listed in Table 4. 1) is shown in Figure 4.1a. In the image, the NPs exhibit spherical or slightly ellipsoidal shape. Statistical analysis of the size of the particles (Figure 4.1b) shows that the average diameter of the NPs is 31.1 ± 6.1 nm, indicating that the NPs are uniform when compared with other Fe_3O_4 NPs synthesized in aqueous conditions.[36-38] The selected area electron diffraction (SAED) pattern of the same Fe_3O_4 NPs (Figure 4.1c) confirmed a typical magnetite crystalline structure.[25, 39]

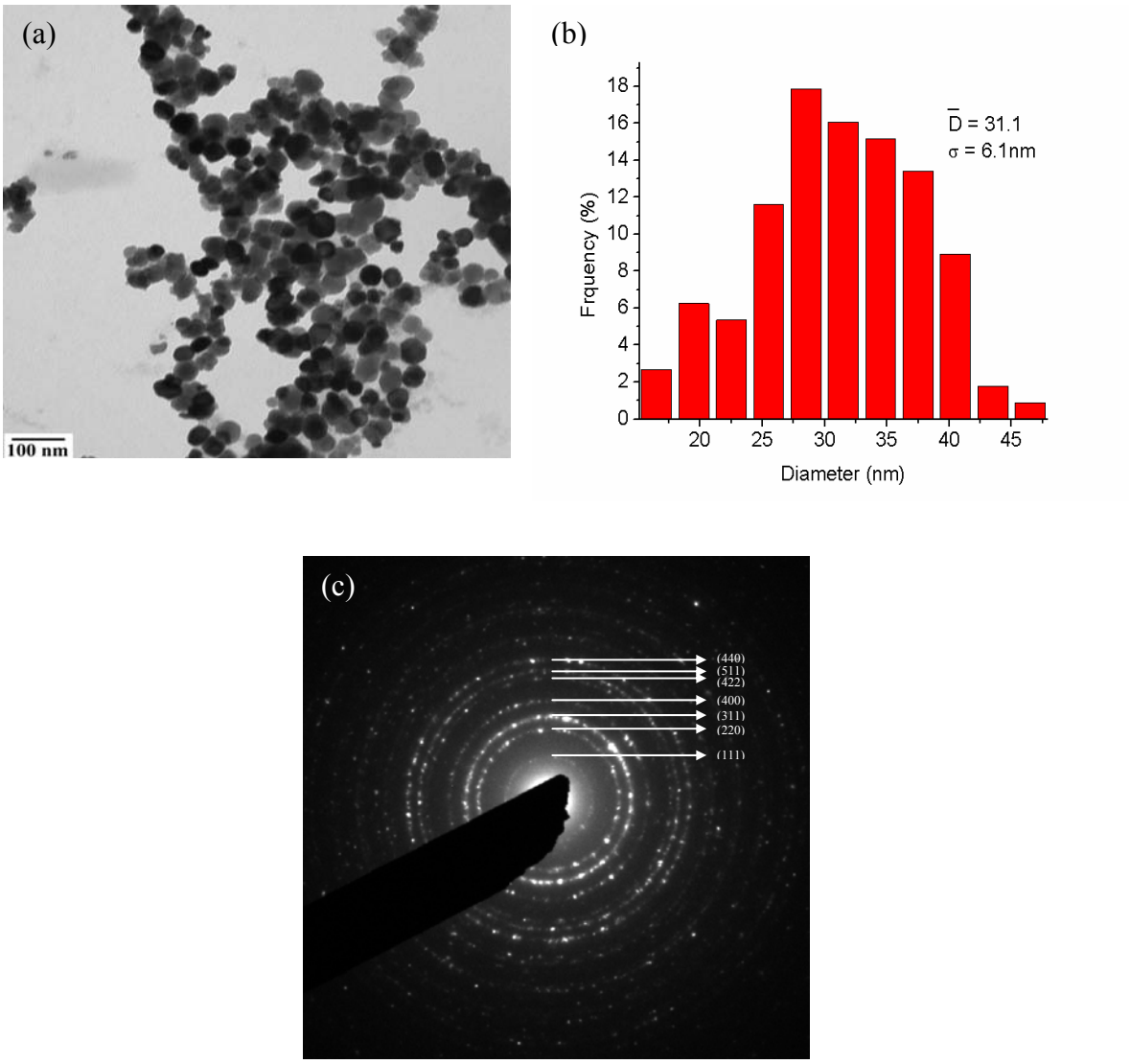

Figure 4.1 (a) A typical TEM image, (b) size distribution histogram, and (c) selected area electron diffraction (SEAD) pattern of Fe_3O_4 NPs (Product 1 listed in Table 4. 1)

The composition of these nanocrystals was identified by XPS (Figure 4.2). The survey scan shows clear peaks corresponding to the binding energies of Fe_{2p} and O_{1s} (Figure 4.2, left panel). Further fine scanning around the Fe_{2p} peaks reveals two characteristic binding energy peaks at 710.4 and 723.3 eV for $Fe_{2p3/2}$ and $Fe_{2p1/2}$, respectively, which are consistent with the reported values of Fe_3O_4 in the handbook

(Figure 4.2, right panel).[40, 41] Other peaks in the spectrum (Figure 4.2, left panel) are ascribed to the indium substrate and carbon contamination on the substrate.

Table 4. 1 Fe_3O_4 NPs with tunable sizes synthesized under different reaction conditions.

Pruduct	$FeCl_2 \cdot 4H_2O$ (g)	Solvent		$NH_3 \cdot H_2O$ (mL)	Total volume (mL)	Diameter [a] (nm)	Diameter[b] (nm)
		H_2O (mL)	Ethanol (mL)				
1	0.25	12.75	0	1.25	14	31.1 ± 6.1	29.7
2	0.5	11.5	0	2.5	14	22.4 ± 4.1	22.5
3	1	9	0	5	14	16.7 ± 3.3	17.3
4	1.25	7.75	0	6.25	14	15.4 ± 2.4	16.0
5	0.25	6.375	6.375	1.25	14	19.9 ± 3.9	20.3

[a] Measured by TEM. [b] Measured by XRD.

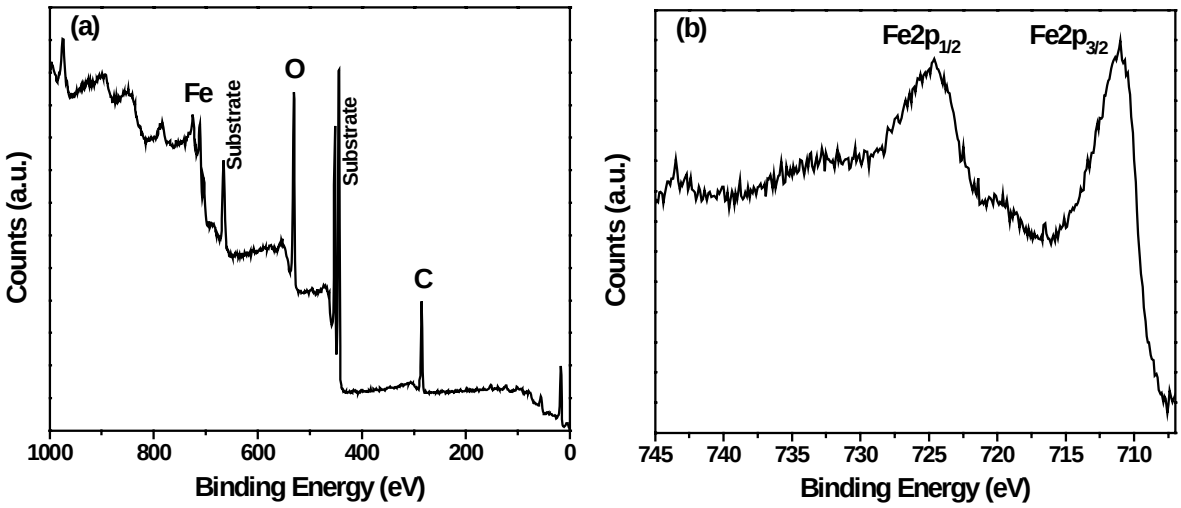

Figure 4.2 (a) XPS survey of the as-synthesized Fe_3O_4 NPs and (b) Fe2p core-level spectrum of the same NPs (Product 1 listed in Table 4. 1)

4.3.2 Size-control of the Fe_3O_4 NPs

After the Fe_3O_4 NPs with a diameter of 31 nm were synthesized and characterized, we expected that by altering the reaction conditions, the size of Fe_3O_4 NPs could be controlled. To test the influence of $FeCl_2$ concentration on the as-synthesized NP size, our experiments were designed to minimize the change of other parameters. First, we kept a constant volume of the mixture solution (14 mL) in the pressure glass vessel to ensure that a similar amount of oxygen was used for the oxidation of Fe (II). And the volume of ammonium was adjusted proportional to the amount of $FeCl_2$. A series of changes on the experimental parameters with their corresponding products are shown in Table 4. 1.

From product 1 to 4, as the concentration of $FeCl_2$ increases, the synthesized NPs get smaller. The TEM images (Figure 4.3a-c) with the same magnification as figure 1a obviously show the monotonic size change. Size distributions were evaluated by randomly measuring 300 NPs in the images, also listed in Table 4. 1. With the amount of $FeCl_2 \cdot 4H_2O$ increasing from 0.25 to 1.25 g, the size of the synthesized NPs decreases from 31.1 to 15.4 nm. This could be due to the fact that the concentration of Fe (II) ions strongly affects the nucleation and growth rate of Fe_3O_4 particles. The higher initial precursor concentration led to smaller particles size due to the formation of a large number of seed nuclei, which provided high particle concentration and yielded smaller particles.[37, 42]

Another important factor affecting the size of the synthesized Fe_3O_4 NPs is the composition of the solvent. For product 5, we replaced half the volume of water used for product 1 preparation (6.375 mL) with ethanol, while keeping all other parameters

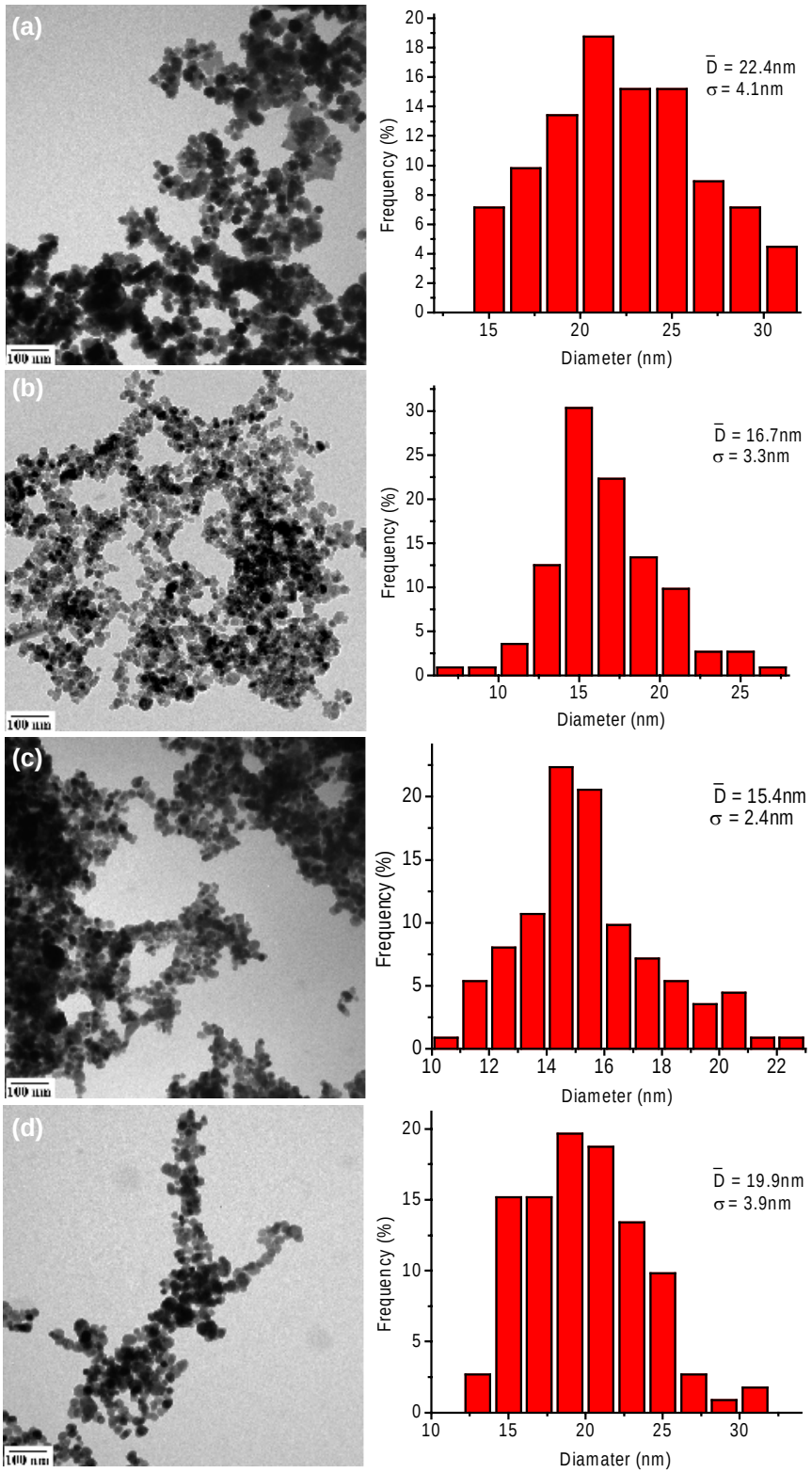

Figure 4.3 TEM images of Fe_3O_4 NPs as the concentration of $FeCl_2$ increasing and the corresponding statistical histograms. Mean diameters are (a) 22.4nm (b) 16.7nm (c) 15.4nm. Same condition as the NPs in Figure1 except that ethanol and water mixture was used as solvent (d) mean diameter 19.9nm

unchanged. The resulting NPs have a significant size decrease (from 31.1 nm for product 1 to 19.9 nm for product 5), as can be seen from the TEM image and size distribution histogram in Figure 4.3d. Similar effects have been reported previously.[41, 43] The reason for this could be due to the fact that the formed Fe_3O_4 NPs with considerable numbers of hydroxyl groups on the surface can absorb ethanol via hydrogen bond formation. Accordingly, there were more ethanol molecules attached on the NP surfaces, which inhibited the subsequent growth and aggregation of the particles, leading to the formation of smaller particles.

To further confirm the crystal structure and the size of the formed Fe_3O_4 NPs under different conditions, XRD experiments were performed (Figure 4.4). Curves

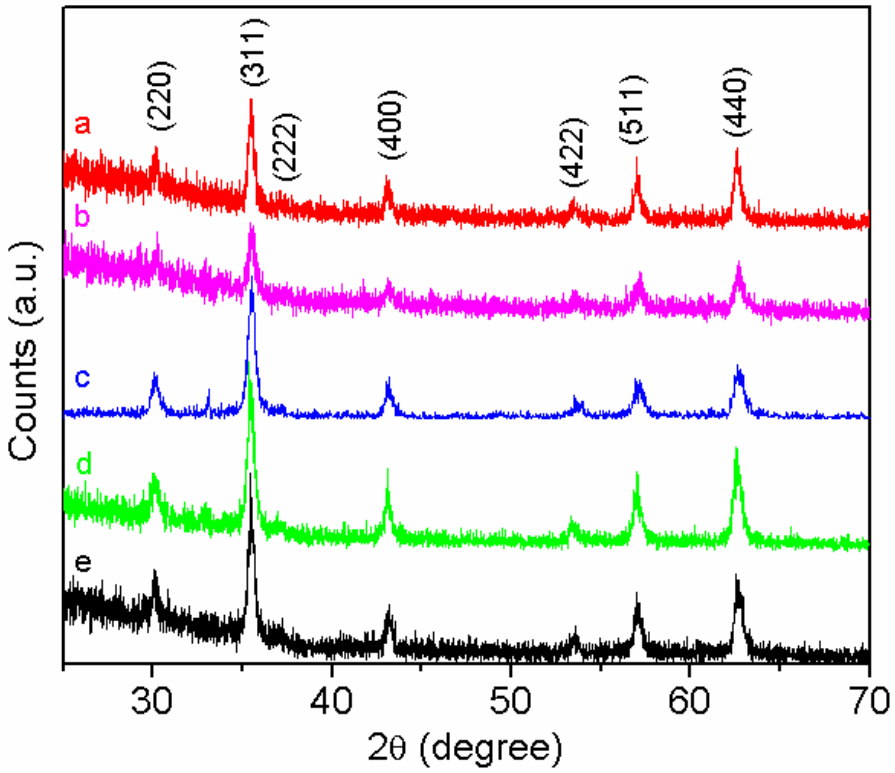

Figure 4.4 XRD patterns of (a) product 1 (29.7 nm), (b) product 2 (22.5 nm), (c) product 3 (17.3 nm), (d) product 4 (16.0 nm), and (e) product 5 (20.3 nm) (see Table 4. 1). The diameter of each product is calculated based on Scherrer's equation

labeled from (a) to (e) correspond to product 1 to 5, respectively. The lattice spacing calculated from the diffraction peaks observed at 30, 35.4, 37.2, 43, 53.4, 56.9, and 62.5 matched the [220], [311], [222], [400], [422], [511], and [440] planes of Fe_3O_4 crystals, respectively. The XRD patterns are consistent with those reported in literature.[34, 44, 45]

The comparison of curve (e) with the other four curves suggests that the use of water/ethanol mixture as solvent does not have any appreciable effect on the crystal structure of the NPs when compared to those NPs formed in pure water. To obtain the average size of the Fe_3O_4 NPs, we did fine scans on the major peak (plane [311]) of each product and calculated their sizes using Scherrer's equation. The particle diameter D can be calculated by [46]

$$D = \frac{0.9\lambda}{\beta \cos\theta} \tag{4-1}$$

where λ is the wavelength of x-ray in nanometers and β is the full width at the half maximum (FWHM) in terms of the Brag angle θ in radians. The results (Table 4. 1) are in very good agreement with TEM data. It can be further concluded that the synthesized Fe_3O_4 NPs are nearly single crystals.

4.3.3 Magnetic Properties of the Fe_3O_4 NPs

The magnetic hysteresis loops of room temperature Fe_3O_4 NPs were obtained by a DC SQUID magnetometer (Figure 4.5). For the largest NPs (product 1 with mean diameter of 31.1 nm), the specific saturation magnetization (σ_s) is 97.4 emu/g, which is close to the bulk magnetite.[47] As the size of the Fe_3O_4 NPs is reduced to 22.4, 16.7, and 15.4 nm, σ_s decreases to 81.2, 65.1 and 53.3 emu/g, respectively. This phenomenon was

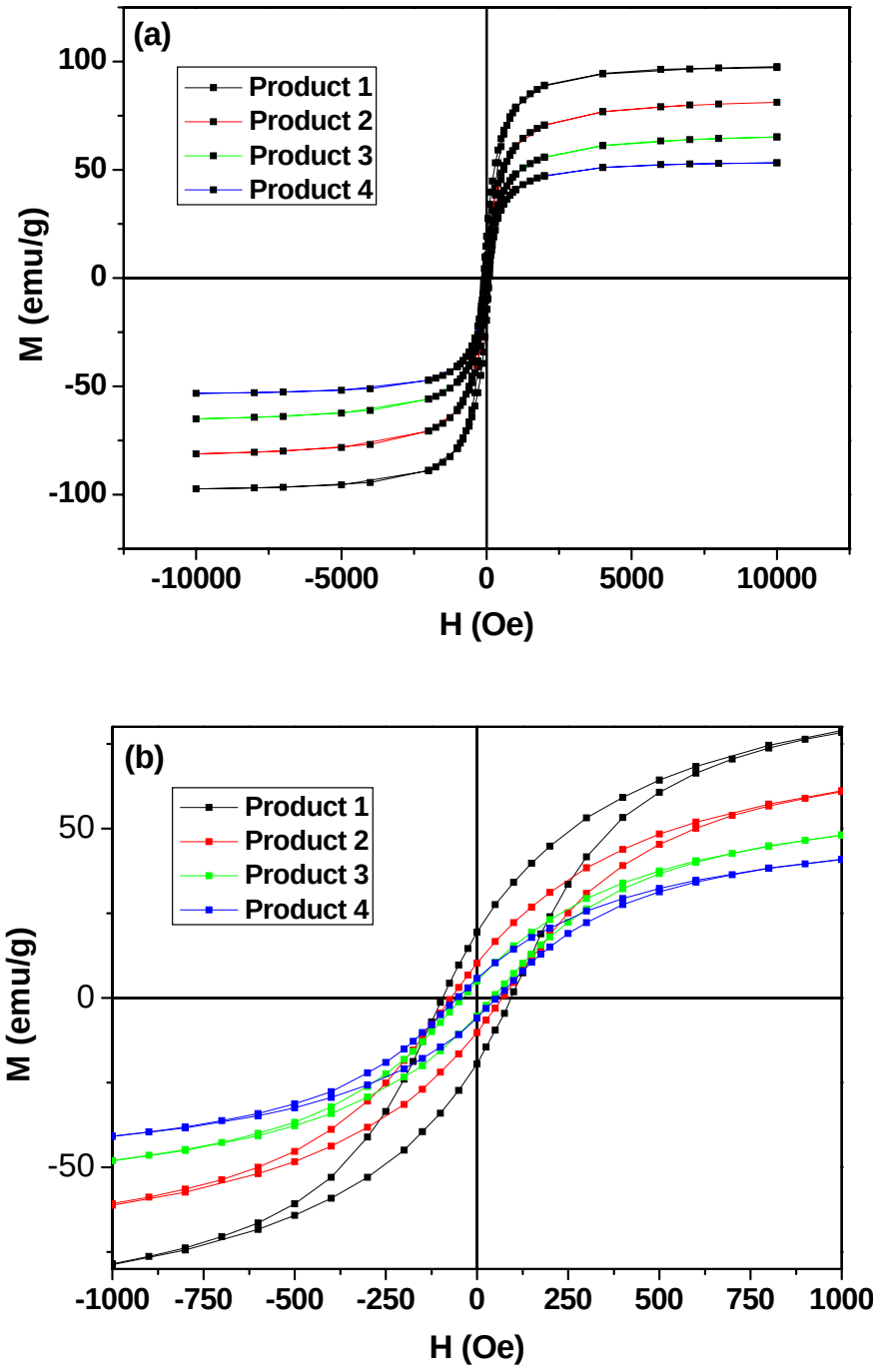

Figure 4.5 SQUID magnetometry measurement of room-temperature magnetic hysteresis of NP Products 1-4: (a) full hysteresis loops, and (b) hysteresis at low field

observed in many other magnetic NPs and could be explained by the existence of a magnetically inert layer on the surface of the particles.[48] Due to this surface effect, σ_s is contributed by an effective volume, which is a fraction of the nominal volume. As the

particle gets smaller, the magnetic effective volume accounts for smaller proportion and the specific saturation magnetization decreases.

Figure 4.6 displays the profile of σ_s as a function of the inverse of the particle mean diameter. The data points were fitted linearly. A theoretical approach to quantitatively explain this linear relationship assumes that each nanocrystal consists of two parts: the nonmagnetic outer layer with thickness *t* and magnetic normal core with same property as bulk material. By keeping the first order in *t*, the specific saturation magnetization is found to be proportional to the inverse of diameter.

$$\sigma_s(d) = \left(1 - \frac{6t}{d}\right)\sigma_s(\infty) \tag{4-2}$$

The nonmagnetic layer on the surface of the Fe_3O_4 NPs can be calculated, and is found to be about 1.4 nm.

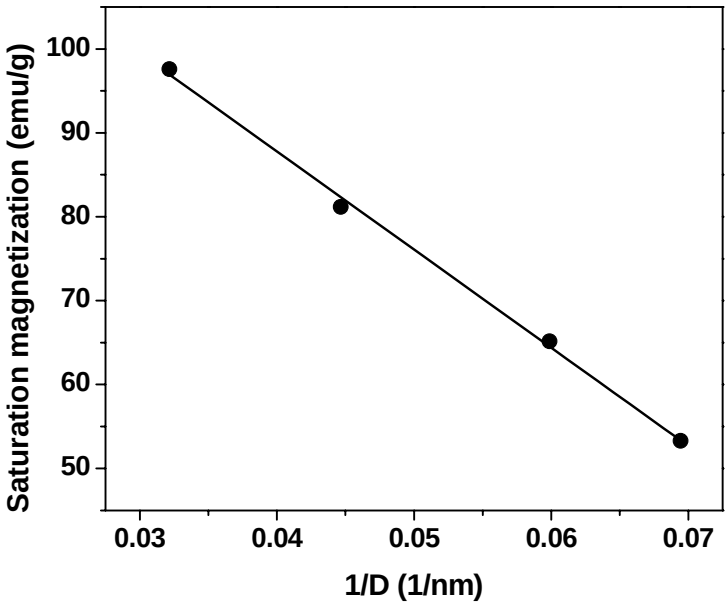

Figure 4.6 The saturation magnetization (σ_s) decreases as the diameter of the Fe_3O_4 NPs increases due to the nonmagnetic surface effect

As can be seen from Figure 4.5b, in the particle size range of our synthesized products (from 31.1 to 15.4 nm) ferromagnetism was observed. But as the mean size decreases, the coercivity (H_c) also decreases to values smaller than the reported for ferromagnetic bulk material.[47] This suggests a gradual transition from ferromagnetism to superparamagnetism as a function of the size of the magnetic NPs. This transition meets the requirements for using these NPs as contrast agent in the SQUID-MRX measurement. Due to the millisecond time delay between the biasing field turning off and measurements starting, NPs that are far in the region of superparamagnetism decay too rapid to be detected. On the other hand, particles that are large can not generate detectable decay signal during the measurement time course and will also be ignored. So only the NPs on the magnetic properties transition region with the appropriate relaxivity rate provide signal contribution, and thus preferred by the MRX technique.

4.3.4 SQUID-MRX Results

Figure 4.7 shows a typical relaxation curve recorded by the SQUID MRX system with the theoretical fitting for 200 μg NPs of product 4 (15.4 nm in diameter). The "no sample" curve in figure 7 was acquired in the absence of the Fe_3O_4 NPs after the background was subtracted. By applying Equation (3-5) to fit the experimental curve in the presence of NPs, the best-fit parameters B' and B_0 can be determined to be 87.9 and 20.5 pT, respectively. Similar as section 3.3.2, the value of B' can be ignored because it represents an arbitrary static magnetic field and B_0 is only affected by the mass of NPs as long as the SQUID measuring parameters do not change.

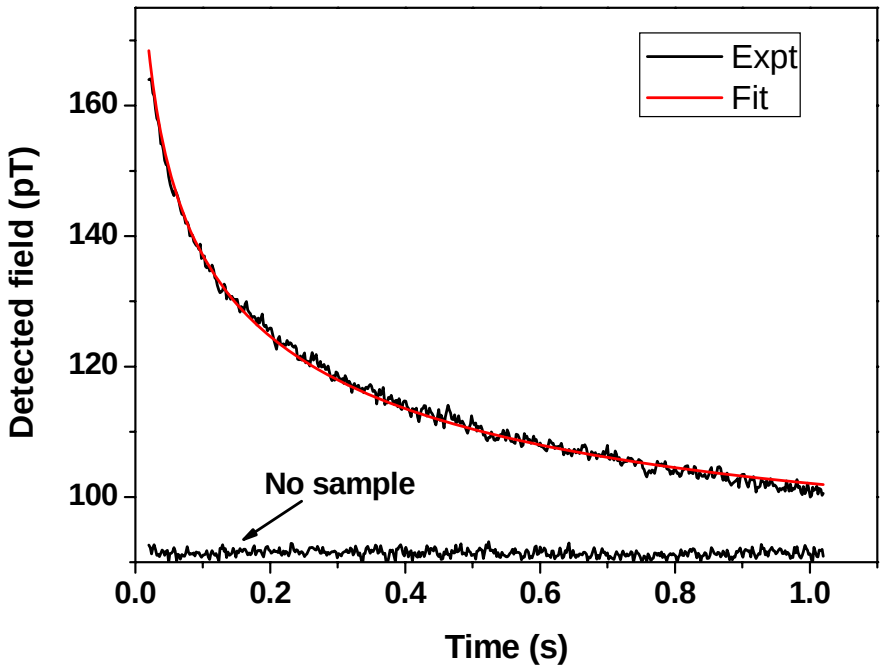

Figure 4.7 A SQUID magnetorelaxometry curve on 200 μg NPs of product 4 (D = 15.4 nm in average) with theoretical fitting $B(t) = B_0 \ln(1+1/t) + B'$, where B_0 = 2.05 pT and B' = 8.79 pT. The factor B_0 is proportional to the amount of NPs as shown in Figure 8

As discussed in section 4.3.3, when the average size of the iron oxide magnetic NPs is decreased from 31.1 to 15.4 nm, the magnetic behavior changes from ferromagnetic to superparamagnetic. This transition affects the particles' relaxation time constant, which in turn increases the MRX signal intensity. To test this, various amounts (from 20 to 200 μg) of the iron oxide NPs from products 1 to 4 were measured by SQUID-MRX and the decay amplitudes versus their masses are plotted in Figure 4.8. Each calibration line was fitted linearly and the sensitivities were found to be increasing when the particles get smaller. Figure 4.9 illustrates the sensitivity's dependence on the particles' mean diameter, showing a signal enhancement of three folds as the diameter changing from 31.1 to 15.4nm. The size dependence of MRX signal can be understood by considering the Nèel relaxation's relation to particle size, which predicts larger NPs have longer magnetic decay time. When the decay time is long enough that no obvious

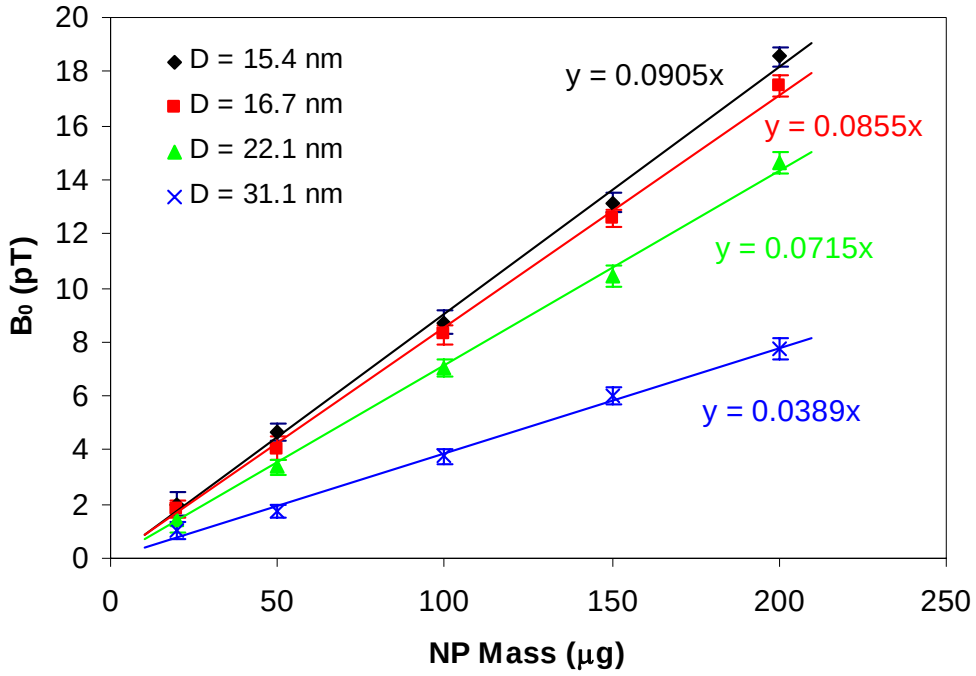

Figure 4.8 MRX sensitivities on NPs of product 1-4 with different mean diameters. The graph shows higher slope, i.e. sensitivity, for smaller NPs.

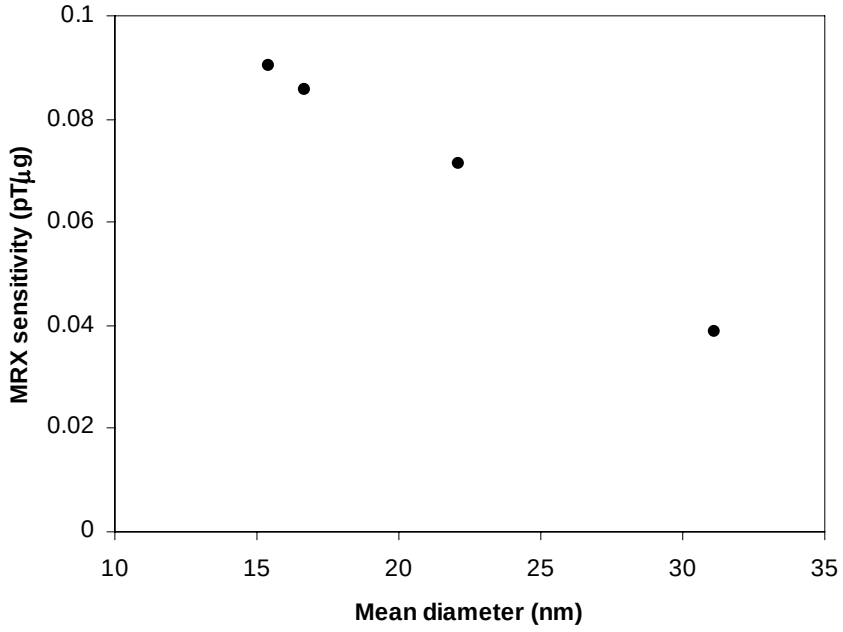

Figure 4.9 The dependence of the MRX sensitivity on the mean size of Fe_3O_4 NPs

decay can be observed during the MRX measurement time interval (in our case, 1 s), such particles have no contribution to the measurement. As the average size decreases, larger portion of NPs will have the decay time less than or equal to 1 s, thus increasing the MRX signal. And this behavior can be supported by the magnetic property transition from ferromagnetism to superparamagnetism (Figure 4.5).

4.3.5 *In Vitro* Experiments with SQUID-MRX Measurement

Since NPs in product 4 (d = 15.4 nm in average) have the highest MRX sensitivity, they were chosen to be functionalized by the FA and FI surface-modified G5 dendrimer, where the dye FI was used as the imaging molecule for flow cytometry. Meanwhile, the iron content was directly measured by ICP-MS to compare with the mass of particles calculated from the SQUID magnetic relaxation measurement. Three groups were designed in the study: 1) dendrimer functionalized Fe_3O_4 NPs with FA (Fe_3O_4/PSS/G5.NHAc-FI-FA) targeting KB cells expressing high-levels of FAR (KB-HFAR), 2) the ligand control group: non-targeted dendrimer coated Fe_3O_4 NPs without FA (Fe_3O_4/PSS/G5.NHAc-FI) for KB-HFAR, and 3) the receptor control group: KB cells with low-level FAR (KB-LFAR) targeted by Fe_3O_4/PSS/G5.NHAc-FI-FA. Figure 4.10 illustrates the binding differences among the three groups investigated by flow cytometry at various concentration of iron (0.07 to 0.56 mg/mL). There is a clear increase of the fluorescence signal from the Fe_3O_4/PSS/G5.NHAc-FI-FA with KB-HFAR compared the other two control groups. The two controls, i.e. no active targeting moiety (FA) on the contrast agents and blocked FAR of the KB cells, show similar fluorescence intensity. This indicates that the binding of PSS/G5.NH.Ac-FI-coated Fe_3O_4 NPs is mediated by the FA-FAR interactions. It should be noted that in the studied concentration range, the

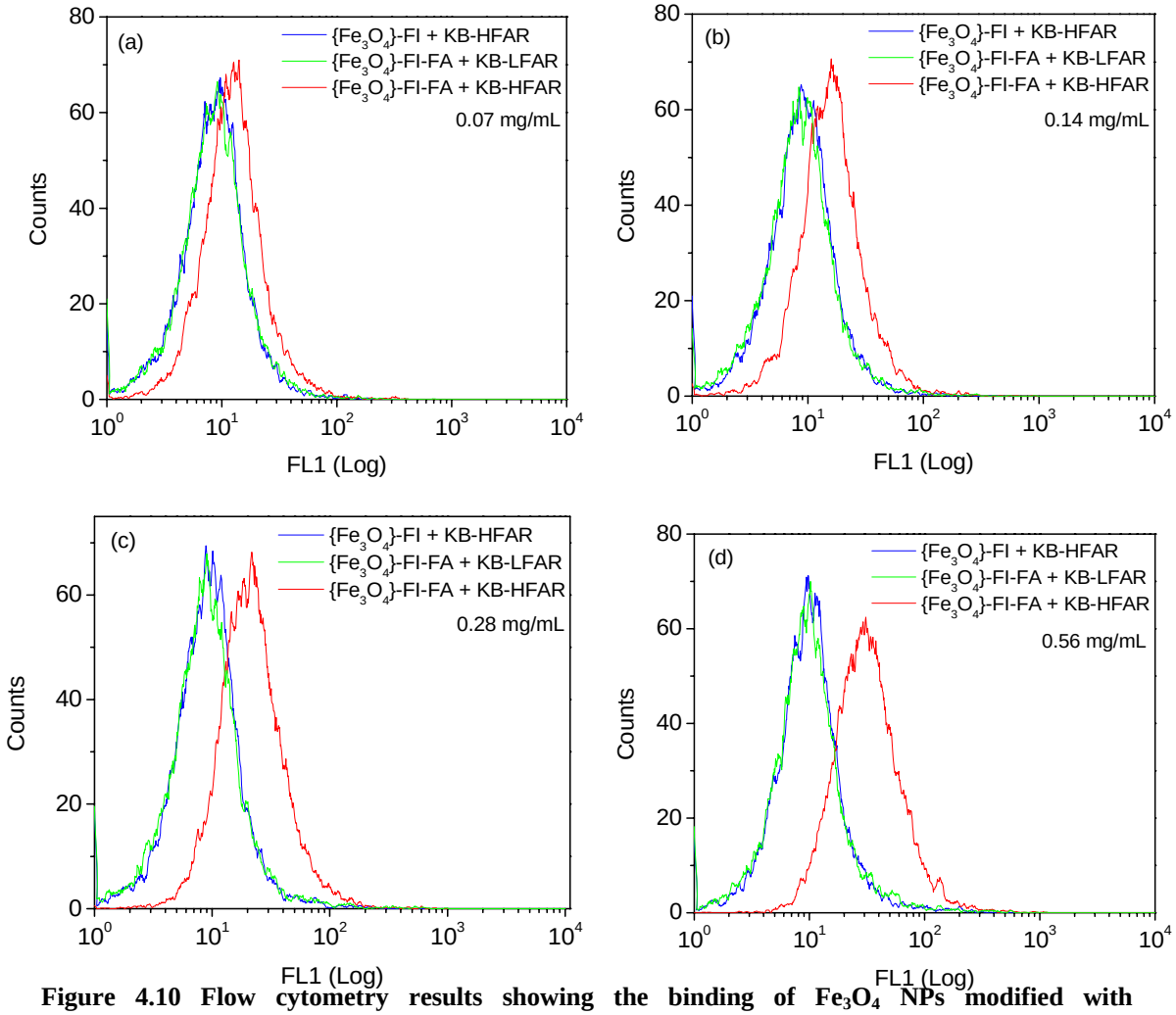

Figure 4.10 Flow cytometry results showing the binding of Fe_3O_4 NPs modified with PSS/G5.NHAc-FI and PSS/G5.NHAc-FI-FA with KB-HFAR and KB-LFAR at different concentrations. Iron concentrations are a) 0.07 mg/mL b) 0.14 mg/mL c) 0.28 mg/mL and d) 0.56 mg/mL.

fluorescence signal of Fe_3O_4/PSS/G5.NHAc-FI-FA targeted KB-HFAR is increased with the higher amount of NPs used.

The SQUID-MRX results are displayed in Figure 4.11, where the fitting parameter B_0, which represents the amount of NPs, is plotted against the experimental groups. In each subgroup, three cases can be compared: Fe_3O_4/PSS/G5.NHAc-FI-FA with KB-HFAR, Fe_3O_4/PSS/G5.NHAc-FI with KB-HFAR and Fe_3O_4/PSS/G5.NHAc-FI-FA with KB-LFAR. The unstained cells showed almost no magnetic signal and the small

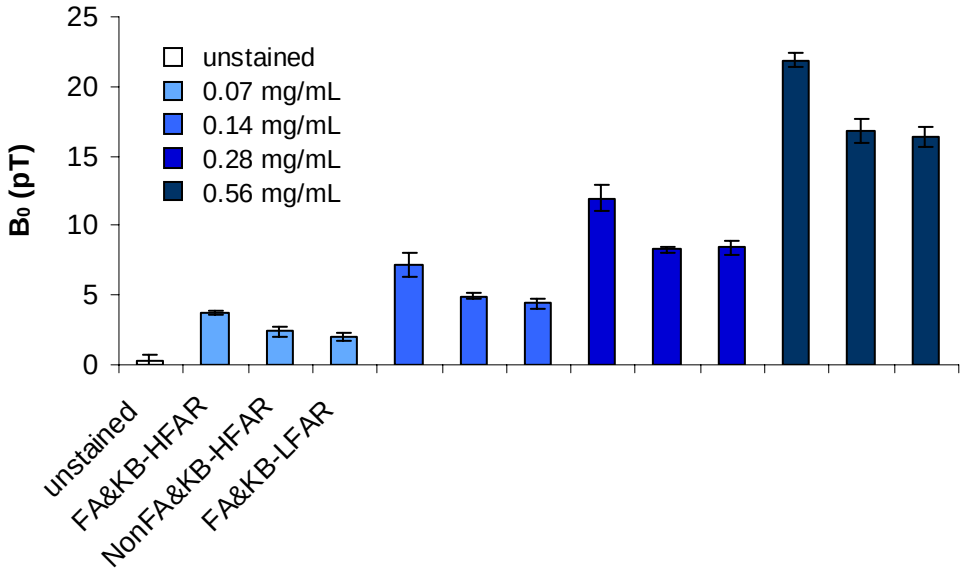

Figure 4.11 The SQUID-MRX data on the FA-modified NP targeted KB-HFAR cells compared with the two control groups.

nonzero value is within the uncertainty of the measurement. For the two control groups, the SQUID detected some signal, which is caused by unspecific NP uptake of cells. But the graph clearly shows the FA-modified NP enhanced the intracellular uptake by the FA-FAR interactions at all measured iron concentrations. This agrees well with the flow cytometry data. The two control groups showed similar signal strength, indicating similar NP uptake level. In each subgroup, the absolute intensity increment of the targeted group from the two control groups becomes larger as the concentration increases. However, the relative enhancements are 71%, 55%, 59%, and 32% showing a saturation behavior of the FA-FAR targeting mechanism, which qualitatively agrees with previous observations.[2] In this calculation, the signals of the control groups were averaged due to their similar levels.

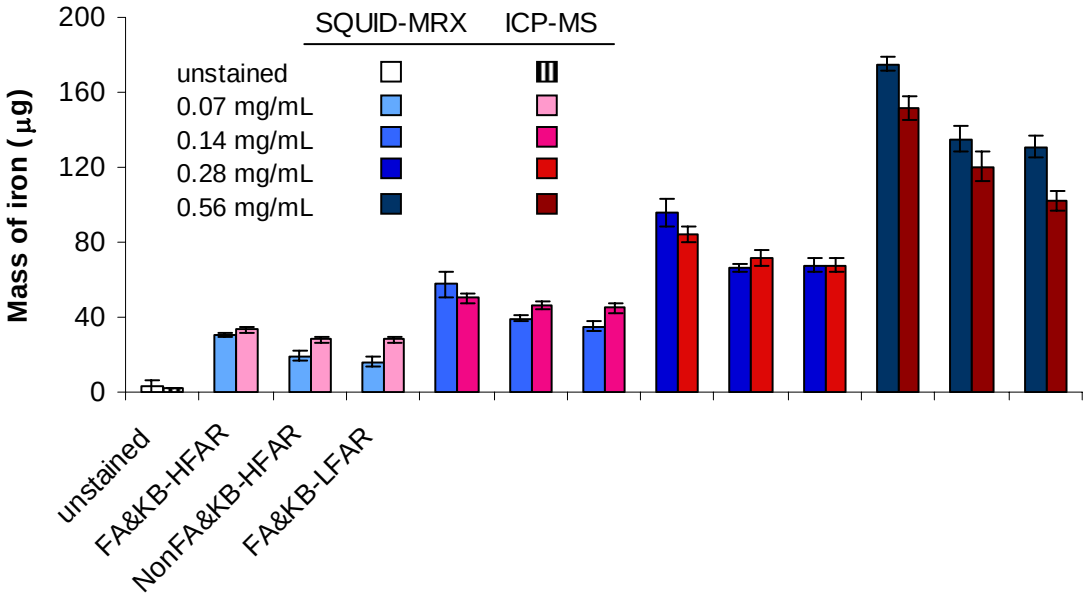

Figure 4.12 The comparison between the iron contents of the NPs up-taken by KB cells expressing HFAR and LFAR levels determined by the SQUID-MRX and ICP-MS.

To confirm the data acquired from SQUID-MRX, ICP-MS was conducted to investigate the iron content of each sample using a portion of the cells in the SQUID study. The result of ICP-MS measurement is the iron concentration of the dissolved and diluted Fe_3O_4 NP solution. According to the experimental parameters described in section 4.2.11, the total amount of iron in the SQUID study can be deduced by multiplying the ICP measured iron concentration with the dilution factor and the total volume of the cells 350 μL. Meanwhile, based on the calibration curve (Figure 4.8) of the 15.4 nm NPs, the amount of Fe_3O_4 NPs can also be calculated from the sensitivity of the line, hence the iron's mass. The comparison between the calculated iron mass from both methods are compared in Figure 4.12. The two sets of data match well with the average relative error (averaging the absolute values) with respect to the ICP result of ~17%. From the NPs' concentrations in the incubated cells: 0.07, 0.14, 0.28, and 0.56 mg/mL, we can calculate

the total amount of iron used in each scenario: 25, 50, 100, and 200 μg, respectively. In the figure, the measured iron contents are similar to or smaller than the maximal values in all cases. The SQUID system based on the relaxation measurement is a reliable device and can be applied to quantitatively determining the existence of magnetic NPs.

4.4 Reference

1. Landmark, K.J., et al., *Synthesis, characterization, and in vitro testing of superparamagnetic iron oxide nanoparticles targeted using folic acid-conjugated dendrimers.* Acs Nano, 2008. **2**(4): p. 773-783.

2. Shi, X.Y., et al., *Synthesis, characterization, and intracellular uptake of carboxyl-terminated poly(amidoamine) dendrimer-stabilized iron oxide nanoparticles.* Phys. Chem. Chem. Phys., 2007. **9**(42): p. 5712-5720.

3. Shi, X.Y., et al., *Dendrimer-functionalized shell-crosslinked iron oxide nanoparticles for in vivo magnetic resonance imaging of tumors.* Adv. Mater., 2008. **20**(9): p. 1671-1678.

4. Wang, S.H., et al., *Dendrimer-functionalized iron oxide nanoparticles for specific targeting and imaging of cancer cells.* Adv. Funct. Mater., 2007. **17**(16): p. 3043-3050.

5. Gupta, A.K. and M. Gupta, *Synthesis and surface engineering of iron oxide nanoparticles for biomedical applications.* Biomaterials, 2005. **26**(18): p. 3995-4021.

6. Corot, C., et al., *Recent advances in iron oxide nanocrystal technology for medical imaging.* Adv Drug Deliv Rev, 2006. **58**(14): p. 1471-504.

7. Renshaw, P.F., et al., *Ferromagnetic contrast agents: a new approach.* Magn Reson Med, 1986. **3**(2): p. 217-25.

8. Anzai, Y., *Superparamagnetic iron oxide nanoparticles: nodal metastases and beyond.* Top Magn Reson Imaging, 2004. **15**(2): p. 103-11.

9. Barrett, T., et al., *Macromolecular MRI contrast agents for imaging tumor angiogenesis.* Eur J Radiol, 2006. **60**(3): p. 353-66.

10. Cushing, B.L., V.L. Kolesnichenko, and C.J. O'Connor, *Recent advances in the liquid-phase syntheses of inorganic nanoparticles.* Chemical Reviews, 2004. **104**(9): p. 3893-3946.

11. LesliePelecky, D.L. and R.D. Rieke, *Magnetic properties of nanostructured materials.* Chemistry of Materials, 1996. **8**(8): p. 1770-1783.

12. Mefford, O.T., et al., *Stability of polydimethylsiloxane-magnetite nanoparticle dispersions against flocculation: interparticle interactions of polydisperse materials.* Langmuir, 2008. **24**(9): p. 5060-9.

13. Vadala, M.L., et al., *Cobalt-silica magnetic nanoparticles with functional surfaces.* Journal of Magnetism and Magnetic Materials, 2005. **293**(1): p. 162-170.

14. Peng, S., et al., *Synthesis and stabilization of monodisperse Fe nanoparticles.* J Am Chem Soc, 2006. **128**(33): p. 10676-7.

15. Hafeli, U.O. and G.J. Pauer, *In vitro and in vivo toxicity of magnetic microspheres.* Journal of Magnetism and Magnetic Materials, 1999. **194**(1-3): p. 76-82.

16. Mornet, S., et al., *Magnetic nanoparticle design for medical applications.* Progress in Solid State Chemistry, 2006. **34**(2-4): p. 237-247.

17. Muller, R., et al., *Magnetic particles for medical applications by glass crystallisation.* Journal of Magnetism and Magnetic Materials, 2004. **272-76**: p. 1539-1541.

18. Fried, T., G. Shemer, and G. Markovich, *Ordered two-dimensional arrays of ferrite nanoparticles.* Adv. Mater., 2001. **13**(15): p. 1158-+.

19. Kang, Y.S., et al., *Synthesis and characterization of nanometer-size Fe3O4 and gamma-Fe2O3 particles.* Chem. Mater., 1996. **8**(9): p. 2209-&.

20. Tang, J., et al., *Magnetite Fe3O4 nanocrystals: Spectroscopic observation of aqueous oxidation kinetics.* J. Phys. Chem. B, 2003. **107**(30): p. 7501-7506.

21. Hyeon, T., et al., *Synthesis of highly crystalline and monodisperse maghemite nanocrystallites without a size-selection process.* J. Am. Chem. Soc., 2001. **123**(51): p. 12798-12801.

22. Sun, S.H. and H. Zeng, *Size-controlled synthesis of magnetite nanoparticies.* J. Am. Chem. Soc., 2002. **124**(28): p. 8204-8205.

23. Lu, A.H., E.L. Salabas, and F. Schuth, *Magnetic nanoparticles: Synthesis, protection, functionalization, and application.* Angewandte Chemie-International Edition, 2007. **46**(8): p. 1222-1244.

24. Willard, M.A., et al., *Chemically prepared magnetic nanoparticles.* International Materials Reviews, 2004. **49**(3-4): p. 125-170.

25. Cornell, R.M. and U. Schwertmann, *The Iron Oxides*. 2nd ed. 2003, Weinheim: VCH.

26. Ziolo, R.F., et al., *Matrix-Mediated Synthesis of Nanocrystalline Gamma-Fe2o3 - a New Optically Transparent Magnetic Material.* Science, 1992. **257**(5067): p. 219-223.

27. Jana, N.R., Y.F. Chen, and X.G. Peng, *Size- and shape-controlled magnetic (Cr, Mn, Fe, Co, Ni) oxide nanocrystals via a simple and general approach.* Chemistry of Materials, 2004. **16**(20): p. 3931-3935.

28. Monge, M., et al., *Room-temperature organometallic synthesis of soluble and crystalline ZnO nanoparticles of controlled size and shape.* Angewandte Chemie-International Edition, 2003. **42**(43): p. 5321-5324.

29. Seo, W.S., et al., *Preparation and optical properties of highly crystalline, colloidal, and size-controlled indium oxide nanoparticles.* Advanced Materials, 2003. **15**(10): p. 795-+.

30. Trentler, T.J., et al., *Synthesis of TiO2 nanocrystals by nonhydrolytic solution-based reactions.* Journal of the American Chemical Society, 1999. **121**(7): p. 1613-1614.

31. Murray, C.B., D.J. Norris, and M.G. Bawendi, *Synthesis and Characterization of Nearly Monodisperse Cde (E = S, Se, Te) Semiconductor Nanocrystallites.* Journal of the American Chemical Society, 1993. **115**(19): p. 8706-8715.

32. Peng, X.G., J. Wickham, and A.P. Alivisatos, *Kinetics of II-VI and III-V colloidal semiconductor nanocrystal growth: "Focusing" of size distributions.* Journal of the American Chemical Society, 1998. **120**(21): p. 5343-5344.

33. Xie, J., et al., *One-pot synthesis of monodisperse iron oxide nanoparticles for potential biomedical applications.* Pure and Applied Chemistry, 2006. **78**(5): p. 1003-1014.

34. Sun, S.H., et al., *Monodisperse MFe2O4 (M = Fe, Co, Mn) nanoparticles.* J. Am. Chem. Soc., 2004. **126**(1): p. 273-279.

35. Yu, W.W., et al., *Aqueous dispersion of monodisperse magnetic iron oxide nanocrystals through phase transfer.* Nanotechnology, 2006. **17**(17): p. 4483-4487.

36. Gao, S.Y., et al., *Biopolymer-assisted green synthesis of iron oxide nanoparticles and their magnetic properties.* J. Phys. Chem. C, 2008. **112**(28): p. 10398-10401.

37. Hui, C., et al., *Large-scale Fe3O4 nanoparticles soluble in water synthesized by a facile method.* J. Phys. Chem. C, 2008. **112**(30): p. 11336-11339.

38. Vereda, F., et al., *Synthesis and characterization of single-domain monocrystalline magnetite particles by oxidative aging of Fe(OH)(2).* J. Phys. Chem. C, 2008. **112**(15): p. 5843-5849.

39. McClune, W.F., *Powder diffraction File Alphabetical Index Inorganic Phase*. 1980, Swarthmore: JCPDS.

40. Moudler, J.F., et al., *Handbook of X-ray Photoelectron Spectroscopy*. 1992, Eden Prairie, MN: Perkin-Elmer.

41. Dong, Y.M., et al., *A facile route to controlled synthesis of Co3O4 nanoparticles and their environmental catalytic properties.* Nanotechnology, 2007. **18**(43).

42. Shevchenko, E.V., et al., *Colloidal synthesis and self-assembly of CoPt(3) nanocrystals.* J Am Chem Soc, 2002. **124**(38): p. 11480-5.

43. Liang, X., et al., *Synthesis of nearly monodisperse iron oxide and oxyhydroxide nanocrystals.* Adv. Funct. Mater., 2006. **16**(14): p. 1805-1813.

44. Harris, L.A., et al., *Magnetite nanoparticle dispersions stabilized with triblock copolymers.* Chem. Mater., 2003. **15**(6): p. 1367-1377.

45. Maoz, R., et al., *Constructive nanolithography: Site-defined silver self-assembly on nanoelectrochemically patterned monolayer templates.* Adv. Mater., 2000. **12**(6): p. 424-+.

46. Cullity, B.D. and S.R. Stock, *Elements of X-Ray Diffraction*. 3rd ed. 2001, New Jersey: Prentice-Hall.

47. Chikazumi, S., *Physics of Magnetism*. 1964, New York: Wiley.

48. Yang, H., et al., *Magnetic properties of nanocrystalline Li0.5Fe2Cr0.4O4 ferrite.* Mater. Lett., 2003. **57**(16-17): p. 2455-2459.

CHAPTER 5

Conclusions

SQUID detection systems for magnetic nanoparticles (NPs) based on magnetic remanence measurement and magnetorelaxometry (MRX) were established and presented in this dissertation. Both of the systems were carefully designed and improved to achieve high sensitivity. The remanence system exhibits better detection limits due to its reduced particle size dependence than the MRX methodology. A novel synthetic route for Fe_3O_4 NPs was developed, which allows tunable magnetic properties by controlling the particle's size. *In vitro* experiments were performed with MRX and the difference between the targeted and non-targeted NPs up-take levels was detected.

A 1-D scanning remanence based SQUID imaging system was set up, calibrated and investigated. This measurement achieved good noise reduction ability by using phase lock detection, thus leading to high sensitivity (10 ng of the 25-nm Fe_2O_3 NPs can be detected at a distance of 1.7 cm from the SQUID detector). The spatial resolution of the imaging system is about 1 cm in lateral separation, which is limited by the diameter of the SQUID pick-up coils. Based on the system, a theoretical model was proposed which shows excellent agreement with the experimentally acquired images. The model also suggests a computational way to locate the NPs' position, especially the depth in tissue and determine the mass of the particles as well. Image reconstruction was attempted with the 1-D scanning system and the calculated values are close to the experimental controls.

A SQUID-MRX detection system was also developed and tested. To switch off the magnetic biasing field in a few milliseconds, a special circuit was designed. Noise reduction was achieved by both hardware improvements and software algorithms and the suppression is about two orders of magnitude. The particle size dependence of MRX signal was studied experimentally and a series of Fe_3O_4 NPs were measured to determine the optimal sensitivity. Computer simulations which describe the MRX measurement process were used to analyze how the sensitivity is affected by the particles' property. The studies show 1) the currently achieved MRX sensitivity is close to the optimal value and the small offset is possibly caused by the measurement temperature; 2) to significantly enhance the sensitivity, multiple factors have to be changed at the same time, including the mean and distribution of NPs' size, the strength of the biasing field and further techniques reducing the environmental noise.

In order to obtain magnetic NPs with controllable size and a modifiable surface for *in vitro* application of the SQUID-MRX detection, Fe_3O_4 NPs were synthesized. The particles' mean diameter ranged from 15 to 30 nm by changing the concentration of the reactants or the reaction solvent composition. The resultant Fe_3O_4 NPs are single crystals and have high purity. Their magnetic property exhibits a transition from ferromagnetic to superparamagnetic behavior as the particle's diameter decreases. Within the diameter range of the synthesized NPs, it was shown that the NPs with smaller mean size have higher signal in SQUID-MRX measurement. The NPs were further functionalized for cancer cell targeting and the MRX data showed detectable difference between the uptake levels by cell of the targeted and non-targeted NPs. This result agrees with the flow cytometry and ICP-MS studies.